6. AUTOMOTIVE METALS – CROSS-CUTTING

A. Magnesium Research and Technology Development

Principal Investigator: Eric A. Nyberg
Pacific Northwest National Laboratory (PNNL)
P.O. Box 999, Richland, WA 99352
(509) 372-2510; fax (509) 376-1093; e-mail: Eric.Nyberg@pnl.gov

Technology Area Development Manager: Joseph A. Carpenter
(202) 586-1022; fax (202) 586-1600; e-mail; joseph.carpenter@ee.doe.gov

Expert Technical Monitor: Philip S. Sklad
(865) 574-5069: fax: (865) 576-4963; e-mail: skladps@ornl.gov

---

Contractor: PNNL
Contract No.: DE-AC06-76RL01830

Objective

- The Mg Research and Technology Development (MR&TD) project is aimed at increasing the use of the lightest structural metal, magnesium (Mg), in automotive applications.
- Increase awareness and familiarity of Mg as a viable option for automotive applications.
- Support the United States Automotive Materials Partnership's (USAMP) Mg Front End Research and Development (MFERD) project (see 6.C) in collaboration with China and Canada.
- Compile, document and evaluate state-of-the-art R&D in Mg research around the world as a resource to determine where U.S. government resources should be directed.

Approach

- Serve as the MFERD U.S. Project Technical Committee (PTC) Chairman, advising the U.S. Project Steering Committee (PSC) member of on-going activities by the PTC and project tasks.
- Assist in the coordination of U.S. MFERD project meetings and the international three-country meetings.
- Evaluate proposals and oversee the effectiveness of the nine tasks of the MFERD project.
- Conduct and report on the gaps in international research related to Mg R&D.
- Develop and maintain the Mg R&D Bibliographic Database located at Mg.pnl.gov.

Accomplishments

As the U.S. Project Technical Committee (PTC) chairperson, I assumed responsibility to serve as liaison between the project Task Leaders and the U.S. Project Steering Committee (PSC) representative, Dr. Joseph Carpenter, from the DOE Office of Vehicle Technologies (DOE-OVT). In this role, I performed the following activities:

- Coordinated and reviewed progress by the nine U.S. Task Leaders.
- Participated in quarterly international conference calls with other PTC members from China and Canada.
- Co-wrote the U.S. and International Semi-Annual and Annual MFERD Project Reports to DOE.
- Reviewed the U.S. Task Leaders' annual presentations held at United States Council for Automotive Research (USCAR) headquarters on 10/30/07.
- Organized the first annual Task Leaders' meeting which received favorable reviews by the participants and DOE.

- Co-authored a paper with other MFERD PTC members that will be presented at the TMS annual meeting in 2008.
- Developed and maintained a publicly-available database/bibliography on Mg R&D.
- Presented the opening plenary talk on Mg research in North America at the 2006 International Conference on *Mg and Its Alloys* in Dresden, Germany (November 2006).
- Co-authored a proposal for a North American Mg Network of Excellence with colleagues from Oak Ridge National Laboratory (ORNL, P. Sklad) and CANMET (J. Jackman).

Future Direction

- Primary future work on the MFERD project will be to evaluate progress of the MFERD tasks, participate in committee meetings, report results and make recommendations to the PSC.
- Develop resources that can be used at PNNL and ORNL in support of the MFERD project.
- Evaluate and propose Mg R&D activities that are unique and necessary.
- Serve as the TMS Mg Light Metals Committee Vice-Chairman and Symposium co-organizer.

Introduction

The primary purpose of this project is to support the Canada-China-U.S. collaborative project entitled "Mg Front End Research and Development" (MFERD; see 6.C). The goal of the MFERD project is to develop key enabling technologies for a lightweight, Mg, front-end body structure and other body applications. The MFERD project will develop enabling technologies in high-integrity casting, wrought-Mg processing, Mg and dissimilar-metal joining and corrosion, and generate scientific understanding in corrosion science, crash-energy management, fatigue, and noise, vibration and harshness (NVH) performance. The project will also provide a platform for Mg research collaboration in Canada, China, and the United States.

Background

The primary goal of the MFERD project is to develop key enabling technologies (body casting, extrusion, sheet & joining) and knowledge base (crashworthiness, NVH, durability, and corrosion) for primary (load-path) body applications of Mg alloys. The following are some specific objectives:

- Define materials and develop manufacturing processes for Mg body castings, extrusions, sheet, and joining technologies.
- Develop knowledge base and define Mg-body technical requirements in crashworthiness, NVH, durability, corrosion, and surface finishing.
- Enhance the infrastructure for integrated computational materials engineering for Mg applications, including alloy design/ development, process optimization, and component manufacturing (see 6.F to 6.G).
- A total life-cycle analysis showing the net benefit of vehicle lightweighting, using Mg vs. energy consumption, emission, and pollution in Mg production.
- High-quality professionals and students educated in materials science, engineering, and Mg research and development (R&D) infrastructure in Canada, China, and the United States.
- Establish automotive OEM / supplier / academia collaboration in Mg-body applications.

PNNL Approach to Supporting MFERD Project and Database Development

As the U.S. Project Technical Committee Chairman, I have participated in all project-related meetings since the initial three-country meeting held in Dearborn, MI in October 2005. The continuity and background developed because of this participation has made me uniquely qualified to advise the U.S. Project Steering Committee representative (Dr. Joseph A. Carpenter, Jr.) on the technical issues, task status, and cultural complexities that can and will develop as the project matures.

Other related activities include:

- Attended International Mg Workshop at Johns Hopkins University's *Center for Advanced Metallic and Ceramic Systems*, sponsored by the Army Research Laboratory (Baltimore, MD).
- Reviewed two international proposals: a Canadian proposal to develop a "*Center of Excellence*" on Mg research at the University of British Columbia and another for the Department of Manufacturing Engineering and Engineering Management at the City University in Hong Kong.

Conclusions

This technical-support project is aimed at effectively assisting in the management of the U.S. portion of the three-country MFERD project. To date, we have completed the first full year of the MFERD project and the annual report will be submitted by the end of the calendar year. Additionally, this project will serve as a resource for future funding decisions related to DOE-funded Mg projects.

Current and Future Work

Future work will be to evaluate progress of the tasks, participate in committee meetings, report results and make recommendations to the U.S. PSC Chairman.

Currently, we are in the midst of organizing plans for the 2nd Annual Task Leaders' meeting that will be held in China on April 2 and 3, 2008. This meeting will follow the joint PSC/PTC meeting. The U.S. and Canadian Task Leaders and PTC Chairmen plan to visit several facilities and organizations in China that are involved in the MFERD project.

Research opportunities inside and out of PNNL will be reviewed and proposed to DOE in consideration for future funding opportunities. Continue to manage the publicly-available Mg R&D Database.

Issue final version of the Mg Gap Analysis Report to the DOE Technology Area Development Manager, providing recommendations on critical areas of R&D funding that are not being adequately addressed.

Presentations

"*Mg Automotive R&D in North America*", J. Jackman, J. Carpenter, E. Nyberg, at the Intl. Conference on Mg Alloys and their Applications, Dresden, Germany, November 6, 2006.

B. Magnesium Front-End Design and Development (AMD 603[i])

Principal Investigator: Alan A. Luo
General Motors (GM) Research & Development Center
MC 480-106-212
30500 Mound Road
Warren, MI 48090-9055
(586) 986-8303; fax: (586) 986-9204, e-mail: alan.luo@gm.com

Program Technical Administrator: Robert C. McCune
Robert C. McCune and Associates, LLC
5451 S. Piccadilly Circle
West Bloomfield, MI, 48322-1446
(248) 661-0085; fax: (248) 661-8718; e-mail: robert.mccune@sbcglobal.net

Technology Area Development Manager: Joseph A. Carpenter
(202) 586-1022; fax: (202) 586-1600; e-mail: joseph.carpenter@ee.doe.gov

Field Project Officer: Aaron D. Yocum
(304) 285-4852; fax (304) 285-4403; email: aaron.yocum@netl.doe.gov

Expert Technical Monitor: Philip S. Sklad
(865) 574-5069; fax: (865) 576-4963; e-mail: skladps@ornl.gov

---

Contractor: United States Automotive Materials Partnership (USAMP)[i]
Contract No.: DE-FC05-02OR22910 through the National Energy Technology Laboratory

---

Objectives

The goal of the project is the engineering design/analysis and technical cost modeling for magnesium (Mg)-intensive, front-end structures for selected unibody and body-on-frame (BOF) vehicle architectures with the following design targets:

- Mass reduction: 60% (approx. 40 kg) lighter than comparator steel baseline structures and 35% (approx. 16 kg) lighter than aluminum (Al) structures for mid-size passenger cars at comparable strength and crashworthiness.
- Vehicle mass distribution: Shift the front-to-rear mass ratio by -1/+1 toward 50/50 for the rear-wheel drive, unibody donor architecture.
- Demonstration via technical cost modeling of a maximum of $8/kg (of mass saved) cost penalty (100,000 vehicles/year production volumes), via part consolidation using large Mg castings (e.g., dash panel, shotguns) and attractive pricing of Mg in world markets.
- Matched or improved key performance characteristics such as stiffness, durability and noise, vibration and harshness (NVH) of the Multi-Materials Vehicle (MMV, see 12.D) 'donor' vehicle as determined via simulation.

Approach

Task 1. Mg Front-End Design Deliverables: The Mg front-end design and analysis for the two selected vehicle architectures will consist of the following deliverables expected from the supplier with appropriate industry inputs:

- All computer-assisted design (CAD) and computer-assisted engineering (CAE) data.
- Bill-of-materials (materials properties and standards).

- Definition of interfaces to steel structure.
- Typical sections.
- Corrosion-prevention strategies and designs.
- Typical sections.
- Performance assessments:

  -- Frontal Crash: 35-miles-per-hour (mph), flat, frontal New Car Assessment Program (NCAP) and 40-mph Insurance Institute for Highway Safety (IIHS) Front Offset Deformable barrier (FODB).

  -- Stiffness (dynamic and static).

  -- Durability.
- Mass.
- Assembly.
- Impact on body-shop assembly.
- Assembly sequence.
- Paint-shop impact.
- Recycling strategies with attention to disassembly.
- Repair procedures, both in-plant and during use.

The design exercise will be staged to coincide with data being developed with regard to materials and processes as part of Mg Front-End Research and Development (AMD 604, see 6.C). The staging of the design project is summarized below:

A. Unibody Front-End Design Staging – Three Design Iterations

(1) First Design Iteration (6 months) based upon:

- Existing literature and USAMP material-property and performance data.
- Property data of experimental alloys provided by the USAMP team.
- Commercially-available manufacturing technologies, and
- Promising, non-commercial-scale, manufacturing processes selected by the USAMP team.

(2) Second Design Iteration (one year after the first iteration milestone) based upon:

- Materials-property data generated and/or validated in the AMD 604 project.
- Manufacturing processes developed and/or validated in the AMD 604 project, and
- Performance knowledge base (corrosion, crashworthiness, NVH, etc.) developed in the AMD 604 project.

(3) Third Design Iteration (one year after the second iteration milestone) based upon:

- Design optimization including part and function integration using all materials and manufacturing enabling technologies and performance knowledge base (corrosion, crashworthiness, NVH, etc.) developed in the AMD 604 project; and
- The manufacturing processes developed and/or validated in the AMD 604 project and the best practices and Mg technologies developed in the world-wide market.

B. Body-on-Frame Front-End Design Approach

- Utilize well-developed, Ford/USAMP designs for the Mg, upper-radiator support and Mg “shotgun” structure developed in collaboration with the Ultra Large Casting Project (see 3.C).
- The design effort in this project is focused on the attachment schemes at the A-pillar/shotgun interface and, additionally, the exploration of more part integration with the rest of the body structure.

- The BOF design is being carried out in parallel to the unibody design and is progressive in nature, incorporating the learning from the AMD 604 project and the new technologies developed in the industry during the project design phase (2.5 years).

Task 2. Technical Cost Modeling

The approach uses process-based, technical cost modeling [1] to provide the following deliverables for the two front-end designs (unibody and BOF):

- Determine primary Mg production costs, sustainability and market impact of the electrolytic vs. direct thermal-reduction (Pidgeon) processes.
- Provide a detailed cost analysis and report for all the components and assembly identified by Task 1 for both the unibody and BOF designs.
- Current steel designs for both the unibody and BOF are the comparators for weight and cost.
- The work is divided into two phases. Phase I includes a primary Mg production analysis and the component cost of individual parts for each design. Phase II includes the assembly of the components to each other and to the main body structure. Phase II will also incorporate any updates to Phase I determined by design changes or information gathered by AMD 604.
- This cost analysis includes surface finishing, machining or any other process each component requires to allow it to be attached or integrated with the rest of the front-end assembly. The overall cost of the assembly including components is provided for each design as compared to the steel baseline.

Accomplishments

- OEM project kickoff: November 1, 2006.
- Supplier kick-off and request for proposals: November 28, 2006.
- Selection of Cosma Engineering of Troy, MI, Task 1 (Design).
- Selection of Camanoe Associates of Cambridge, MA, Task 2 (Technical Cost Modeling).
- "Donor" vehicle baseline math data and vehicle design/performance targets provided to suppliers for design and cost modeling: GM, rear-wheel drive (RWD), unibody construction and Ford, BOF, pickup truck.
- Initial design for the unibody Mg front end was completed with stiffness and concept level crash assessments, as well as bill-of-materials.
- Specific progress against design and performance targets:

  -- (Unibody) part-count reduction: 50 pieces (29 Mg Front End vs. 79 steel baseline).

  -- Mass reduction: 37 kg (45%).

  -- Materials technologies: 15 castings, 3 extrusions, 9 formed sheets.

  -- Initial joining strategies developed.

  -- Crashworthiness (unibody): IIHS Deformable Barrier – maximum structural intrusions "acceptable" or "good" rating via simulation. NCAP, 35-mph, full frontal – deceleration pulse comparable to steel baseline.

  -- Modal analysis – full body-structure-only modes occur at higher frequencies than baseline.

  -- (BOF) – part count reduction: 7.

  -- Mass reduction (45%).
- Technical Cost Modeling: Detailed statement of work concluded; team kickoff; developed modeling framework and identified key variables.

Future Direction

- The design supplier (Cosma Engineering) will present its 1st total design iteration for review on December 10, 2007.

- The interim design reviews (four to date) have been used to track design progress and also to provide feedback to the designer with regard to materials and process feasibility or criticisms of the design itself. These design reviews are expected to continue as the next design iteration proceeds.
- The second design iteration calls for more incorporation of emerging Mg property data generated by the companion AMD 604.
- Materials performance, particularly the ductility and failure of cast metals, is expected to take on more significance due to the relatively large reliance on large castings for the initial design.
- Technical cost modeling will provide insight into the viability of the reliance on large castings.
- The anticipated manufacturing paradigm is also expected to have impacts on such areas as surface pretreatment and finishing, joining and corrosion protection.

Introduction

AMD 603, Mg Front-End Design and Development, is a complementary project to both the AMD 604 (Mg Front-End Research and Development) and the USAMP Multi-Materials Vehicle (MMV) projects. Whereas AMD 604 is predicated on development of enabling Mg technologies on an international scale, involving a wide range of suppliers and organizations, AMD 603 is confined to the OEM participants of USAMP (i.e., Chrysler, Ford and GM) and selected suppliers focused on design specifics and technical cost modeling.

The goal of AMD 603 is the engineering design and computer-aided analysis of Mg-intensive, front-end structures for both a RWD unibody and BOF vehicle architectures that are aimed at meeting defined targets for weight reduction, performance (including vehicle weight redistribution for the unibody design, durability, corrosion resistance, crashworthiness, NVH targets) and subassembly cost within defined parameters (i.e., a maximum cost penalty of $8 per kg of weight saved).

The OEM steering committee for the project determined that there would be two principal tasks: 1.) the actual physical design of the Mg-intensive structures envisioned, taking into account materials and their properties, assumptions regarding manufacturing and a virtual design permitting use of advanced CAE tools aimed at such requirements as crashworthiness, stiffness and NVH (noise, vibration and harshness), and 2.) Technical cost modeling to permit a better assessment of the costs of materials and mass production of the assemblies as designed. Definition of work statements and selection of suppliers for these tasks were the first items to be accomplished in the program.

The Statement of Work for Task 1 (Design) included assumptions declaring those elements of the design envelope and performance expectations provided by the OEM participants (e.g., GM and Ford designs for the candidate structures, based on present materials of use and manufacturing methods) and specific requirements as intended deliverables for the contract, summarized in the Approach section above.

The following sections describe, in greater detail, key technical accomplishments of the project occurring during fiscal year (FY) 2007.

Project Technical Structure, Launch and First-Year Achievements

The development of precise work statements for design and technical cost modeling were critical to the execution of the project, and were largely compiled before the project was unveiled to the supplier community in November, 2006. Four design and three cost-modeling proposals were received in response to the public announcement of the project and request for proposals. In early 2007, potential suppliers were interviewed. Cosma Engineering of Troy, MI was selected to conduct the design portion and Camanoe Associates of Cambridge, MA was selected to conduct the technical cost modeling. The donor vehicles, previously selected by the OEM team based on availability of design data and willingness of the respective OEMs to release such data for purposes of the project, are a GM RWD sedan for the unibody architecture and a full-size, Ford, pick-up truck for the BOF architecture. Relevant baseline CAD data and performance expectations were provided by the OEMs to Cosma at the outset. The

current Ford design utilizes a Mg radiator-support structure which has been described elsewhere [2]. Ultra-large Mg castings are also being evaluated for this vehicle structure as the subject of the USAMP AMD 406 project (Ultra-Large Castings, see 3.C).

The steel-baseline, unibody structure for the donor vehicle front end is illustrated in Figure 1 for purposes of showing the design envelope under consideration.

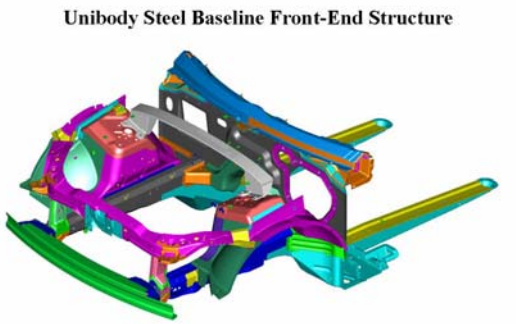

Figure 1. Unibody steel front-end baseline structure for GM donor vehicle.

Similarly, the baseline steel structure for the Ford donor vehicle is illustrated in Figure 2.

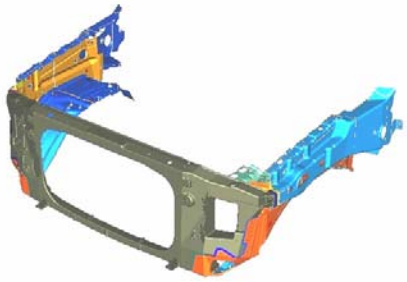

Figure 2. Baseline Ford BOF donor-vehicle steel structure with Mg radiator support.

The initial focus for the designers was the unibody structure, given that the BOF structure was more incremental in its development. The phasing of the design project called for an initial design to be completed six months after receipt of order. This design was to be predicated on "best available" materials properties and manufacturing methods as recommended by the project team. Ultimately, refinements and improvements in the design will occur as knowledge of material properties and manufacturing matures.

Nevertheless, the first unibody design iteration has yielded encouraging projections on most issues. The details are shown in the Accomplishments section above; however, in summary, the design yielded a reduction in part count from 79 to 29, with a weight reduction of 37 kg (45%). The Mg materials technologies utilized were: castings, 15; extrusions, 3; and formed sheet, 9. Other parts included isolators that were not Mg alloys.
Initial concept predictions came in the area of crashworthiness, where, after several iterations of design chiefly through alteration of cross-sectional thicknesses and shapes, it was found that if Mg of sufficient ductility and strength can be developed, then Mg unibody structures could be designed that meet acceptable structural performance for intrusion in IIHS, 40-mph, offset barrier and full-frontal impact at 35 mph. However, these initial results were based on Mg material performance of infinite ductility and no fracture in high-rate deformation (typically Mg does not behave with high ductility). Hence, the results are encouraging but not verified, and must be revisited as materials-property information is improved through the companion AMD 604 and AMD 702/703 projects (see 6.F). Further improvements are also expected as knowledge regarding joining, particularly employing structural adhesive bonding as a supplement to fasteners (e.g., self-piercing rivets), is developed.

The BOF structure has received considerable attention within USAMP as a candidate for a Mg-intensive front end, taking advantage of the large Mg radiator-support assembly already designed and in use by Ford. Attention has focused on integrating the inner fender or "shotgun" structures developed in USAMP AMD 406 (Ultra-Large Castings Project) [3], with attention given to assessing the capabilities of a number of advanced, high-integrity casting processes. Novel corrosion-protection schemes and parts-consolidation strategies are also under investigation. An example of a singe-piece, Mg alloy "shotgun" structure is shown in Figure 3.

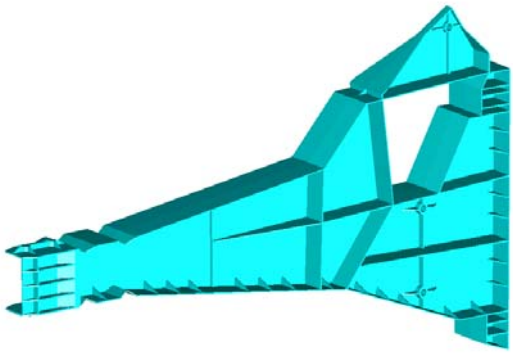

Figure 3. Structural Mg alloy "shotgun" structure designed for the Ford donor vehicle.

Support of the ongoing design activity on this type of structure by Cosma Engineering has, therefore, focused on methods of joining and structural adaptations to accommodate the types of mechanical fasteners envisioned. Successful implementation of the large castings and existing radiator support would effectively reduce the major portion of the front-end structure to three large Mg castings with associated joining hardware.

Conclusions

AMD 603 (Mg Front End Design and Development) was launched in late 2006, and in early 2007 enrolled suppliers for design/engineering and technical cost modeling. Results of the first design iteration, while encouraging, are constrained by limited understanding of the mechanical performance of candidate materials (chiefly Mg-alloy castings) under crash conditions, which are paramount in such a design exercise. Design targets for part-count reduction are similarly encouraging, and weight reduction, while appreciable (e.g., 45% relative to baseline steel), is expected to improve further as material properties are improved and physical designs are optimized.

Presentations/Publications

Mention of the AMD 603 Project has been included in the following reviews of the larger AMD 604 project:

1. A. Luo, E. Nyberg, K. Sadayappan and W. Shi, "Mg Front End Research & Development - A Canada-China-USA Collaborative Project", TMS Annual Meeting, Orlando, FL, USA, February 25 – March 1, 2007.
2. A. Luo, R. McCune, R. Beals, S. Logan, E, McCarty, J. Allison, M. Maj, D. Wagner, T. Lee, R. Osborne, L. Ouimet, J. Quinn and R. Verma, "The USAMP Mg Front End Program - Design and Enabling Technology Development", International Mg Association Mg in Automotive Seminar, Livonia, MI, USA, March 28, 2007.
3. A. Luo, R. McCune, R. Beals, S. Logan, E. McCarty, J. Allison, M. Maj, D. Wagner, T. Lee, R. Osborne, L. Ouimet, J. Quinn and R. Verma, "Mg Front End Development - USAMP Activities", Society of Automotive Engineers (SAE) 2007 Congress, Detroit, Michigan, USA, April 16-19, 2007.

References

1. R. Kirchain and F.R. Field III, "Process-Based Cost Modeling: Understanding the Economics of Technical Decisions," Encyclopedia of Materials Science and Engineering, 2001.
2. J. S. Balzer, P. K. Dellock, M. H. Maj, G. S. Cole, D. Reed, T. Davis, T. Lawson and G. Simonds, "Structural Mg Front End Support Assembly," SAE Paper No. 2003-01-0186 (2003).
3. U.S. Department of Energy, USAMP AMD 406 Annual Report (2007).

Acknowledgements

The success of this project is due to the dedicated efforts of team members at Ford, Chrysler, and General Motors, as well as the suppliers Cosma Engineering and Camanoe Associates. The continuing support of our respective organizations and the US Department of Energy is gratefully acknowledged.

[i] Denotes project 603 of the Automotive Materials Division (AMD) of the United States Automotive Materials Partnership (USAMP), one of the formal consortia of the United States Council for Automotive Research (USCAR) set up by Chrysler, Ford and General Motors (GM) to conduct joint, pre-competitive research and development. See www.uscar.org.

C. Magnesium Front-End Research and Development (AMD 604[i])

Principal Investigator: Alan A. Luo
General Motors (GM) Research & Development Center
MC 480-106-212
30500 Mound Road
Warren, MI 48090-9055
(586) 986-8303; fax: (586) 986-9204; e-mail: alan.luo@gm.com

Program Technical Administrator: Robert C. McCune
Robert C. McCune and Associates, LLC
5451 S. Piccadilly Circle
West Bloomfield, MI, 48322-1446
(248) 661-0085; fax: (248) 661-8718; e-mail: robert.mccune@sbcglobal.net

Technology Area Development Manager: Joseph A. Carpenter
(202) 586-1022; fax: (202) 586-1600; e-mail: joseph.carpenter@ee.doe.gov

Field Project Officer: Aaron D. Yocum
(304) 285-4852; fax (304) 285-4403; email: aaron.yocum@netl.doe.gov

Expert Technical Monitor: Philip S. Sklad
(865) 574-5069; fax: (865) 576-4963; e-mail: skladps@ornl.gov

---

Contractor: United States Automotive Materials Partnership (USAMP)[i]
Contract No.: DE-FC05-02OR22910 through the National Energy Technology Laboratory

---

Objective

The goal of this US-Canada-China collaborative project is the concurrent development of key enabling materials and manufacturing technologies and the accompanying performance knowledge base to permit design and implementation of magnesium (Mg)-intensive, automotive-body, front-end structures having greatly reduced mass, but with performance and cost comparable to sheet-steel baseline structures.

Two aspects of this project are unique within the USAMP:

- The focus is on entire "front-end" structures as the developmental object, in contrast to individual components, thereby offering critical, vehicle-level benefits in terms of mass distribution and performance while challenging the technical community to devise materials and manufacturing approaches to permit mass production of such structures at reasonable cost.

- Establishment of an international effort enlisting the best scientific and engineering expertise in Mg technology from the United States, Canada and China in a first-of-its-kind, global collaboration.

Approach

- Organization and Administration: Establishment of organizational and technical steering committees and systematic management of information and activities in a global environment.

- Partitioning of Projects: Separation of the design function into a separate USAMP project (AMD 603, see 6.B) as well as Integrated Computational Materials Engineering - ICME (AMD 702 and 703, see 6.F), to facilitate handling of original equipment manufacturer (OEM)-sensitive design data and to permit a broader, more uni-

versal approach to ICME. Further partitioning by subject-matter expertise and capabilities. The international project, additionally, has a task for life-cycle analysis, in which USAMP is not participating (see 12.A).

- Enabling Technologies: Assessment of the state-of-the-art and development of emerging technologies in primary forming, joining and finishing that would permit manufacture of the envisioned structures.

- Knowledge Base: Understand the current awareness and knowledge gaps with regard to materials and structural performance in the intended application, particularly with regard to crashworthiness, noise-vibration harshness (NVH), fatigue and durability, including corrosion.

- Technical Gateways: Provide for rigorous assessment of progress against pre-determined metrics at sub-levels of the project, assuring that functional targets are achieved or, alternatively, that further efforts are discontinued if required metrics cannot be achieved. Gateways exist for both the design stage and also for the enabling technologies, such that efforts for actual prototype build (Phase 2) only occur at successful accomplishment of Phase 1. Overall timing and conceptual flow for projects AMD 603 and AMD 604 are illustrated in Figure 1.

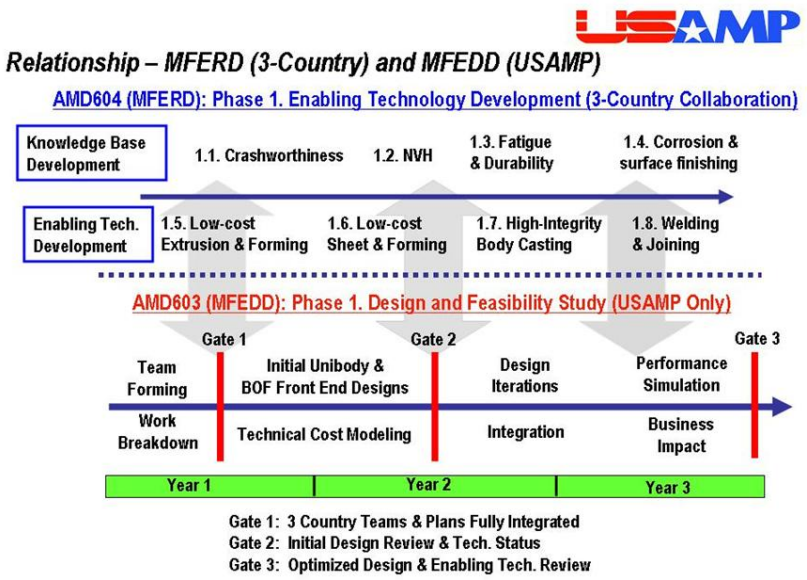

Figure 1. Schematization of AMD 603 and AMD 604 partitioning and technical gateways.

Accomplishments

The relationship between activities of the individual task areas and overall project objectives is summarized by the "fishbone" diagram shown in Figure 2. Targets for knowledge-based and enabling technologies are illustrated therein.

- OEM launch of AMD 604 by USAMP on November 1, 2006, followed by an OEM-supplier kickoff on November 28, 2006.
- Canadian program kickoff August 2006; China program kickoff December 2006.
- In calendar year (CY) 2007, the U.S. and International Task Teams conducted various organizational meetings and enlisted key supplier and funding organizations in their respective countries.
- Meetings of the Project Steering Committee (PSC), Project Technical Committee (PTC) and individual task representatives of the three countries were held on March 1 and 2, 2007 following the TMS Annual Meeting in Orlando, Florida. Follow-up sessions were also conducted in the Detroit area after this meeting.

- All international task teams have agreed on the technical agenda for the overall project and individual task areas including partitioning of the efforts, deliverables and timing.
- The PTC conducted meetings via teleconference on June 6, September 5 and December 18, 2007.
- The PTC and PSC have agreed upon April 2-4, 2008 as the time for the next three-country progress meeting to be held in Hangzhou, Peoples Republic of China (PRC).
- Project leadership received the AMD board of directors concurrence for meeting the goals of Gate 1 (project organization and setting of program metrics and timing).
- The first annual U.S. Project Review was held on October 30, 2007, for OEM and supplier participants.
- 31 Supplier companies have provided work plans and 19 purchase orders have been released.
- USAMP AMD 604 Task Area Highlights:
    - Task 1.1 Crashworthiness – Determination by partners of strain-rate regimes to be studied by each country and initial materials. LS-DYNA models are being fit to properties measured for AZ31 and AM30.
    - Task 1.2 Noise, Vibration and Harshness (NVH) – Delivery of flat Mg panels, actual-shape production parts, and base-line donor vehicle computer-aided design (CAD) data and NVH design and performance data from U.S. OEMs to Canadian and Chinese researchers to verify correlation of numerical simulation tools being developed.
    - Task 1.3 Fatigue and Durability – Fatigue efforts partitioned between three-country participants and also ICME (Mississippi State) contributors. AM30 extrusion material being prepared for round-robin testing.
    - Task 1.4 Corrosion and Surface Treatment – International work plan developed. U.S. team has enlisted suppliers for metal pre-treatment, anodizing, polymeric topcoat and analysis methods. Separate subteams were formed for fasteners, pre-treatment and testing.
    - Task 1.5 Extrusion - Extrusion alloys (AM30 and AZ61) selected and the property data provided to AMD 603 design team. Initial evaluation of microstructure, texture and mechanical properties of AM30 and AZ31 extruded sections conducted. Bending and warm-gas forming processes defined for Mg alloy extrusions.
    - Task 1.6 Sheet Forming – Exemplary sheet materials obtained from U.S. supplier (Mg Elektron), and Chinese supplier (Luoyang Copper). AZ31 sheet property data provided to AMD 603 design team. Initial evaluation of sheet microstructure and tensile and biaxial formability completed. The warm forming tools & process development, under the companion USAMP program AMD 602 (see 2.B), is on schedule, with the Deep Pan Die operational and successful demonstration of forming with direct-chill (DC) Mg sheet.
    - Task 1.7 High-Integrity Large Castings – International tasks defined and castings work initiated. For the U.S., a modified existing strut tower tool is being used in to develop the Super Vacuum Die Casting (SVDC) process for Mg. 100 SVDC castings have been produced in AZ91D. Casting-quality confirmation testing is underway. Castings to be free of cracks as determined by dye penetrant; porosity levels to be equal to or better than ASTM E-505 Level 1; and castings are to be heat treatable and weldable.
    - Task 1.8 Joining - Subteams established and suppliers engaged to pursue development of pretreatment, adhesive, self-piercing rivets (SPR), threaded mechanical fasteners and blind rivets. Pretreatment subtask began strength and corrosion assessment of baseline (untreated) and pre-treated substrates using two adhesives and eight pretreatments.

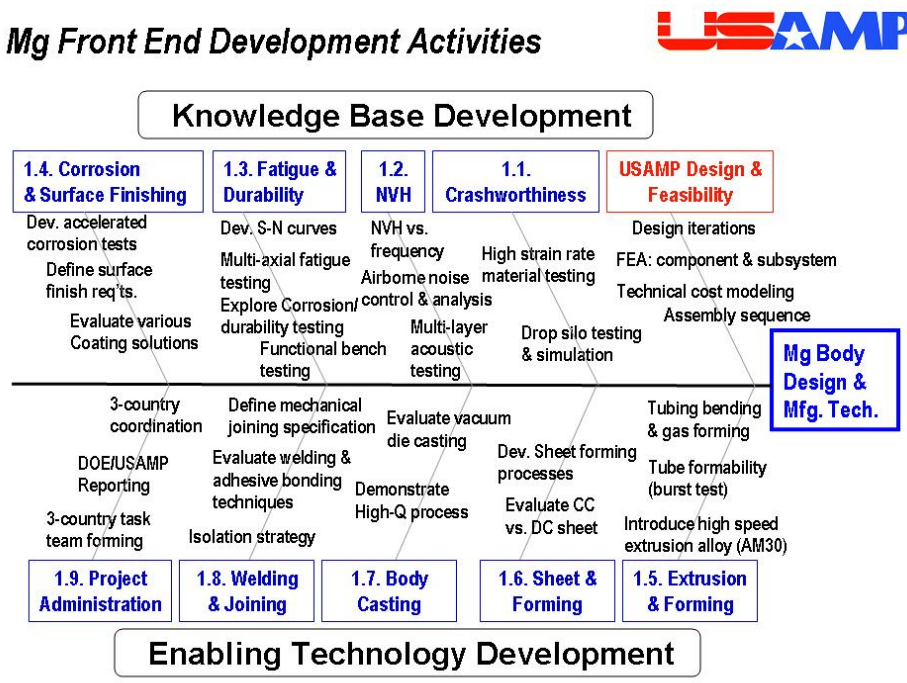

Figure 2. Mg front-end project/task structure fishbone diagram.

Future Direction

- Continuation of international discussions and progress reports via next annual meeting in Hangzhou, China (April 2008).
- Completion of requisite documentation for remainder of suppliers and issuance of USAMP purchase orders. Continue to book in-kind project contributions.
- U.S. Task Teams to provide updated physical property, material performance and manufacturing recommendations to AMD 603 Design Team.
- Information-sharing platform (web site) for international cooperation expected to become operational in calendar year (CY) 2008 upon resolution of all matters related to export-control regulations.
- 2008 Project Review to be held approximately end of October, 2008.

Introduction

Despite numerous advances in Mg manufacturing technologies, widespread and expanded use of Mg as a major automotive structural material has yet to be realized [1]. This is, in part, due to fundamental physical property limitations of Mg castings, which are the predominant form of usage, particularly with regard to deformation and fracture behaviors. Furthermore, technologies which permit the manufacture of extended structures by joining of individually-formed components are not well developed for Mg. Nevertheless, as a structural material, with high strength-to-weight values approaching or exceeding that of Al, Mg offers an attractive approach for achieving the FreedomCAR Materials goals of up to 50% weight reduction in comparison to mild steel baseline, with cost, durability and recyclability attributes that are comparable or better than other structural materials of consideration.

Project AMD 604 (Mg Front-End Research and Development – MFERD) has brought together a talented team of international scope (i.e., United States, China and Canada) to explore and develop certain "enabling" technologies which could, if successful, permit the integration of Mg-based subelements (e.g., castings, extrusions and formed sheet) into optimized assemblies for vehicle body-

structure applications. In this project the vehicle "front-end" structures for unibody and body-on-frame (BOF) architectures, serve as test beds by demonstrating significant levels of subassembly weight reduction and concomitant vehicle handling attributes, thereby, supporting the FreedomCAR goals for lightweighting materials.

The background for establishing this international effort has been previously reported [2,3]. The approach is aimed at bringing together those unique attributes from each nation, e.g., United States – product development, design and manufacturing; Canada – extractive metallurgy and manufacturing; and China – low-cost extraction, forming and component manufacturing processes, into a homologous project with the commonized technical focus of a useful and critical aspect of lightweight vehicle architecture.

The following sections describe key technical attributes of the project and accomplishments occurring during Federal fiscal year (FY) 2007.

2007 Progress and Accomplishments

Project Management and Organization: Although initial efforts began in the participant countries in late 2006, the first collective meeting occurred in March 2007 in Orlando, FL. While a draft work statement had served for organizational purposes, greater details were added at this meeting as well as a focus on the subject tasks as shown in Figure 2. The broader objectives for the project were cascaded into task-level deliverables that were discussed at a technical level among the experts present and formalized into work plans for each contributing country. A follow-up meeting was also held in southeast Michigan for purposes of continued discussions, particularly with the Chinese visitors and conducting tours of industrial and academic facilities.

Task 1.1 - Crashworthiness: Crashworthiness research includes material testing, failure characterization, computer-aided engineering (CAE) analyses and selected testing of a prototype section in crush (low loading rate) and crash (high loading rate) component tests. The strain rates for the material testing range from quasi-static (10^{-3} sec^{-1}), through the mid rates of 10 sec^{-1}, up to 1000 sec^{-1}, which is observed in the high-deformation areas during a high-speed crash. During 2007, initial testing began in the U.S., Canada and China. The LS-DYNA material models are being fit to the strain-rate and failure data for extrusion AM30 and AZ31 materials. A double top-hat section was chosen for future component testing to verify the CAE predictions.

Task 1.2 – NVH: NVH research focuses on sound transmission characteristics of Mg alloys to be used in dash panels. This research includes experimental analysis of Mg panels at 2-mm and 4-mm thickness and development of simulation tools that provide good correlation to the test panels for use in designing quiet Mg dash panels. The major accomplishments of this task for the first year have included: 1.) development of a working agreement between partner countries, 2.) delivery of flat Mg panels, actual-shape production parts, and baseline donor-vehicle CAD data and NVH design and performance data from U.S. OEMs to Canadian and Chinese researchers to verify correlation of numerical simulation tools being developed, and 3.) numerical studies of mid-to-high frequency airborne acoustic performance and modal analysis for flat panels were completed and experimental studies are underway to verify results of the computer simulations. Modifications will be made to the numerical simulation tools if the tested correlation is not good.

Task 1.3 - Fatigue and Durability: This task studies, improves and compares the fatigue-predictive capability for analyzing Mg-component and -subsystem behavior, by understanding the critical interactions of design, material and processing parameters that influence component microstructure and subsequent properties. Casting, extrusion and sheet products will be characterized sufficiently to establish links between microstructural features and fatigue behavior. Required monotonic and cyclic material properties for both multi-scale and traditional fatigue analysis methods were defined. Mississippi State University (MSST) via the AMD 702 (ICME) project and Canada's Ryerson University have completed limited monotonic and cyclic testing of extruded AZ31. The Joining (Task 1.8) Team has provided several joint configurations which will be empirically evaluated and CAE-analysis parameters developed to allow accurate simulations of the fatigue of joints. Both MSST multi-scale and tradi-

tional fatigue analysis methods will be used to analyze component structures when CAD data becomes available.

Task 1.4 - Corrosion and Surface Treatment: The U.S. Team agreed to divide the task into three initial subtasks: metal pre-treatment, fastener-related corrosion and testing methods. Chairpersons were identified and teams formed. Supplier companies have been enlisted to provide prototype pretreatments including conversion coatings, anodizing and various barrier-type layers. Suppliers of fastener coatings were also subscribed to the project and various laboratories have been selected to conduct specific evaluations of the intended sublayers. Since the metal pre-treatment will play a substantial role in the envisioned manufacturing process, it is also critical to understand the performance of the various metal pre-treatments with regard to the joining processes expected, particularly adhesive bonding. The Chinese efforts will incorporate two exemplary pre-treatments presently under development: 1) the micro-arc oxidation process developed at Xi'an University of Technology and 2) a phosphate-based conversion coating developed by the Institute for Metals Research. Canadian efforts will include a study of the cold-spray aluminizing process and also efforts directed to environmentally-assisted fracture (e.g., stress-corrosion cracking). A direct-current (DC) electrochemical technique for comparing the effectiveness of conversion-coating pretreatments is being developed by the Fontana Corrosion center of the Ohio State University.

Task 1.5 - Low-Cost Extrusion: Although initial conceptual designs for the front-end structures suggest a relatively small number of extrusions, these components are crucial insofar as providing among the higher specific strengths observed for structural Mg alloys and expectation of use in critical positions such as bumper beams and crush rails. The traditional limitation to greater use of Mg extrusions is the high cost of manufacturing, dictated in part by the size of the tooling required, and the relatively low rate of production due to the intrinsically poor formability of the material. Efforts underway include expanded use of modeling software such as DEFORM® to predict and optimize extrusion behavior for specific cross-sections. The Institute for Metal Forming of Lehigh University was selected to conduct modeling and microstructural evaluations of the extrusion process. The topic is similarly linked to AMD 702 (ICME) efforts at MSST to understand the influence of microstructure on the extrusion process. First-year results also include initial measurement of crystallographic textures of extruded shapes at key locations. A major U.S. supplier of extrusions, Timminco, has been enlisted to produce experimental shapes for the project.

Task 6 - Low-Cost Sheet and Forming: Mg Elektron of North America (MENA) was engaged as sheet supplier to AMD 604, and has to date provided 300 AZ31 sheet panels (20" x 48") in 2- and 4-mm thickness produced by the conventional DC process. This sheet material has been supplied to various task teams and partners for testing of crashworthiness, NVH, fatigue and joining. Additionally, DC sheet has been provided by the Luoyang Copper Company of China. Experimental low-cost, AZ31 sheet produced by twin-roll, continuous casting (CC) has been received from different suppliers by the companion USAMP program AMD 602 (see 2.B). Initial microstructure characterization of DC and CC sheet materials is completed. Tensile-testing protocol for warm-forming temperature range has been established and implemented at the University of Virginia. Initial tensile testing of two sheet materials is completed. Significant progress was made in establishing the biaxial testing protocol based on Marciniak flat-top punch test to provide intrinsic material formability without frictional effects. CANMET-Materials Technology Laboratory (MTL), Ottawa, has improved the test protocol and is currently evaluating different sheet materials. The initial emergent designs for the unibody front-end structure call for a number of components formed from Mg sheet.

The development of warm-forming tools and processes for making these parts is being carried out under the companion USAMP program AMD 602, and the complete progress is reported under that project. In summary, the tool and process development is proceeding as scheduled. The new Warm Forming Deep Pan Die is fully operational. Thermal modeling was used to optimize die design for temperature uniformity. Preliminary forming results show successful forming of deep pan with Mg sheet under a limited forming window. The

new press installation at Troy Tooling Technologies is on schedule.

Task 1.7 - High-Integrity Body Castings: One anticipated outcome of the companion design exercise is the strong reliance on a substantial number of Mg alloy castings which achieve the cost-lowering ability of part integration with, however, uncertainties due to the physical strength and crashworthiness aspects of cast Mg. These attributes are further compounded by concerns regarding the inhomogeneity of large castings, for a number of reasons. Fundamentally new approaches to overcoming the traditional limitations on large castings are being studied within AMD 406 (Ultra-large Castings, see 3.C). Results and technology from that project are tangential to the conduct of AMD 604. The principal target for improved large castings within AMD 604 is the study of vacuum-assisted processes which limit the gas incorporation in die-castings, thereby, permitting structures with more homogeneous and both greater intrinsic strength as well as fatigue strength governed, in part, by microporosity. Furthermore, through proper alloy selection and processing, such large castings are envisioned to be both heat-treatable and weldable, thereby further extending their utility.
In 2007, AMD 604 enlisted participation by Contech Corporation, which undertook the adaptation of high-vacuum processing to produce structural Mg castings of improved strength and integrity. Initial trial processes with alloy AZ91D, having anticipated good castability, were at least encouraging and initial strength measurements are underway at CANMET-MTL. The expected alloy of use for most structural die castings in AM60B and it is expected that castings of this material will be forthcoming in 2008. Gibbs Die Casting was also enlisted as a participant in 2007 and a second version of a higher-vacuum assist process will be the focus of their contribution. EKK, Inc. contributed computer analysis of metal flow in the Contech process during 2007. Such modeling is expected to improve the process capability and also lead to improved homogeneity of the castings.

Task 1.8 – Joining: Joining of Mg componentry produced by any of the basic forming processes under consideration into an integrated structure is essential to the success of the Mg front-end project. While resistance and fusion welding are essential to economic steel-body fabrication, there is simply no analog for the Mg structures envisioned. The basic partitioning of approaches on an international level places largely fusion-welding processes in China; laser, resistance and friction-stir processing in Canada; and SPRs, adhesive bonding, threaded fasteners and friction spot processing in the U.S. In 2007, specific efforts directed toward adhesive bonding, SPRs and threaded fasteners were initiated and subteams formed to conduct these efforts. The Henkel Corporation and Dow Automotive were enlisted to focus on adhesive bonding and, in Henkel's case, metal pre-treatment directed thereto. A liaison with USCAR's standing fastener committee was established and potential suppliers are under consideration. A parallel effort on specialized corrosion resistant coatings for steel fasteners is underway in Task 4. SPRs will undoubtedly require some form of heat application to the deforming Mg surrounding structure to resist mechanical, as well as corrosion break-down [4]. Initial investigations of the role of Mg pre-treatment on adhesive bond strength are underway, in collaboration with the University of Michigan at Dearborn.

Conclusions

AMD 604 concluded its first year of project work with advances in both the organizational aspects of the project as well as the accumulation of initial data and predictions at the various Task levels. The companion design project AMD 603 has provided insights into preferred technologies on which to focus and the AMD 604 project is expected, in short order, to provide AMD 603 with realistic material properties and manufacturing paradigms as they emerge, including surface treatments and joining methods. A major challenge for ICME will be in the area of extrusion modeling.

Presentations/Publications

1. A. Luo, E. Nyberg, K. Sadayappan and W. Shi, "Mg Front-End Research & Development - A Canada-China-USA Collaborative Project", TMS Annual Meeting, Orlando, FL, USA, February 25 – March 1, 2007.
2. A. Luo, R. McCune, R. Beals, S. Logan, E. McCarty, J. Allison, M. Maj, D. Wagner, T. Lee, R. Osborne, L. Ouimet, J. Quinn and R. Verma, "The USAMP Mg Front-End Program

- Design and Enabling Technology Development", International Mg Association Mg in Automotive Seminar, Livonia, MI, USA, March 28, 2007.
3. A. Luo, R. McCune, R. Beals, S. Logan, E. McCarty, J. Allison, M. Maj, D. Wagner, T. Lee, R. Osborne, L. Ouimet, J. Quinn and R. Verma, "Mg Front-End Development - USAMP Activities", Society of Automotive Engineers (SAE) 2007 Congress, Detroit, Michigan, USA, April 16-19, 2007.

References

1. USAMP, "Mg Vision 2020: A North American Automotive Strategic Vision for Mg," Nov. 1, 2006.
2. USAMP AMD604 DOE Annual Report, FY 2006. A. A. Luo, E. A. Nyberg, K. Sadayappan and W. Shi, "Mg Front-End Research & Development: A Canada-China-USA Collaboration," Mg Technology 2008 Symposium of TMS, Annual Meeting, March 9-13, New Orleans, LA (in press).
3. A. Luo, R. McCune, R. Beals, S. Logan, E. McCarty, J. Allison, M. Maj, D. Wagner, T. Lee, R. Osborne, L. Ouimet, J. Quinn and R. Verma, "Mg Front-End Development - USAMP Activities", Society of Automotive Engineers (SAE) 2007 Congress, Detroit, Michigan, USA, April 16-19, 2007.
4. Y. Durandet, W. Song, S. Blacket and M. Brant, "Spot Joining of Mg Using Thermally Enhanced Self-Piercing Riveting Technology," pp.141-146 in Proc. Third Int'l. Conf. on Light Metals Technology, Sept. 24-26, St. Sauveur, Quebec, CA.

Acknowledgments

The success of this project is due to the dedicated efforts of a large number of team members at Ford, Chrysler, and General Motors, the various supplier organizations listed below, as well as the international counterparts in Canada and China. The continuing support of our respective organizations and the U.S. Department of Energy is gratefully acknowledged.

[i] Denotes project 604 of the Automotive Materials Division (AMD) of the United States Automotive Materials Partnership (USAMP), one of the formal consortia of the United States Council for Automotive Research (USCAR), set up by Chrysler, Ford, and General Motors (GM) to conduct joint, pre-competitive research and development. See www.uscar.org.

D. Self-healing Coating Systems for Corrosion Control of Magnesium Alloys

Principal Investigator: Dr. Amit Singhal
Alternate POC: Dr. Ganesh Skandan, CEO
NEI Corporation
400 Apgar Drive, Suite E
Somerset, NJ 08873
(732) 868-3141; fax: (732) 868-3143; e-mail: asinghal@neicorporation.com; gskandan@neicorporation.com

Technology Area Development Manager: Joseph A. Carpenter
(202) 586-1022; fax: (202) 586-1600; e-mail: joseph.carpenter@ee.doe.gov

Contractor: NEI Corporation
Contract No. DE-FG02-06ER84563 Small Business Innovative Research (SBIR) and Small Business Technology Transfer (STTR) Program

Objective

- The goal of the Phase I project was to develop a chromate-free coating system for protection of magnesium (Mg) alloys, which includes both the primer and the pretreatment. Through a combination of novel pretreatment formulation and additives, both barrier and self-healing characteristics were imparted to the coating. Hybrid inorganic-organic pretreatments were synthesized and deposited on AZ31B alloy test coupons and corrosion inhibiting nanoscale additives were incorporated into a commercial epoxy primer formulation and their corrosion-inhibition characteristics were studied.

Approach

- Conducted literature review on the corrosion-inhibiting pretreatment and coating systems available for protecting Mg alloys. Zirconium-, phosphate-permanganate- and silane-based pretreatments provide good adhesion, but have poor barrier properties and are highly inefficient in inhibiting corrosion of Mg alloys.
- Surface preparation of Mg before coating was studied in detail since it has a substantial influence on the corrosion resistance properties of the coating system. The cleaning process adopted from American Society for Testing and Materials (ASTM) D 1732-03 was used to prepare AZ31B alloy before depositing the pretreatment (Task 1).
- A hybrid inorganic-organic pretreatment formulation was synthesized. The formulation had large concentration of adhesive functionalities and formed a highly corrosion-resistant thin film on the metal substrate. The chemistry of the formulation was developed during the Phase I program (Task 2).
- Nanoscale additives were incorporated into the pretreatment formulation as well as a commercial epoxy primer formulation and deposited on AZ31B alloy substrates.
- Salt-water immersion, electrochemical impedance spectroscopy, direct-current (DC) polarization and adhesion tests were conducted to study the barrier and adhesive properties of the pretreatment and the self-healing properties of the nanoscale corrosion inhibitors.
- Compared the electrochemical performance of the hybrid pretreatment with chromate (DOW 1) and commercial non-chrome pretreatments.

Accomplishments

- Demonstrated that by combining the attributes of nanoparticles and hybrid inorganic-organic coatings, pretreatment coatings with excellent barrier properties can be produced. The corrosion current density of the

nanoparticle-enabled, hybrid inorganic-organic pretreatment was 0.07 μA/cm^2, while it was as high as 10 μA/cm^2 for a commercial non-chrome pretreatment on the same type of Mg alloy, AZ31B (Figure 1).

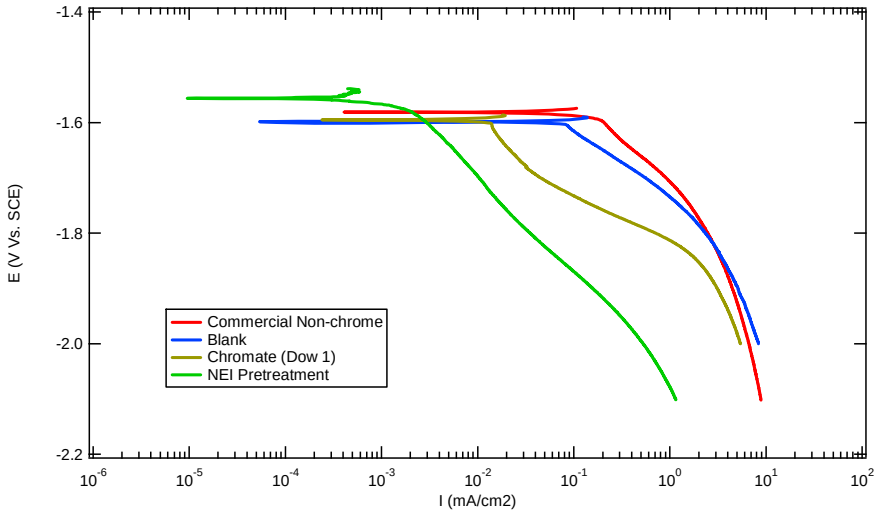

Figure 1. Cathodic polarization data of DOW 1 Chromate, a commercial non-chrome pretreatment, NEI pretreatment coatings, and uncoated AZ31B alloy. (Note that the chromate formulation was synthesized in-house following the DOW1 process).

- Observed that the corrosion current is also a function of the type of nanoscale additive. Adding about 1 wt% of Nanoparticle A in the hybrid inorganic-organic matrix does not reduce the corrosion current density. On the other hand, ~ 1 wt% of Nanoparticle B reduces the corrosion current density by an order of magnitude.

- The adhesion characteristics of the epoxy primer with the hybrid inorganic-organic pretreatment coating containing nanoscale additives are comparable to those of a commercial non-chrome as well as chromate coatings. Figure 2 shows dry and wet adhesion ASTM D4541 test data on different coatings.

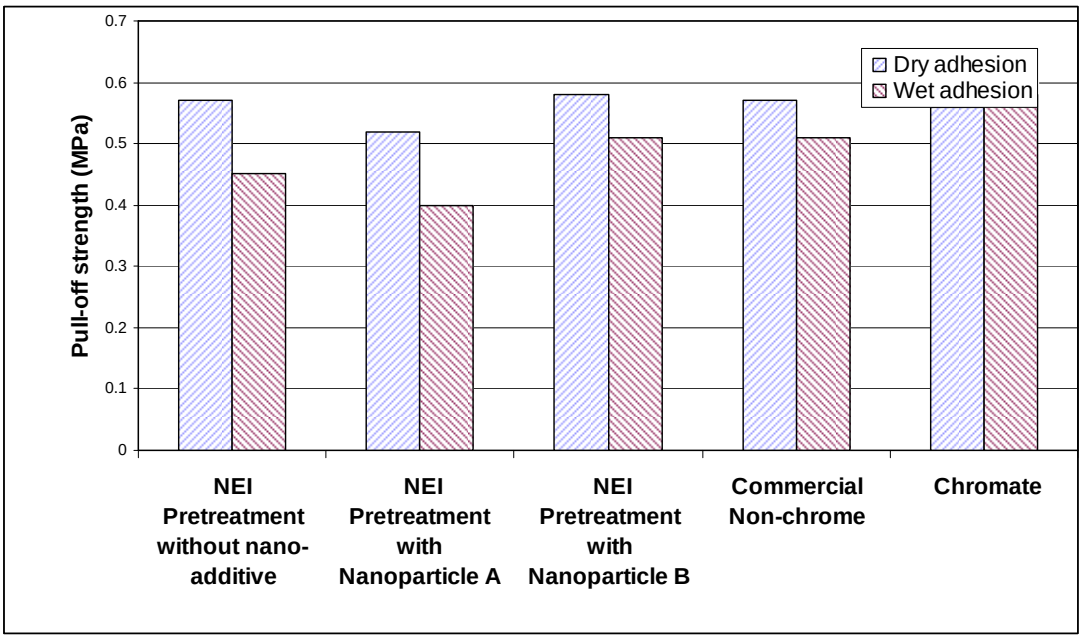

Figure 2. Adhesion strengths of an epoxy primer applied on NEI pretreatments with and without nanoscale additives, commercial non-chrome and a chromate pretreatment; before and after soaking the coated substrates in distilled water for 24 hrs.

- A commercial epoxy primer was applied on pretreated AZ31B panels. Intact primer/nanoparticle-enabled, hybrid inorganic-organic pretreatment coating exhibited higher corrosion resistance than the primer/commercial non-chrome and primer/chromate pretreatment coatings. Alternating-current (AC) impedance studies suggested that the initial low-frequency impedance of primer/NEI pretreatment containing nanoparticles was one order of magnitude higher than the control coatings. After two weeks of exposure, the low-frequency impedance of primer/ NEI's coating with nanoparticles was higher by nearly two orders of magnitude than that of primer/commercial non-chrome and comparable to primer/chromate coatings. Figure 3 compares the impedance values of the different coatings.

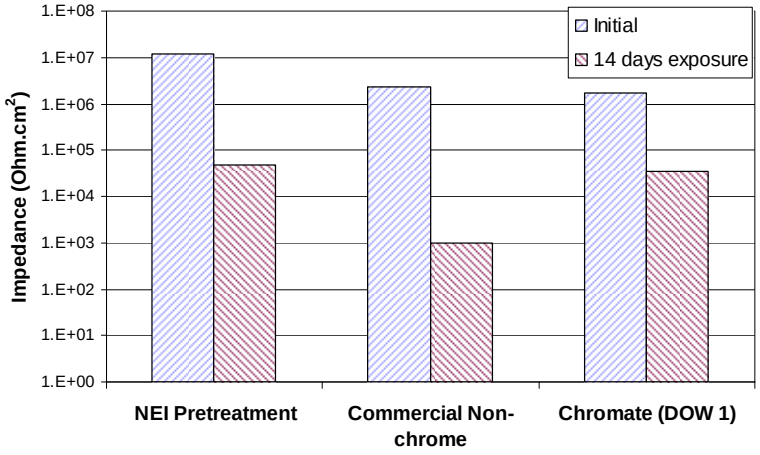

Figure 3. Low-frequency AC-impedance values of defect-free primer/pretreatment coatings for 14 days exposure to 3.5 % salt water.

- Began developing an understanding of the effect of different corrosion-inhibiting additives on the damage-responsive behavior (i.e., self-healing) of an epoxy primer coating that was applied on AZ31B panels treated with NEI's pretreatment. Defects were introduced in the coatings to expose the metal and the impedance values were measured after exposure to salt water for an hour (initial) and 11 days. Coatings containing corrosion-inhibiting nanoscale or micron-sized particles had impedance values more than an order of magnitude higher than primer coatings without additives (see Figure 4). Although we do not have any compositional evidence at this point, the increase in impedance supports the hypothesis of inhibitor particles leaching out at defect sites.

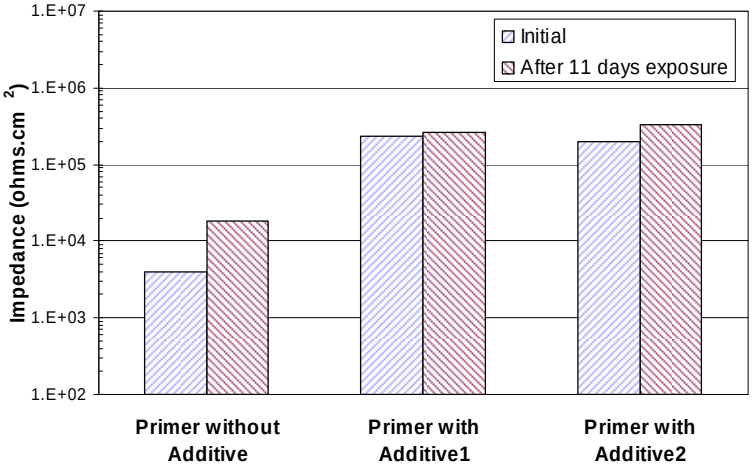

Figure 4. Comparison of low-frequency impedance after being exposed to 3.5 wt. % salt-water solution for 11 days for primers with intentionally-introduced defects.

As a result of the accomplishments of the Phase I program, we now have the opportunity to develop alternative coating architectures to impart corrosion resistance and self-healing characteristics to coatings on Mg alloys.

Nanoscale additives with the corrosion-inhibiting functionality can be added to either the pretreatment or the primer, or both.

Future Direction

- Recently, NEI Corporation has received a Phase I SBIR contract from the Department of Energy to start from July 2008 for development of chromate-free pretreatments/primer coatings systems for automotive Mg alloys. In this program, we will work towards developing a pretreatment formulation that has excellent adhesive properties and ability to exhibit damage-responsive corrosion inhibition similar to chromates. In a related program funded by the National Science Foundation, we are developing waterborne, self-healing coatings for Mg alloys.

Introduction

This Phase I project was completed in April 2007. Its goal was to demonstrate the feasibility of a non-chrome coating system, containing a pretreatment and primer that can inhibit corrosion through the use of nanoscale additives.

Task 1. Prepare Surface of AZ31B Alloys

Figure 5 shows the procedure for cleaning the panels before chemical treatment. The panels were ground with a # 320 SiC paper to remove the thick oxide layer formed on the surface. They were then immersed in n-hexane solvent and ultrasonicated for 2 minutes to remove dirt or grease from the surface. This was followed by etching the surface in an acetic acid/sodium nitrate solution for 60 seconds. This solution removed surface contamination, and a bright clean surface was obtained. The samples were rinsed in distilled water, dried and then immersed in an aqueous solution of hydrofluoric acid (HF) for surface activation. HF does not attack Mg to an appreciable extent but forms an insoluble, protective MgF_2 film. The samples were rinsed in water, dried and finally given a chemical pretreatment, followed by a spin-coating process for organic-inorganic hybrids and a dip-coating process for chromate conversion coating (DOW 1).

Task 2. Synthesize Hybrid Organic-Inorganic Pretreatment Formulation

The hybrid thin-film coating developed in the program was prepared from a hybrid inorganic-organic formulation. The pretreatment not only acts as an adhesive forming strong bonds with the metal surface, but also provides corrosion protection by forming a hard and insoluble barrier film.

Task 3. Synthesize Nanoscale Additives Functionalized with Corrosion-Inhibiting Ions

Nanoscale particles were functionalized and incorporated into the pretreatment formulation to enable them to inhibit corrosion of AZ31B alloy.

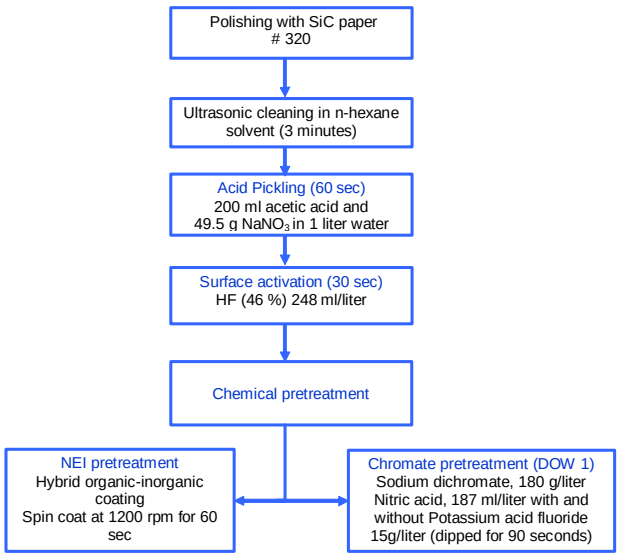

Figure 5. Surface preparation procedure of AZ31 B alloy before applying the pretreatment. (Chromate pretreatment was synthesized using the DOW 1 process).

Task 4. Perform Corrosion and Adhesion Tests on Pretreated Test Panels

Corrosion and adhesion performance tests on the pretreatment and the corrosion inhibiting nanoscale additives were performed by salt-water immersion, impedance measurements, DC polarization and pull-off adhesion tests. Additional characterization was done by

scanning electron microscopy (SEM).

Salt -Water Immersion

Figure 6 shows hybrid inorganic-organic pretreatments after 120 hours of 3.5 wt. % salt-water immersion. It is observed that the blank and commercially-pretreated AZ31B panels show general corrosion all over the surface. The chromate treatment made according to the DOW 1 process showed a lot of black corrosion products. These were chromium oxide/hydroxide formed on the surface that protects the metal from corrosion. NEI pretreatment, with and without nanoparticles, showed significantly less corrosion than the blank and commercial non-chrome pretreatment. Note that the addition of ~ 1 wt. % nanoscale particles to the NEI hybrid inorganic-organic pretreatment reduced the extent of pitting corrosion. These salt-water immersion results indicate that NEI pretreatments have considerably higher barrier and corrosion-resistance properties compared to a commercial non-chrome pretreatment. The addition of nanoscale additives further enhances the corrosion resistance of the pretreatment by reducing its porosity.

Scanning Electron Microscopy (SEM)

To understand the morphology of the commercial non-chrome and NEI pretreatment, high-resolution images using SEM were taken before and after 24 hours of salt-water immersion of the pretreated panels. As shown in Figure 7, the commercial non-chrome is not a homogeneous film. Upon exposure to 24 hours of 3.5 wt. % salt water, the treatment shows a mud-crack morphology, which also explains the general corrosion observed in the salt-water immersion test (Figure 6). NEI pretreatment shows some pores and defects which are the likely causes of pitting corrosion seen in the salt-water immersion test. The vertical lines are the polishing marks formed during the cleaning step that can be seen because of the sub-micron thickness of the pretreatment. Unlike the commercial non-chrome, NEI pretreatment does not crack and remains homogeneous upon exposure to salt water. Residual salt deposits can be seen on both the treatments (after exposure to salt water), since the panels were simply rinsed under tap water which may have not removed the salt completely.

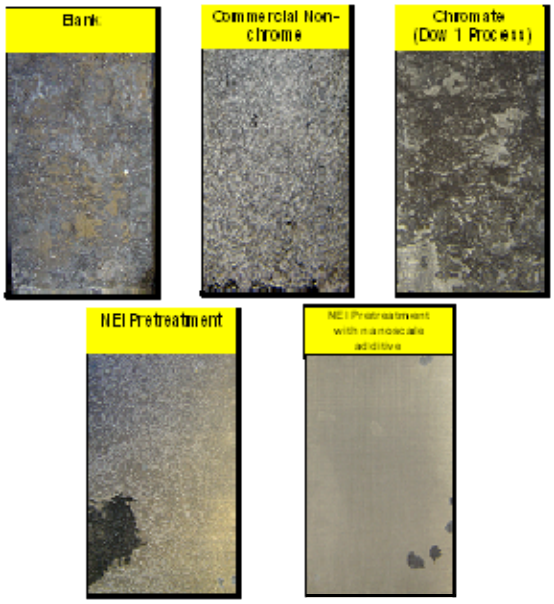

Figure 6. Pretreatments applied over AZ31 B after 120 hours of 3.5 % salt-water immersion.

Electrochemical Impedance Spectroscopy of Epoxy Primer Containing Corrosion-Inhibiting Additives

Artificial defects were introduced into the coatings and the inhibitive effect of the additives was analyzed by conducting impedance measurements over a period of 11 days. As shown in Figure 4, introduction of defects in the coating reduces the low-frequency impedance values. It is intriguing to see that the impedance values of coatings containing nanoscale particles are two orders of magnitude higher than the coating without additives. The coating without additive shows increase in impedance with time due to the formation of Mg $(OH)_2$ corrosion products. The above results are a clear indication that the addition of corrosion-inhibiting nanoscale additives has a positive effect on the corrosion performance of the commercial epoxy primer. Note that corrosion products at defect sites were visually observed for all the samples indicating that the inhibitors are not 100 % protective. More work needs to be done to improve the efficiency and quality of these materials.

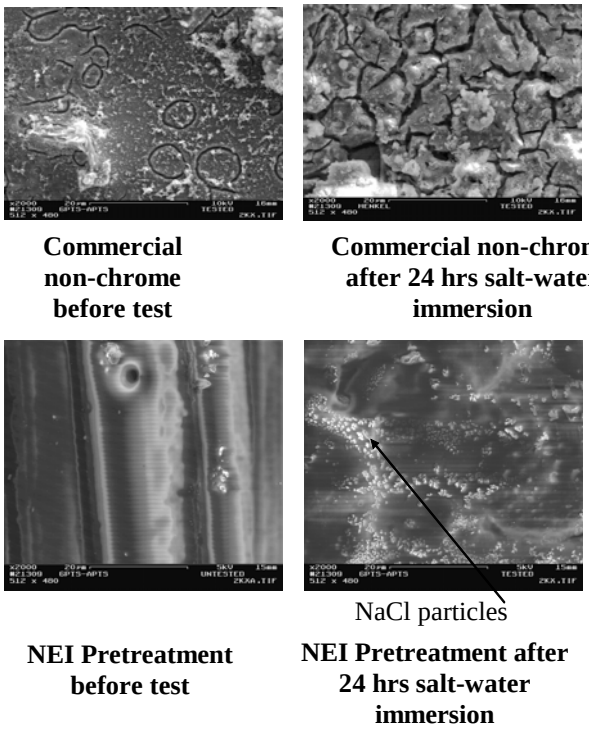

Figure 7. SEM pictures of NEI pretreatment and commercial non-chrome before and after 24 hours of 3.5 % salt-water exposure.

Adhesion of Pretreatment with Commercial Epoxy Primer

Dry and wet pull-off (ASTM D4541) was done on pretreatments under study. Wet adhesion was done after immersion of the coated panels in distilled water for 24 hours.

Figure 2 indicates that the dry adhesion values were similar for all pretreatments in the range of 0.52-0.58 MPa and, except for chromates; the wet-adhesion values were lower than the dry adhesion. For the commercial and NEI pretreatment containing nanoparticles, the wet-adhesion values were similar but 10 % lower than the dry adhesion. The wet adhesion for NEI pretreatment with and without additive was lower than the dry adhesion by 10 % and 21 %, respectively. This shows that the addition of nanoparticle B enhanced the barrier properties and decreased water penetration into the coating system. This is consistent with salt-water immersion results and cathodic polarization results, which showed that incorporation of nanoparticles enhanced the corrosion performance of NEI pretreatment. The chromate pretreatment made according to the DOW 1 process had the highest adhesion, which did not drop upon immersion in water indicating that the chromium (III) oxide/hydroxide protective film formed during the corrosion-inhibition process adheres strongly to the primer.

Acknowledgements

The author would like to acknowledge the Deportment of Energy, the sponsors of the project. We would like to thank Mr. Bob McCune for providing valuable insight into the Mg pretreatment processes and Mr. Sean Brossia of CC Technologies for conducting the electrochemical tests.

Conclusions

In Phase I, a thin, non-chromate pretreatment coating with excellent corrosion-protection ability was deposited on Mg alloy. The corrosion current of this pretreatment was at least two orders of magnitude lower than that of a commercially-available, non-chromate pretreatment. Further, it was observed that the corrosion-resistance behavior of the primer/pretreatment coating system was dependent upon the type of the corrosion-inhibitor additive in the primer coating.

Presentations/Publications/Patents

A provisional patent application has been filed with the US patent office. A full patent application will be filed soon.

E. Ferrate Conversion Coating for Corrosion Protection of High-Temperature Die-Cast Magnesium Alloys

Principal Investigator: Eric T. Clarke
Lynntech, Incorporated
7610 Eastmark Drive
College Station, Texas 77840
(979) 693-0017; fax: (979) 764-7479; e-mail: eric.clarke@lynntech.com

Technology Area Development Manager: Joseph A. Carpenter
(202) 586-1022; fax (202)586-1600; e-mail: joseph.carpenter@ee.doe.gov

---

Contractor: Lynntech, Incorporated
Contract No. DE-FG02-06ER84547 Small Business Innovative Research (SBIR) and Small Business Technology Transfer (STTR) Program

---

Objective

- Carry out a series of research studies to determine the optimum formulation for ferrate-based, corrosion-protection coatings on high-temperature diecast magnesium (Mg) alloys used in automotive powertrain applications to yield a corrosion-resistant coating comparable or better in quality than chromate-based coatings.
- Determine the corrosion resistance of the coating and its technical attributes including promotion of bonding with an organic sealant and the mechanical stability of the secondary organic coating.
- Investigate the mechanism of Mg corrosion process.

Approach

- Optimize the ferrate corrosion-protective coatings with respect to the concentration of ferrate anions and various additives and accelerators, as well as temperature, pH and time of treatment. Careful attention was given to the choice of acid-etch agents since mineral acids are known to accelerate mineralization of Mg with high rates of weight loss (Task 1).
- Expose Mg-alloy samples coated with ferrate to a 5% salt-spray corrosion resistance test and visually judge the relative extent of area covered by pit formation. Demonstrate a shift in corrosion current density (A/cm^2) using direct-current (DC) electrochemical polarization testing to show corrosion protection for the coated Mg alloy surface (Task 2).
- Evaluate adhesive properties of the secondary corrosion-protection coatings as they were supported by ferrate-based conversion coating. Adhesion evaluations were performed by cross-hatch tape test, impact-resistance test, and Taber abrasion-resistance test (Task 3).
- Characterize the chemical and metallurgical factors of corrosion for coated Mg-alloy samples using methods of scanning electron microscopy (SEM), X-ray absorption and Energy Dispersive Spectra (EDS), and high-resolution cross-sectional views of the ferrate conversion coating (Task 4).
- Assess the commercial manufacturing costs of ferrate production and document the completed project by compiling a final report inclusive of results and recommendations (Task 5).

Accomplishments

- The fiscal year (FY) 2007 Phase I accomplishments were as follows:

- Samples of Mg alloys (MRI 153M and 230D) were obtained from Dead Sea Mg, successfully sectioned, and coated at room temperature using the ferrate conversion-bath process.
- Performance of individual bath components and those in interaction with other components was evaluated in step-wise fashion using immersion conditions. A relative visual ranking system (Task 1) was used to identify useful trends of the conversion process.
- Improvements in surface sealing were noted (Task 1) when using calcium hydroxide primary sealant as compared to silicate sealant.
- Salt-fog-spray conditions (Task 2) were used to demonstrate superior corrosion protection for ferrate-converted Mg-alloy samples as compared to reference DOW 7 chromate conversion coatings, as well as for control samples prepared in the absence of ferrate.
- Similar salt-fog-spray testing of ferrate-converted Mg-alloy samples was successfully carried out for over 336 hours without formation of pits (Task 2) when the coatings were additionally sealed with a commercial varnish.
- Electrochemical-polarization tests (Task 2) were used to demonstrate a full order-of-magnitude reduction in corrosion current density (A/cm^2) for Mg alloys treated with ferrate relative to an untreated sample.
- Ferrate conversion of the Mg-alloy surfaces was shown to support the organic, varnish-type, secondary sealant film under high impact and load as demonstrated by standard mechanical testing (Task 3). Taber abrasion-resistance testing was used to show exceptional adhesion of the varnish to the converted Mg surfaces and set the stage for development of multi-layer coatings.
- Surface characterization was successfully carried out (Task 4) employing SEM methods and EDS methods. Pitted and non-pitted zones of treated Mg alloys were characterized. Non-pitted zones were clearly protected by calcium hydroxide films while pits were demonstrated to contain chlorine. Supplementary focused-ion-beam methods were used to view the coated Mg surfaces in cross-section and provide spectral analyses at higher resolution.
- Ferrate coating costs (Task 5) are projected to be affordable by original automotive parts manufacturers on the assumption that costs for scaled-up synthesis of ferrate will come down in a timely manner.
- A patent application for the ferrate conversion of Mg-alloy surfaces has been registered with the US Patent Office.

Future Direction

- The Phase I project is complete.

Introduction

The Mg Powertrain Cast Components project (see 3.B) is intended to supply lightweighting automotive Mg cast alloys to replace heavier aluminum (Al) parts in automotive manufacturing. Mg surfaces are highly reactive with respect to corrosion and must be protected by modification of their surface chemistry. Certain strong oxidizers such as ferrate, Fe(VI), are capable of modifying ("converting") the soft hydroxide film that forms on the surface of Mg to produce a harder and more protective film. Similar chromate formulations have been used successfully with Al (and other metals) to prepare surfaces for further finishing. The metallurgy of Al and Mg are similar in their oxide or hydroxide surface chemistry but differ in packing densities. The overall purpose of this study in corrosion protection of lightweighting automotive Mg diecast alloys is to evaluate the application of ferrate as an oxidizer of the soft Mg surface with respect to development of a widely-based industrial-coatings practice that protects bulk automotive Mg in a variety of structural applications and supports secondary protective films.

Immersion and salt-fog-spray corrosion testing was performed for converted alloy samples in stand-alone states and in combination with a secondary organic sealant, "RockHard" varnish. ("RockHard" varnish is produced by Indestructible Paint, Ltd., England.) Mechanical properties were determined for the varnish coating inclusive of

cross-hatch adhesion, impact resistance, and Taber abrasion resistance. Electrochemical polarizations demonstrated that the ferrate conversion coating contributed to lowering the corrosion current density at fixed potential. Electron micrographs show that converted surfaces sealed with calcium hydroxide were smooth and free of cracks. Projected costs indicate that ferrate conversion is as inexpensive as chromate without the burden of environmental risks and cleanup costs.

The results, as described below, clearly demonstrate the feasibility of a ferrate-based conversion coating for Mg. As demonstrated here, ferrate conversion coatings are at least as effective as chromate ones, without the environmental risks of chromates.

Task 1. Optimization of Ferrate Corrosion-Protective Coatings

Optimization of the corrosion-protection components in the ferrate formulations was performed with respect to the concentration of ferrate anions, the supplemental oxidant potassium permanganate and the second supplemental oxidant sodium nitrate. Hardeners such as phosphate or tungstate were optionally present in the bath. The pH of the ferrate solution was ~11.5, sufficient to stabilize the ferrate against spontaneous degradation to Fe (III). Solutions were filtered to remove impurities that remained from the ferrate production process carried out at Lynntech. Fresh ferrate solutions were replenished daily.

Samples of Mg alloys (MRI 153M and 230D) were obtained from Dead Sea Mg in the form of cast plates. Sample plates were cleaned by bead blasting to remove release-powder and dirt and then scrubbed with mild alkaline detergent to remove release-oils and grease smears. Samples were sectioned to form coupons, trued, and meticulously cleaned to remove contaminants that could have been transferred by the ensuing sanding and polishing steps. Oils and grease were removed in a manner consistent with industrial practices by employing dual washes in mineral spirit (petroleum ether) and acetone. Coupons were further degreased in an alkaline degreasing bath, rinsed, and de-oxidized using a weakly-acidic fluoride-containing bath. Immediately after stripping the surface hydroxides from the Mg samples, the coupons were rinsed and carried through a conversion and sealing sequence with the intention of replacing surface hydroxyls with iron oxometallate species as shown in Figure 1.

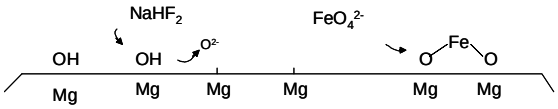

Figure 1. Schematic representation of ferrate (K_2FeO_4) conversion of Mg-alloy surface directly following cleaning and de-oxidation steps.

Results of the screenings are summarized in Figure 2 as they were obtained from a step-wise study with immersion in 5 % sodium chloride at room temperature. A relative visual ranking was used to help identify useful trends or components of the conversion process. Comparisons were made to control baths in the absence of ferrate and to reference chromate baths.

As seen in Figure 2, the common feature present in all of the combinations showing good or excellent performance is ferrate in the conversion coating and calcium hydroxide in the sealant layer. Also apparent is the fact that the ferrate conversion coatings have outperformed the chromate-based conversion coatings.

Chromate	Ferrate	Phosphate	Tungstate	Permanganate	Nitrate	Sealant: Silicate	Sealant: $Ca(OH)_2$	Protection Score
	*					*		Fair
	*	*				*		Poor
	*	*	*			*		Poor
	*			*		*		Poor
	*	*		*		*		Fair
	*	*	*	*			*	Poor
	*				*		*	Poor
	*	*			*	*		Fair
	*	*	*		*	*		Fair
	*			*	*		*	**Excellent**
	*	*		*	*		*	**Excellent**
	*	*	*	*	*		*	Poor
		*		*	*		*	Poor
		*		*		*		Fair
		*			*	*		Fair
*						*		Fair

Figure 2. Visual ranking chart for appearance of corroded coupons obtained by immersion in saline. Reference chromate was outperformed by ferrate in optimized baths.

Films obtained from boiling water or Mg hydroxide films produced in 0.01 M KOH baths were insufficient to protect Mg surfaces even with ferrate conversion treatment. Severe cleaning-bath conditions based on treatments in phosphoric acid or 10 % hydrofluoric acid were also screened out after it became apparent that these harsh condi-

tions produced rough or porous Mg-alloy surfaces. The most successful conversion baths contained components of ferrate, permanganate and nitrate.

Use of silicate as primary sealant (laid down on top of preexisting calcium hydroxide film) tends to mask the corrosion-protection results since the silicate eventually becomes opaque when exposed to sodium chloride. Use of calcium hydroxide alone may well be a better choice for primary sealant. Separate scores for corrosion-protection ranking were entered in the score chart on the basis of sealant selected. On occasion, an experiment was repeated to clarify results whenever a score could not be awarded. Worthy results obtained from the 48-hour immersion-screening process were selected for further study in long-term immersion tests or salt-fog-spray tests.

Task 2. Standard Corrosion-Resistance Testing

For purposes of salt-fog-spray corrosion testing, sample coupons of alloys MRI 153M and 230D converted with ferrate and, additionally, those coated with secondary organic sealant, "Rock-Hard" varnish, were exposed to a 5 % sodium chloride spray within a salt-fog chamber. Coupons not protected by a secondary coating of varnish were selected from the screening survey in Figure 2 and subjected to salt-fog or immersion tests for long durations, Figure 3. Silicate sealant did not perform as well as calcium hydroxide sealant under salt-fog conditions and tended to mask results obtained for the chromate reference coupons. The ferrate conversion process was superior to the reference chromate process (DOW 7) based on salt-fog-spray and immersion conditions. The appearance of the ferrate-treated specimens without an organic top-coat is better when calcium hydroxide was used as the primary sealant instead of silicate.

Figure 3. Ferrate with calcium hydroxide bath (two central samples) performed better under corrosive salt-fog conditions than silicate sealant (far left), or reference chromate treatment (far right).

The converted 230D alloys that were secondarily coated with varnish provided protection equal in level to their chromated counterparts, Figure 4.

Electrochemical-polarization testing for ferrate-coated Mg alloys provided additional corrosion-resistance information. A one order-of-magnitude reduction in corrosion current density (A/cm^2) was observed for Mg alloy MRI 153M coated with ferrate, relative to an untreated sample.

Figure 4. Secondary sealant (organic varnish) provides additional salt-fog corrosion protection. Ferrate conversion coating (left) as compared to reference chromate conversion (right).

Scans for corrosion current density and corrosion potentials were driven by CorrWare software relative to the open circuit potential (-1.5 volts) in a potential range that was selected to avoid evolution of hydrogen gas and oxygen gas (at cathodic potentials). The potentials were monitored by use of a silver/silver chloride reference electrode and a carbon working electrode, Figure 5.

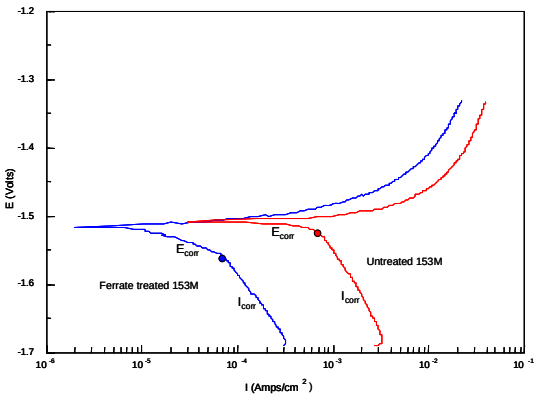

Figure 5. DC/Mg polarization of ferrate-converted Mg alloy demonstrates conclusively that ferrate is contributing to corrosion resistance for Mg.

Task 3. Mechanical Testing of Organic Varnish Coat

Adhesion of the ferrate conversion coating to the varnish secondary coating for Mg alloys was determined to fall within acceptable levels by non-specific cross-hatch tape tests and by impact-resistance tests. Excellent adhesion was determined by Taber abrasion-resistance testing (Figure 6) placing its hardness in a class comparable to polycarbonate.

Figure 6. Taber abrasion resistance for organic varnish applied to ferrate-coated Mg alloy.

Task 4. Surface Characterization of Ferrate Coatings

SEM micrographs with EDS were obtained for Mg-alloy samples coated with ferrate (and sealed with calcium hydroxide). For the SEM micrographs, the coated samples had been challenged by immersion in 5 % sodium chloride for up to three months to provide zones of pitting interspersed with pit-free zones in the coating surface. As viewed at 250X magnification, Figure 7, the pit-free zone is uniformly coated by calcium hydroxide and shows no evidence of cracking or damage. Pits (Figure 8) are sometimes observed as agglomerations of Mg hydroxide, or as dished-out areas with visible cracking.

The EDS data qualitatively reveal the presence of Mg, Al, silicon (Si), and calcium (Ca), together with other elements that are present at levels just above the baseline (Figure 9). A decrease in Al abundance (relative to Mg) may indicate that Al has preferentially dissolved away from corroded surfaces. The make-up of the corroded face more closely matches that of the untreated surface than the treated.

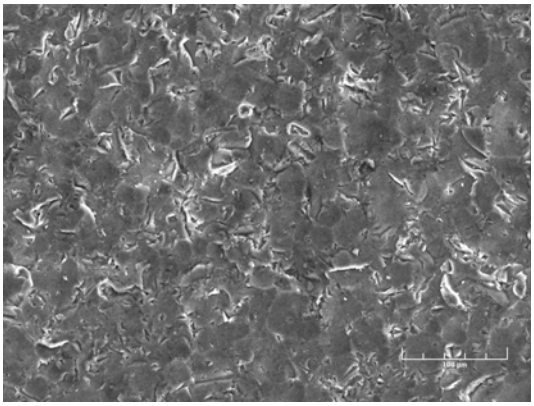

Figure 7. Unpitted zone of corroded ferrate-coated Mg alloy. Original magnification is 250X. Area of view was approximately 1 square millimeter (not to scale).

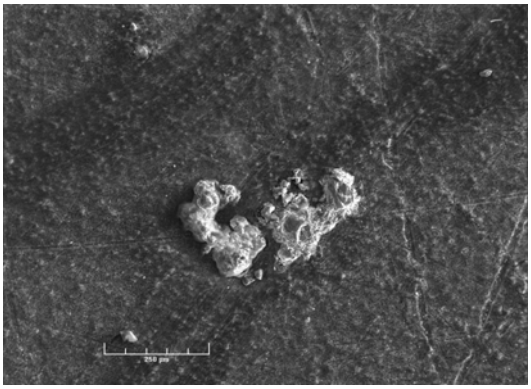

Figure 8. Surface pitting zone (agglomerations of 250 microns) for corroded Mg-alloy sample.

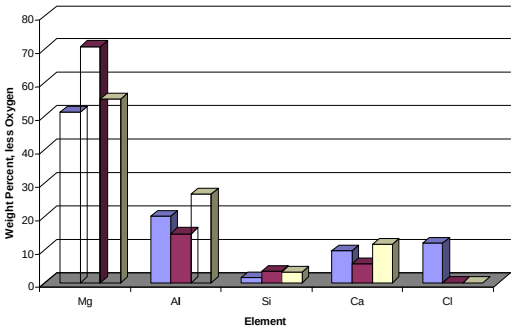

Figure 9. EDS spectral summary for ferrate-coated Mg surfaces. The distribution for each element is given in groups consisting of three different locations: pitted zones (left member of cluster), non-pitted zones (middle of cluster); and untreated zones (right member of cluster).

This indicates that the protective coating has been stripped away in this location by exposure to sodium chloride (or was never present, i.e., a defect

on the coating). The thickness of the calcium hydroxide sealant layer was 200 to 500 nm as determined by cross-sectional microscopic observations.

Conclusions

Ferrate-based conversion coatings of powertrain Mg alloys can be successfully used by original equipment manufacturers (OEMs) to provide corrosion protection to automotive Mg parts. Surface protection has been demonstrated for corrosive environments inclusive of moisture, air, and sodium chloride.

Presentations/Publications/Patents

A patent application has been filed with the U.S. Patent Office, entitled “Ferrate Conversion Coating for Mg Alloys that are used for Reduction of Vehicular Weight.”

F. Integrated Computational Materials Engineering (AMD 702 and 703[i])

Principal Investigator: John E. Allison
Ford Motor Company Research and Innovation Center
Mail Drop 3182
2101 Village Road
Dearborn, MI 48124
(313) 845-7224; fax: (313) 323-1129, e-mail: jalliso2@ford.com

Program Technical Administrator: Robert C. McCune
Robert C. McCune and Associates, LLC
5451 S. Piccadilly Cir.
West Bloomfield, MI, 48322-1446
(248) 661-0085, fax: (248) 661-8718; email: robert.mccune@sbcglobal.net

Technology Area Development Manager: Joseph A. Carpenter
(202) 586-1022; fax: (202) 586-1600; e-mail: joseph.carpenter@ee.doe.gov

Field Project Officer: Aaron D. Yocum
(304) 285-4852; fax (304) 285-4403; email: aaron.yocum@netl.doe.gov

Expert Technical Monitor: Philip S. Sklad
(865) 574-5069; fax: (865) 576-4963; e-mail: skladps@ornl.gov

---

Contractor: United States Automotive Materials Partnership (USAMP)[i]
Contract No.: DE-FC05-02OR22910 through the National Energy Technology Laboratory

---

Objectives

The primary goal of this project is the development of an Integrated Computational Materials Engineering (ICME) infrastructure for magnesium (Mg) alloy development and Mg manufacturing process optimization. This is a key enabling technology for future Mg applications, including the Mg front-end architectures of companion programs AMD 603 Magnesium Front-End Design and Development (MFEDD) and AMD 604 Magnesium Front-End Research and Development (MFERD) (see 6.B and 6.C, respectively). The following are specific objectives:

- Establishment of an international ICME infrastructure (including contributor network, knowledge-base and cyberinfrastucture) for Mg alloys in automotive structural body applications, specifically:
  - Product and manufacturing-process optimization (processes include extrusion, sheet forming and high-pressure die casting).
  - Microstructural engineering.
  - Future alloy development.
- Development of a web-based cyberinfrastructure to serve as a hub for exchanging high-quality data and models between global collaborators in academia and industry.
- Use ICME infrastructure for MFERD Phase II product and process optimization.
- Attract materials researchers into the Mg field and leverage their efforts by providing a collaborative, virtual workplace for coupling high-quality data and models.
- Advance scientific understanding in various aspects of Mg cast and wrought alloys for structural body applications, including development of processing-structure-property relationships, corrosion science, crash-energy management, fatigue performance as well as design optimization.

- Incorporate the contributions of high-quality professionals and students educated in materials science and engineering in the U.S., Canada and China.

Approach

The project, while having a single unifying theme, is divided for contractual purposes into two separate projects within the Automotive Metals Division (AMD) of USAMP. AMD 703 is a 'traditional' USAMP project, funded by Lightweighting Materials of the Department of Energy (DOE), in which original equipment manufacturer (OEM) and supplier "in-kind" efforts provide cost matching for funds provided to universities and other suppliers in support of the project goals. In the project designated AMD 702, work conducted by USAMP OEM organizations will be provided on an "in-kind" basis in support of a separate DOE cooperative agreement with Mississippi State University (MSST), wherein ICME is one part of a broader research agenda. Although the project is structurally linked to AMD 604 which has Phase 1 duration of three years, the initial projected duration of the ICME Project is intended for five years. The plan of work is outlined as follows:

- Utilize the international framework of project AMD 604 (MFERD) as a platform for enlisting the work of scientists and engineers from Canada and China.
- Develop a web-based, electronic "community of practice" allowing development and integration of multi-scale, physics-based, open-source materials models for selected properties and processes.
- Establish and verify a web-accessible, "first-principles" and CALPHAD/diffusion infrastructure database. Using such database, assess the optimization process for the predominant wrought and cast Mg alloys and likely future variants (e.g., AZ and AM alloy base).
- Processing-structure-property (PSP) relationships. Establish physics-based and/or empirical relationships for microstructural evolution and similarly-based relationships between microstructures and mechanical response of materials under stress in tension, compression, fatigue and varying strain rates. This formalism would apply to:
  - Extruded Mg components.
  - Sheet Mg components.
  - High-integrity, high-pressure, die-cast Mg components.
- Establish and demonstrate capability for multi-attribute optimization. Demonstrate capability to optimize Mg alloys, processes and components for cost and performance on one or more extruded components. Extend such capability to MFERD Phase II efforts (should they occur).
- Coordination, information dissemination and reporting. Establish overall coordinated work structure between AMD 702 (ICME A), AMD 703 (ICME B), Canadian and Chinese suppliers, and MFERD.

Accomplishments

USAMP AMD 703, Integrated Computational Materials Engineering, and the companion project AMD 702, were approved on February 14, 2007 by the AMD Board of Directors and USAMP Steering Committee, and partitioned by accounting function as indicated previously. Accomplishments for the included time period of this report are summarized as follows:

- Identified and enlisted participant organizations.
- Developed detailed program plans and individual work statements for all participants including:
  - Three U.S. universities contributing to AMD 703 (Northwestern, Michigan and Virginia).
  - MSST (AMD 702).
  - Four companies or other organizations (e.g., Materials Genomics and The Minerals, Metals and Materials Society (TMS)).
- Legal agreement with MSST largely (approx. 90%) complete.
- USAMP purchase orders entered or completed for six organizations.

- Developed interdependent plans with Canadian and Chinese participants.
- Identified model Mg alloys for ICME developments.
- Secured materials for experimental work at various universities.

Future Direction

- Finalize legal agreement between USAMP and MSST.
- Assure implementation of all outstanding USAMP purchase agreements.
- Conduct ongoing international discussions as part of the MFERD Project meeting in China in 2008.
- Assist in populating the web-based "cyberinfrastructure" platform expected to be operational at MSST during 2008.
- Focus on Mg extrusion and low-cycle fatigue behavior as early targets in the U.S. program based on MFERD needs and suitability of available data.

Introduction

The availability of low-cost, widely-distributed, massive computational power as well as near-instant worldwide communication and information sharing via the internet has enabled previously intractable scientific and engineering problems to be addressed by extensive networks of participants working in parallel. While a well-known example of such a problem is perhaps the recent unraveling of the human genome, many fields of science and technology, including materials science, are confronted with similarly complex universal challenges, which could benefit from a similar approach.

One grand challenge in materials science is the unification of the relationships between structure and properties of materials over great ranges of length and time scales extending from the atomistic level to the engineering scale, and from the fempto second to years. Figure 1 illustrates an example of such scaling ranging from atomic structure to that of an automotive engine block. The classic approach of materials science has been one of reductionism, i.e., of continually improving the understanding of structure through refinement of measuring techniques to smaller levels and accompanying theoretical models for structure and behavior at the atomic and microstructural scales. In recent years, however, a movement has emerged within the materials community to integrate knowledge over the various length and time scales through appropriate methodologies to enable an "atoms-to-engines" paradigm to develop. The Journal of Metals has published several papers describing this approach [1-3]. Figure 2 illustrates the augmentation brought to the traditional materials science and engineering pyramid of design, material and manufacturing, through application of ICME principles.

ICME is expected to play a unique role in the companion Mg front-end program insofar as providing a cyberinfrastructure "platform" to facilitate the exchange of data and methodologies to permit a focused understanding of the various processing-structure-property (PSP) relationships critical to the simultaneous engineering and manufacturing understanding of the component technologies required for the Mg front end. Two aspects of this vision are noteworthy: 1) that the scope of the undertaking is limited to a single engineering material and 2) that, because processing/property and alloy characteristics are in a continuing and rapid state of development, the use of a tool such as ICME is very appropriate for the task at hand. Thus, while Mg, *per se*, is an older engineering material compared to nickel (Ni), titanium (Ti) and aluminum (Al) alloys, the Mg system is in its infancy from the perspective of alloy development and PSP relationships. Many recent worldwide advances in physical metallurgy, alloy development, processing and manufacturing (e.g., joining, surface treatment, etc.) make its consideration for a project such as AMD 604 very appealing and, furthermore, as a particularly valuable material in meeting the FreedomCAR goals of lightweighting, cost parity with existing materials and recyclability.

Project Launch and Technical Structure Status

During 2007, the USAMP launched project AMD 703 and simultaneously negotiated an agreement with MSST to provide automotive-industry "in-kind" support to their cooperative agreement with the U.S. DOE on this particular aspect of a broader research agenda. Work conducted by USAMP OEMs on this part of MSST's program will be recorded separately as AMD 702. Much of the work conducted in this fiscal year (2007), therefore, was in completing requisite USAMP formalities for project launch while simultaneously achieving agreement with the international partners contributing to AMD 604. While AMD 703 is a stand-alone USAMP project, its goals and objectives are additionally incorporated in the U.S.-Canada-China MFERD project. Additionally, individual tasks, including the physical establishment of a cyberinfra-structure, are to be conducted as part of MSST's cooperative agreement. (See 3.E and 6.G to 6.K.)

In support of the conduct of AMD 703, a number of supplier organizations have been enlisted in addition to the participation by the OEM companies, Chrysler, Ford and General Motors. The following paragraphs report the anticipated contributions of these organizations in summary form.

Northwestern University. Professor Christopher Wolverton leads this effort to develop first-principles atomistic models for the behavior of Mg

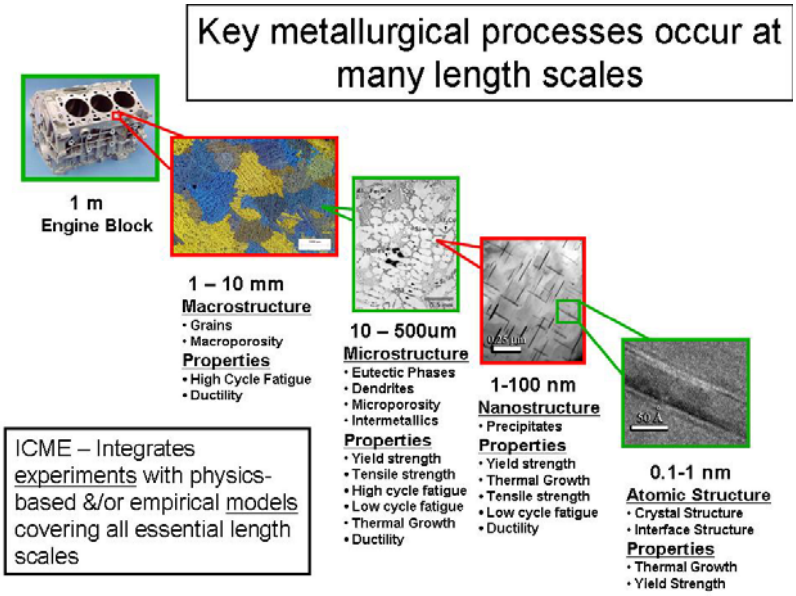

Figure 1. Atoms to engines paradigm for ICME as a unifying approach to material performance understandings beginning at the level of atomic and "nano" structural information and modeling.

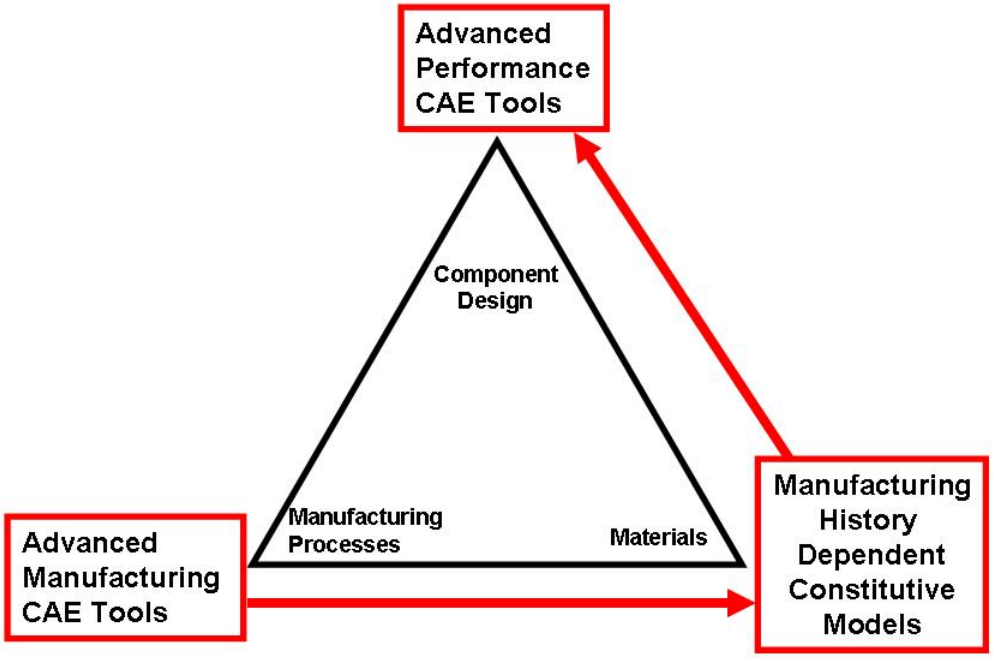

Figure 2. The ICME attributes applied to the traditional design, material and processing triangle of materials science and engineering.

and solute interactions using density functional theory (DFT). This effort will permit comparisons with more traditional phase diagram calculations, including computational methods, and measurements of both phase stability and transport properties including solute diffusion and second-phase formation.

The University of Virginia. Professor Sean Agnew will lead an effort to develop a better understanding of the role of crystal plasticity in the forming of Mg sheet, such model to include factors such as dynamic recrystallization and crystallographic textures occurring as a result of the sheet-forming processes under study. Additionally, constitutive equations and forming-limit diagrams for the thermally-enhanced deformation of Mg alloys critical to the MFERD program will be developed during the course of the project.

The University of Michigan. Professors J. Wayne Jones and Tresa Pollock will jointly conduct this project to understand and quantify the role of microstructures, as developed during the high-pressure die-casting of Mg alloys, on the subsequent yield strength and low-cycle fatigue properties of the base material and implications for the structural parts made in this fashion.

MaterialsGenome, Inc. Dr. Zi-Kui Liu, as a Professor at Pennsylvania State University, has developed computational methodologies for the determination of phase diagrams, will develop an interface that permits extensible materials thermodynamics databases to be organized and provided to third-party software programs that permit computerized calculation of alloy phase diagrams. It will provide an interface for linking the results of first-principles theory with phase-diagram calculations.

TMS. As a professional society, TMS is providing programming and a web-based portal to aid in the creation of a communications network among professionals dedicated to the subject matter of Mg science and technology and ICME.

Magma Foundry Technologies, Inc. As the supplier of the "MagmaSoft" computer program for the analysis of casting and solidification processes, Magma Foundry Technologies, Inc. will provide access and insights into application of this software for the particular purpose of "quality mapping" of castings such that projections of performance expectations based on physical models (e.g., porosity/fatigue strength) can be utilized for the structures of interest to the MFERD project. Such a capability fulfills the type of knowledge application to engineering articles envisioned by the ICME pyramid shown in Figure 2. Since many of the MFERD components are expected to be large, high-quality, Mg castings, this capability will be invaluable.

ThermoCalc Software, Inc. The use of computational methods to arrive at prediction of equilibrium phase diagrams and thermodynamic properties of alloys dates to the late 1970s. ThermoCalc is one of several software packages utilized for this purpose. The company has offered its assistance in the development of the appropriate user interfaces as proposed by MaterialsGenome, Inc. This assistance will be of value in establishing the broader links between software programs and user-populated databases within the ICME vision.

Conclusions

Integrated Computational Materials Engineering (AMD 703) was launched in early 2007 and will contain interfaces with both the AMD 604 (MFERD) project as an international focus and with the broad-based ICME effort underway through Mississippi State University. Proposals, including work plans from participating organizations have been developed and USAMP contracts have been either issued or are at various stages of the approval process. Additional "in-kind" support from candidate suppliers is welcomed and those discussions are continuing. The TMS "Magnesium" and "ICME" web portals are operational and the more specific "cyberinfrastructure" platform is expected to be finalized during fiscal year (FY) 2008. The U.S. and international teams have conducted organization meetings and technical progress by OEMs and suppliers is underway.

References

1. J. E. Allison, D. Backman and L. Christodoulou, "Integrated Computational Materials Engineering: A New Paradigm for the Materials Profession," Journal of Metals 58 [11], 25 (2006).
2. J. E. Allison, M. Li, C. Wolverton and X. SU, "Virtual Aluminum Castings: An Industrial Application of ICME," Journal of Metals 58 [11], 28 (2006).
3. D. G. Backman, D. Y. Wei, D.D. Whitis, M. Buczek, P. M. Finnegan and D. Gao, ICME at GE: Accelerating the Insertion of New Materials," Journal of Metals 58 [11], 36 (2006).

Acknowledgements

The success of this project is due to the dedicated efforts of team members at Ford, Chrysler, and General Motors, as well as the supplier organizations: The University of Michigan, The University of Virginia, Northwestern University, MaterialsGenome, Inc., Magma Foundry Technologies, Inc., ThermoCalc Software, Inc., and The Minerals, Metals and Materials Society. The project leadership also acknowledges the ongoing collaboration and discussions with colleagues at Mississippi State University. The continuing support of our respective organizations and the U.S. DOE is gratefully acknowledged.

[i] Denotes projects 702 and 703 of the Automotive Materials Division (AMD) of the United States Automotive Materials Partnership (USAMP), one of the formal consortia of the United States Council for Automotive Research (USCAR), set up by Chrysler, Ford and General Motors (GM) to conduct joint, pre-competitive research and development. See www.uscar.org.

G. Simulation-Based Design Optimization

Principal Investigator: Masoud Rais-Rohani
Department of Aerospace Engineering
Mississippi State University (MSST)
P.O. Drawer A, Mississippi State, MS 39762
(662) 325-7294; fax: (662) 325-7730; e-mail: masoud@ae.msstate.edu

Technology Area Development Manager: Joseph A. Carpenter
(202) 586-1022; fax: (202) 586-1600; e-mail: joseph.carpenter@ee.doe.gov

Contract Monitor: Aaron Yocum
(304) 285-4852; fax: (304) 285-4403; e-mail: aaron.yocum@netl.doe.gov

---

Contractor: MSST
Contract No.: 4000054701

Objective

- Develop single- and multilevel approaches for probabilistic modeling and reliability-based design optimization (RBDO) of automotive structural components and assemblies.
- Develop analytical or hybrid techniques for efficient uncertainty analysis and evaluation of component and system reliability within design optimization.
- Develop appropriate metamodels as low-cost surrogates for high-fidelity response simulations in RBDO of automotive structures.
- Develop techniques for the integration of multiscale material models in simulation-based design optimization of automotive structures related to the other tasks in the center.
- Apply the developed design methods and procedures to RBDO of automotive structural components and assemblies for the Magnesium Front-End Project (see 5.B and 5.C).

Approach

- Survey the capabilities of existing metamodeling techniques as low-cost surrogates for high-fidelity response simulations. Study the accuracy and efficiency of stand-alone and ensemble metamodels for estimation of nonlinear and noisy response functions.
- Use probabilistic modeling to describe various sources of uncertainty and their impacts on performance characteristics of a structural member or system. Investigate different approaches for RBDO of automotive structural components and assemblies. Develop RBDO formulations and solution techniques consistent with the variable nature of complexity of vehicle structures.
- Develop techniques for the integration of multiscale material models in simulation-based design optimization.
- Investigate new approaches to increase the efficiency and accuracy of structural reliability estimations. Develop analytical or hybrid techniques for evaluation of component and system reliability.
- Apply the developed design methods and procedures to RBDO of automotive structural components and assemblies.

Accomplishments

- Besides examining the performance of five different metamodeling techniques, a new technique based on optimum ensemble of metamodels was developed. Moreover, a framework for Flexible Advanced Metamodel Estimator (FAME) was established with the code currently under development by the Cyberinfrastructure project (see 6.K). (60% complete).

- Investigated a single-level RBDO methodology and its application to an automotive structural component (e.g., side rail). (50% complete).
- In collaboration with the Multiscale Microstructure-Property Plasticity Considering Uncertainty project (see 6.J), we initiated this objective ahead of the original schedule. Using the available ABAQUS UMAT subroutine for A356 cast aluminum (Al), we were able to integrate multiscale material modeling, uncertainty analysis, design optimization, and metamodeling technologies and demonstrate the new capability in design optimization of an automotive control arm. Also, in collaboration with the Materials Design for Steel Alloys project (see 5.M); we developed the approach and the associated codes for a multi-objective optimization procedure to develop modified-embedded-atom-method potentials with application to magnesium. (40% complete).
- Completed the evaluation of several methods for component-reliability analysis. Developed a new efficient method for analytical estimation of component reliability. (50% complete).

Future Direction

- Complete the multilevel approach for RBDO.
- Develop and test the performance of a new hybrid method for component and system reliability.
- Investigate a multi-attribute optimization problem which integrates product and process design into a single optimization problem.

Introduction

Simulation-based design optimization is an enabling technology that allows the design engineers to determine the best combination of product and process attributes to achieve the desired optimal performance and cost objectives while meeting the imposed design criteria. The tools necessary for design optimization of a complex system include simulation models and analysis codes that can describe the characteristics of the product and/or manufacturing process at each design point and numerical optimization techniques that can search the constrained, feasible-design space for an optimum design point. Gradient-based mathematical programming techniques are the most popular methods for the solution of general optimization problems. However, since most design optimization problems involve complex (often non-convex) design domains, gradient-based search techniques converge to a local optimum solution. Non-gradient (stochastic) search methods, on the other hand, are much less susceptible to local minimum entrapment, but they tend to be very computationally intensive and are often reserved for problems with a small number of design variables.

In this report, we will highlight our activities in different research areas under the general framework of simulation-based design optimization and describe our accomplishments as well as future direction to fulfill the remaining objectives.

Metamodeling

When response functions that appear in the objective or design constraint formulations are noisy or require computationally intensive simulations, optimizing the design becomes a very challenging task. In such conditions, surrogate mathematical models (metamodels) can offer a viable remedy.

Given the bounds on the individual input variables, a design-of-experiments (DoE) technique is used to identify the value that each input variable must take for a given experiment. By performing the computer experiments at the specified design points, a corresponding pool of response values (output) is generated. The matrix of input and output values is then used to fit or train a response surface model, which in turn can be used to estimate the value of response at any arbitrary point within the bounds of the input variables. This activity is generally known as design and analysis of computer experiments (DACE).

The common practice in the application of metamodeling techniques is to construct multiple metamodels based on a common training data set then to identify and use only the model considered the best while discarding the rest. This practice has some shortcomings as it does not take full

advantage of the resources devoted to constructing different metamodels, and it is based on the assumption that changes in the data set used to fit the metamodel will not jeopardize the accuracy of the selected model. It is possible to overcome these drawbacks and to improve the prediction accuracy of the model if the separate metamodels are combined together to form an ensemble.

As part of this research, we examined the performance of five different parametric and non-parametric metamodels for various linear, nonlinear, and noisy responses. The metamodeling techniques investigated included the global least-square method in the form of a quadratic polynomial regression (PR) [Myers and Montgomery 2002], radial basis functions (RBF) [Dyn et al. 1986; Mullur and Messac 2004], Kriging (KR) [Sacks et al. 1989; Martin and Simpson 2005; Simpson et al. 2001], Gaussian process (GP) [MacKay 1998; Rasmussen and Williams 2006; Wang et al. 2005], and support vector regression (SVR) [Clarke et al. 2005; Vapnik et al. 1997; Gunn 1997].

Furthermore, motivated by the previous research on committee of neural networks [Bishop 1995] and ensemble of surrogate models [Goel et al. 2007], we developed a more accurate ensemble methodology. This was done by modifying the general weighted average formulation and finding the optimum value for the weight factor associated with each metamodel such that a selected error metric is minimized. This methodology was successfully applied to different problems while considering different error metrics based on either the training points (i.e., cross validation errors) or a few validation points.

For evaluation of the stand-alone and ensemble of metamodels, we considered four mathematical functions (as benchmark problems) along with one car-crash example. The mathematical functions included three two-variable functions (i.e., Branin-Hoo, Camelback, and Goldstein-Price) along with the 3- and 6-variable Hartman function. In the crash problem, we considered the intrusion distance and average peak acceleration as responses of interest. We measured these responses at the driver seat, steering wheel, and the floor pan locations in a full-frontal and off-set-frontal impact simulations of a modified Partnership for a New Generation of Vehicles (PNGV) vehicle model. We used a total of nine input variables that defined the geometric shape and size of the side rails as well as the impact speed, offset distance, occupant mass, and a parameter quantifying the uncertainty in the stress-strain curve at different strain rates. All crash simulations were performed on a 32-processor IBM Linux Cluster using the nonlinear, finite-element analysis (FEA) code, LS-DYNA.

The flowchart in Figure 1 shows the steps taken in building the stand-alone and ensemble of metamodels using different techniques. In all the examples considered, the locations of the training points were obtained using the Latin Hypercube Sampling (LHS) method and maximin criterion.

The two error metrics considered are the generalized mean square error (GMSE) based on leave-one-out cross validation and the root mean square error (RMSE). Since for each metamodel, multiple replicates based on different training sets are developed, the mean value of GMSE or RMSE represent the criterion for establishing the accuracy of each model. Of the four different ensemble construction techniques identified in Figure 1, EP and EV have been developed under this research project.

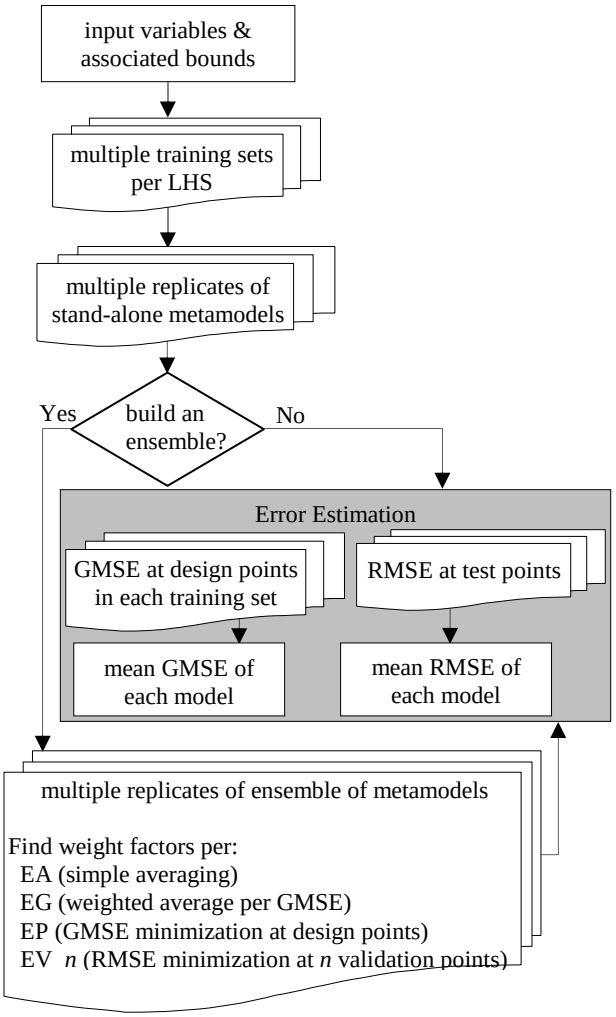

Figure 1. Flowchart of the procedure for metamodel development.

In all example problems, the best ensemble of metamodels outperformed the best stand-alone metamodel. Among the different ensemble techniques, EP proved to be the best when using GMSE as the error metric whereas EV_*n* and EG [Goel et al 2007] proved the best when using the RMSE.

The results for the full-frontal crash model are summarized in Tables 1 and 2 below. In both tables, the error for each response is normalized with respect to the stand-alone model having the lowest error among those in the same category. For example, for intrusion distance at the floor pan (ID_FP) area, GP had the lowest GMSE error among the stand-alone models whereas SVR had the greatest error (2.5 times greater than GP). Among the ensemble models, we found EP to be best overall in terms of GMSE and EV_*n* with *n* = 40 validation points to be the best with RMSE as the error metric.

Besides showing the advantage of EP and EV_*n* over other metamodels, another key finding was that a type of metamodel that accurately describes a response at one location may not necessarily show the same level of precision for the same response at another location. For example, in Table 1 for the average peak acceleration at the floor pan (A_FP), KR provides the most accurate stand-alone metamodel in terms of GMSE metric whereas, for acceleration at the driver seat (A_DS), it is the GP that is superior.

Table 1. Comparison of accuracies of stand-alone models for the full-frontal impact.

		Stand-Alone Model				
Response	Error metric	PR	RBF	KR	GP	SVR
ID_FP	GMSE	1.49	1.14	1.07	**1.00**	2.52
ID_FP	RMSE	1.44	**1.00**	1.15	1.71	2.88
ID_DS	GMSE	1.32	1.06	1.05	**1.00**	3.25
ID_DS	RMSE	1.79	**1.00**	1.39	1.30	4.82
ID_SW	GMSE	1.49	1.14	1.10	**1.00**	5.65
ID_SW	RMSE	1.99	**1.00**	1.85	1.75	11.25
A_FP	GMSE	1.50	1.09	**1.00**	1.10	1.04
A_FP	RMSE	1.36	**1.00**	1.64	1.59	2.03
A_DS	GMSE	1.40	1.03	1.07	**1.00**	1.09
A_DS	RMSE	1.28	**1.00**	1.41	1.15	1.87
A_SW	GMSE	1.16	**1.00**	1.00	1.24	1.39
A_SW	RMSE	1.70	**1.00**	1.07	1.42	2.31

Table 2. Comparison of accuracies of ensemble models for the full-frontal impact.

		Ensemble Model			
Response	Error metric	EA	EG	EP	EV_40
ID_FP	GMSE	1.13	1.05	**0.97**	1.10
ID_FP	RMSE	1.04	0.99	1.36	**0.91**
ID_DS	GMSE	1.16	1.02	**0.98**	1.02
ID_DS	RMSE	1.33	1.04	1.10	**0.94**
ID_SW	GMSE	1.50	1.05	**0.96**	1.13
ID_SW	RMSE	2.84	1.53	1.55	**1.00**
A_FP	GMSE	1.03	1.02	**0.98**	1.11
A_FP	RMSE	1.22	1.27	1.54	**0.99**
A_DS	GMSE	0.97	0.96	**0.95**	1.02
A_DS	RMSE	1.03	1.05	1.08	**0.87**
A_SW	GMSE	0.97	0.96	**0.94**	0.95
A_SW	RMSE	1.06	1.03	0.99	**0.93**

RBDO

Because of the presence of uncertainty in many aspects of product design (e.g., material characteristics, manufacturing process, operation environment, etc.), safety factors have traditionally been used to establish the design allowables. However, research shows that the use of safety factors in a deterministic design setting may not always provide the expected failure probability and that the resulting structural system may have inconsistent levels of reliability among its constituent members or modes of failure. Hence, a probabilistic approach is used to model the various sources of uncertainty and to keep track of their influences on the efficiency and robustness of the designed system.

In probabilistic design modeling, parameters that are subject to uncertainty are treated as random variables with properties (e.g., mean, standard deviation) defined by their corresponding probability distributions. Moreover, in the mathematical formulation of the design optimization problem, the objective and/or constraint functions that are influenced by uncertainty are formulated in terms of the probability of exceeding an allowable limit $P_f = P\left(G\left(\boldsymbol{X},\boldsymbol{Y}\right)<0\right)\le P_{all}$ or the corresponding reliability index $\beta = -\Phi^{-1}\left(P_f\right)$, where Φ is the cumulative distribution function of the standard normal variable.

This non-deterministic optimization approach, known as RBDO [Li and Yang 1994], has gained considerable popularity in recent years for design under uncertainty. Although the RBDO approach allows a more accurate assessment of the tradeoff between efficiency (e.g., cost, weight, performance) and safety, it is accompanied by the additional computational cost of the reliability analysis. Consequently, the solution to an RBDO problem tends to be more computationally intensive than one modeled using the traditional deterministic approach.

The RBDO formulation considered in this research is one of finding the optimal values of design variables defined by vector ***Y*** that would

$$\begin{aligned} &\text{minimize } f(\boldsymbol{Y}) \\ &\text{subject to } g_i^p(\boldsymbol{X},\boldsymbol{Y}) = 1 - \frac{\beta_i(\boldsymbol{X},\boldsymbol{Y})}{\beta_{\min}} \le 0;\ i = 1,N_p \\ &g_j^d(\boldsymbol{Y}) = \frac{R_{j_c}(\boldsymbol{Y})}{R_{j_{all}}} - 1 \le 0;\ j = 1,N_d \qquad (1) \\ &Y_k^l \le Y_k \le Y_k^u; \qquad k = 1,NDV \end{aligned}$$

where $f(\boldsymbol{Y})$ is the objective function, g_i^p designates a probabilistic constraint formulated in terms of the corresponding reliability index, β_i, and its target value, $\beta_{\min}$, and g_j^d represents a deterministic constraint that prevents the critical value of a response of interest, R_{j_c}, from exceeding its allowable value, $R_{j_{all}}$. In Eq. (1), N_p and N_d represent the numbers of probabilistic (reliability-based) and deterministic constraints, respectively, and ***X*** represents the vector of random variables in the problem.

The separation of design constraints into deterministic and probabilistic sets is meant to generalize the formulation and to help distinguish between responses that are impacted by uncertainty from those that are not. A contributing factor to the total cost of reliability analysis is the number of reliability-based constraints in the optimization problem.

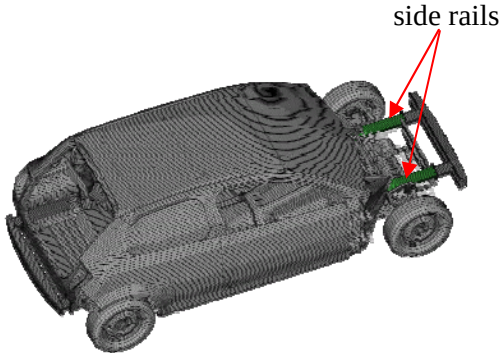

Figure 2. FE model of the vehicle.

The application problem we chose to investigate focuses on the steel side rails of a modified PNGV vehicle model as depicted in Figure 2. The selection of this particular vehicle model was to illustrate the methodology; newer vehicles and designs will be considered in the following year's work. The design criteria include limits on the intrusion distance and average peak acceleration

as measured at three remote sites (i.e., driver seat, steering wheel, and the floor pan) in the vehicle model under the full-frontal impact (FFI) and offset-frontal impact (OFI) scenarios.

Since the cross-sectional geometry of the rails can have a significant influence on their energy absorption, the selected geometric design variables permit the rail to acquire a non-prismatic shape. While the wall thickness is kept uniform, its magnitude can change during design optimization. The morphing of the cross-sectional shape requires the finite-element (FE) mesh to be modified during the design optimization. This is achieved by using the concept of geometric perturbation vectors according to the formula

$$\begin{Bmatrix} x_i^{(p)} \\ y_i^{(p)} \\ z_i^{(p)} \end{Bmatrix} = \begin{Bmatrix} x_i^{(o)} \\ y_i^{(o)} \\ z_i^{(o)} \end{Bmatrix} + \sum_{j=1}^{4} Y_j \begin{Bmatrix} x_i^{(j)} - x_i^{(o)} \\ y_i^{(j)} - y_i^{(o)} \\ z_i^{(j)} - z_i^{(o)} \end{Bmatrix} \qquad (2)$$

where subscript *i* identifies the FE node number whereas superscripts *o* and *p* refer to the original and perturbed mesh, respectively, and Y_j represents the value of the jth shape design variable.

Figure 3 shows the effect of the four shape-design variables in altering the shape of the rail on the right side of the vehicle with the one on the left side being the mirror image. Hence, depending on the optimal values of Y_1 through Y_4, the final shape of the side rail could be some combination of those shown in Figure 3.

Four elements of uncertainty are considered in this design. Here, we quantify the uncertainty in material constitutive relationship with the help of random variable, X_1. As indicated in Figure 4, X_1 defines the variability in the plastic region of the stress-strain curve at different strain rates. The markers in the graph show the range of variability in each curve within ± 3 standard deviations relative to the mean values defined by the curve itself. X_1 is assumed to have a lognormal probability distribution function with mean and coefficient of variation (COV) of 1.0 and 0.033, respectively. The second random variable, X_2, defines the collision speed with the direction of impact always perpendicular to the barrier. X_2 has a mean value of

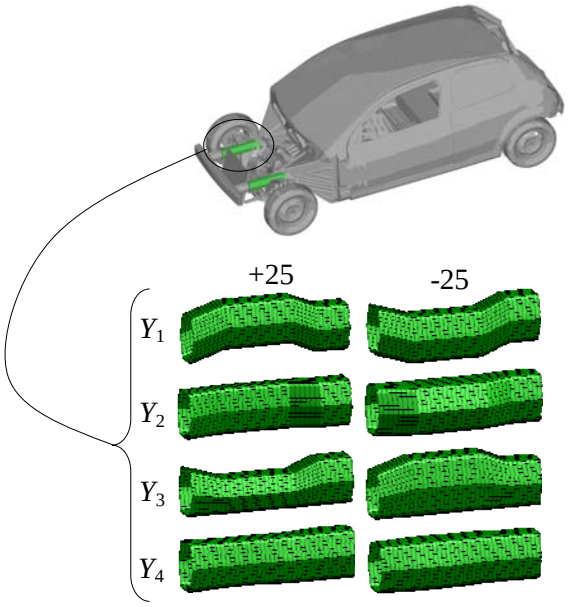

Figure 3. Perturbed geometry of the right side rail per upper and lower bounds in design variables Y_1 through Y_4.

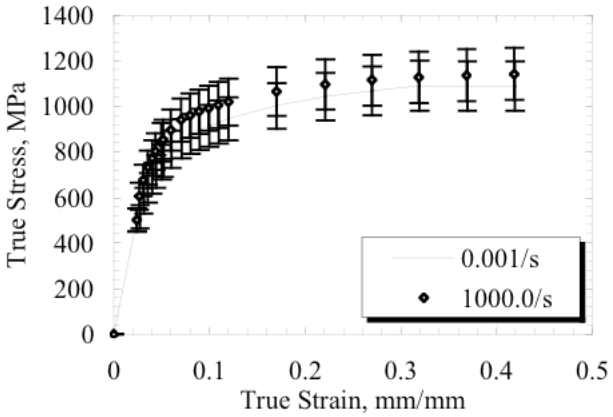

Figure 4. Band of uncertainty on the stress-strain curves at two different strain rates.

15.65 m/s (35 mph), COV of 0.067, and a normal distribution. In an OFI, only a fraction of the vehicle front end (e.g., 40%) comes in contact with the barrier. Here, the offset distance is also treated as a normal random variable, X_3, with mean and COV of 40.0% and 0.167, respectively. The last random variable, X_4, is chosen as that representing the mass of the occupant. It is also normally distributed with the mean of 136.2 kg and COV of 0.167.

In order to facilitate the integration of crash-response analysis and reliability assessment in RBDO of the side rails, we developed twelve separate metamodels that can describe the intrusion distances and average peak accelerations at three sites for the two different crash conditions. We also developed a metamodel for the mass of the side rails. The design and random variables were selected as the input variables. Based on previous experience and additional assessment, we chose to model the mass using an incomplete second-degree polynomial regression whereas the remaining 12 responses were all modeled using independent multiquadric radial basis functions.

We investigated a cadre of cases by selecting different responses as objective function and design constraints. For example, one case focused on minimizing mass while preventing all intrusion distances and accelerations from exceeding those in the baseline model whereas another considered minimizing the acceleration or intrusion distance at one location for one crash scenario while imposing upper limits on the remaining responses.

For the solution to the optimization problem in Eq. (1) we used the method of sequential quadratic programming with the reliability index analysis based on the modified advanced mean value method.

Generally, the tradeoff between performance (mass) and crashworthiness (safety) was observed in different cases. We found the constraining of responses at multiple sites imposed a far greater limit on the design of the side rail than those that simply constrained the responses at a single site. Also, the consideration of intrusion distance and acceleration under two different crash scenarios indicated the dominance of acceleration response over the intrusion distance as a design criterion.

We also investigated the influence of uncertainty on the optimum design by imposing reliability constraints on different responses while minimizing the mass of the side rail. Tables 3 and 4 give the summary of results for some of the RBDO cases we examined.
Different cases represent different constraint sets. The β_{min} value represents the largest attainable target reliability in each case. The differences in the β_{min} values give an indication of the severity of one set of design criteria compared to another. In cases 1 through 3, the intrusion distance responses are treated as probabilistic, measured in terms of the corresponding reliability index, whereas the average peak-acceleration responses are treated as deterministic.

Looking at case 1, for example, only the four responses at the driver-seat (DS) location are constrained. While the intrusion-distance constraints are probabilistic, those on average peak acceleration are treated as deterministic. Hence, the side-rail design is optimized for minimum mass solely based on the desirable characteristics at the DS location in FFI and OFI crash conditions without any consideration to responses at the other two sites. The target reliability, $\beta_{min} = 3.5$, is the largest bound that could be imposed in this problem without violating the bounds on the deterministic acceleration constraints at the same site. The optimum mass is found to be approximately 16% lighter than the baseline value. Among the unconstrained acceleration responses, only Acc_FP_F is worse (~10% higher) than that of the baseline model whereas the others are actually better. Moreover, among the unconstrained intrusion distance responses, Dis_FP_F and Dis_FP_O are better whereas Dis_SW_F and Dis_SW_O are much worse than those of the baseline model as evident by their large negative β values. At the optimal design point, the shape-design variables, Y_1 and Y_3 , are near their respective lower and upper bounds.

In cases 4 through 6, the average peak acceleration responses are treated as probabilistic, measured in terms of the corresponding reliability index, whereas the intrusion-distance responses are treated as deterministic.

In case 4, for instance, the four responses at the DS location are constrained. In comparison to the baseline model, Dis_FP_F, Dis_SW_F, and Dis_SW_O have higher values. Among the unconstrained acceleration responses, Acc_FP_O is worse while others are better than those in the baseline model. It is also interesting to note that design variables 1 and 2 are at their upper bounds.

With a β_{min} of 1.0, the optimum mass is about 18% less than the baseline value.

We also investigated the case where all twelve constraints are treated as probabilistic. In that case, the maximum-attainable β_{min} value was found to be 0.04 for a minimum side-rail mass of 2.277 lb. The optimal geometry for the side rail in cases 1 through 6 is depicted in Figure 5.

The inability to increase the target reliability value any higher than those specified in Tables 3 and 4 is mainly due to the conflicting behavior of response characteristics as a result of changes in the design variables [Rais-Rohani et al. 2006].

Table 3. Summary of RBDO results when two or more intrusion distance responses are treated as reliability-based constraints

Design Variable / Response	RBDO Solution		
	Case 1 β_{min} = 3.5	Case 2 β_{min} = 2.5	Case 3 β_{min} = 1.5
Y_1	-22.53	23.73	-2.90
Y_2	14.92	8.43	10.16
Y_3	25.0	-20.92	-13.70
Y_4	-4.28	19.54	-9.30
Y_5, mm	0.93	1.04	1.00
Opt. Mass, kg	1.95	2.49	2.41
β_Dis_FP_F	1.05	2.54[a]	1.50[a]
β_Dis_DS_F	3.50[a]	4.18	1.76[a]
β_Dis_SW_F	-5.54	-4.51	1.50[a]
Acc_FP_F, mm/s^2	447540	409410[a]	406090
Acc_DS_F, mm/s^2	667490[a]	749400	683710
Acc_SW_F, mm/s^2	429990	518630	573330
β_Dis_FP_O	0.94	2.56[a]	2.01[a]
β_Dis_DS_O	3.50[a]	2.20	1.50[a]
β_Dis_SW_O	-6.20	-2.13	1.50[a]
Acc_FP_O, mm/s^2	482710	503740[a]	528450
Acc_DS_O, mm/s^2	890820[a]	867420	103960
Acc_SW_O, mm/s^2	491840	499240	515940

Table 4. Summary of RBDO results when two or more peak acceleration responses are treated as reliability-based constraints.

Design Variable / Response	RBDO Solution		
	Case 4 β_{min} = 1.0	Case 5 β_{min} = 1.0	Case 6 β_{min} = 0.07
Y_1	25.00	-5.56	7.77
Y_2	25.00	8.83	4.19
Y_3	2.41	25.00	0.48
Y_4	-13.35	12.92	0.44
Y_5, mm	0.86	0.83	0.99
Opt. Mass, kg	1.91	1.68	2.29
Dis_FP_F, mm	63.1	60.5[a]	60.5[a]
Dis_DS_F, mm	42.3[a]	38.6	41.4[a]
Dis_SW_F, mm	10.5	13.7	9.1[a]
β_Acc_FP_F	0.22	0.99[a]	0.90[a]
β_Acc_DS_F	1.00[a]	-0.23	0.18[a]
β_Acc_SW_F	3.92	3.49	0.07[a]
Dis_FP_O, mm	67.4	67.7[a]	70.2[a]
Dis_DS_O, mm	45.2[a]	43.0	51.6[a]
Dis_SW_O, mm	7.8	9.3	6.1[a]
β_Acc_FP_O	-0.54	0.99[a]	0.07[a]
β_Acc_DS_O	1.00[a]	2.47	0.07[a]
β_Acc_SW_O	2.05	2.34	0.51[a]

[a]Response treated as a design constraint.

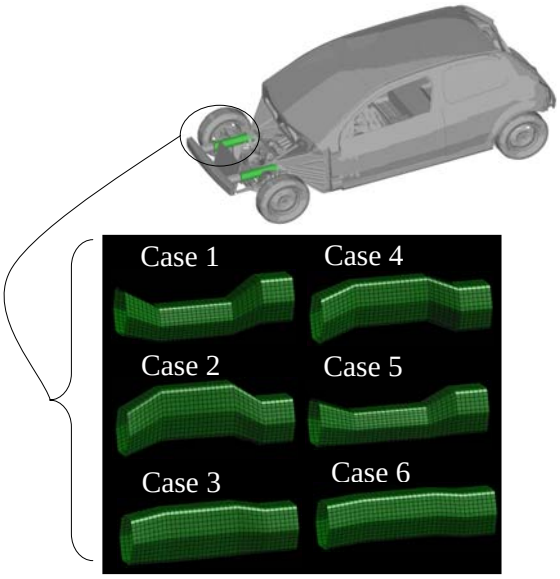

Figure 5. Optimal side-rail shapes.

Design with a Multiscale Material Model

Performance and failure of metallic components under static or dynamic loads are strongly influenced by the microstructural features (e.g., voids, cracks, and inclusion particles) of the material and their evolution during the manufacturing and in-service loading of the components. Likewise, the material microstructure characteristics depend on the type of metal, the process by which it is transformed into a product, and the environment in which the product is used.

An effective method to capture the microstructure-property relationships is by use of the internal state variable (ISV) evolution equations that are formulated at the macroscale level. The ISVs reflect the lower spatial size-scale microstructural rearrangements so that history effects can be properly modeled. With the help of such multiscale material models, it is possible to relate structural responses of interest, such as stress, strain, and toughness, to key material parameters such as particle size, interfacial strength, crack/void-density, and nearest-neighbor distance. In this study, the multiscale material model is based on the thermodynamically-constrained ISVs originally developed by Bammann et al. [1993] and later modified by Horstemeyer [2001].

Recently, Horstemeyer and colleagues [2005] investigated the effect of variability in microstructures and the boundary conditions that characterize the damage evolution using uncertainty-analysis methodology. In particular, void-nucleation, void-growth, and void-coalescence equations were evaluated and quantified in terms of sensitivity and uncertainty of various parameters in the constitutive equations. They found that a 1% uncertainty in the microstructural and boundary condition parameters results in 16% uncertainty in damage near failure, 5% uncertainty in failure strain, and 13% uncertainty in failure stress, thereby, revealing the need for incorporating uncertainties in the design process when a multiscale material model is used.

To study the influence of multiscale material modeling and associated uncertainties in an optimum design, we chose an automobile control arm as an application problem. The control arm is made of A356-T6 Al alloy, and it is manufactured using a die-cast process. This component has been selected because of the availability of data on its load-failure characteristics and the success of multiscale modeling in correctly predicting its failure mode. The two critical loading conditions considered in the design are (a) 0.8-g panic brake and (b) 0.8-g pothole strike, both of which are modeled using appropriate boundary conditions at the connection points.

Figure 6 shows the FE model of the control arm, which consists of 22,310 solid elements for 97,440 degrees of freedom. Nonlinear, static simulations of this high-fidelity model are performed using the FE code, ABAQUS implicit with multiscale-based material model incorporated using the user-defined material subroutine (UMAT).

The design optimization problem is set up similar to Eq. (1). The design variables controlling the geometry of the control arm are shown in Figure 6. These variables are used to control such features as wall thickness ($Y_1 - Y_9$), wall height (Y_{10}), and fillet radius ($Y_{11} - Y_{13}$). The arrows in Figure 6 also show the positive direction for each shape-design variable. For example, if Y_1 is positive, the corresponding wall thickness will decrease whereas, if it is negative, the wall will become thicker than that in the baseline model.

The thirty-eight constants that appear in the ISV model for an Al casting [Horstemeyer 2001] are used as random variables in the problem. They are assumed to be normally distributed with the COVs ranging from 0.05 to 0.25. In addition, there are four loading random variables that define the variability in the boundary conditions (i.e., displacements along x, y, z axes and rotation about the z axis) at the six connection points. The loading random variables are also assumed to be normally distributed with COV = 0.15.

To facilitate the integration of nonlinear FE simulation for damage evaluation with design optimization, we resorted to metamodeling. A total of six metamodeling techniques were considered in this study: Second-order response surface approximation (RS); Multiquadric RBF;

GP; KR; Feed-forward neural network (FFNN) [Smith 1993]; and SVR. All six techniques were programmed in MATLAB®.

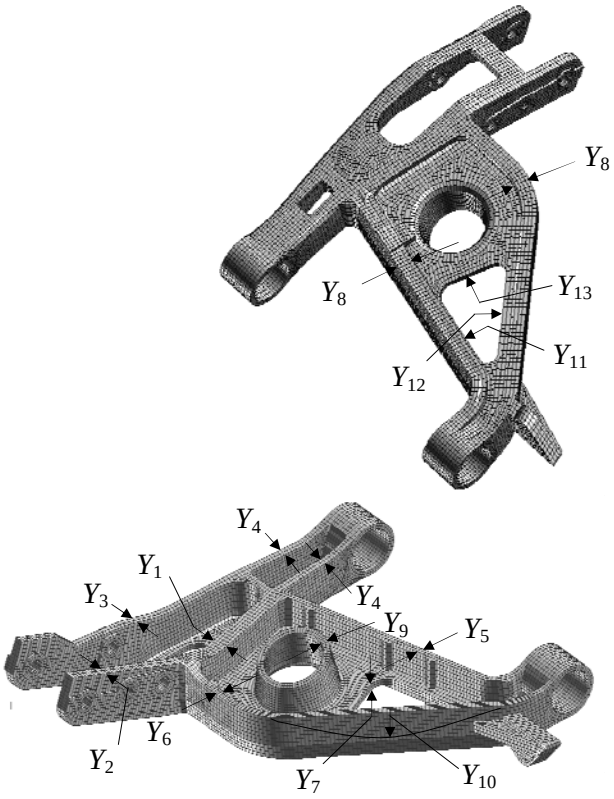

Figure 6. Description of shape-design variables.

We applied the maximin space filling technique proposed by Mourelatos et al. [2006] to generate an adequate number of training points for the metamodels as functions of the 13 design and 42 random variables. A preliminary investigation to identify and remove the subset of non-influential random variables proved inconclusive. Hence, all 42 random variables were retained.

In addition, we used variable transformation technique to increase the accuracy of metamodels, that is, instead of fitting each metamodel to damage response itself, which can vary in the range of 2.92×10^{-4} to 0.1 (three orders of magnitude variation), they were fitted to the logarithm of damage. We tested the accuracy of each metamodel for the damage response and found that the GP-based metamodel provided the most accurate predictions. High levels of noise and nonlinearity in the damage response were the main reason for GP being superior to other metamodels. These noise levels arose because of the heterogeneities arising from the microstructural differences throughout the mesh.

For von Mises stress, the GP-based metamodel again resulted in the most accurate prediction whereas, for weight, the second-order RS model was the most accurate, although the error in all weight-response metamodels was generally less than 0.2%.

Prior to solving the RBDO problem, a deterministic weight-minimization problem (case 1) was set up and solved with a design constraint imposed on the multiscale damage index. Starting with the baseline model as the initial design, the optimum design was found to be 25.3% lighter while satisfying the damage constraint. Almost all design variables were at their respective upper bounds which, in the case of wall thickness, they indicated a maximum size reduction. A post-optimization simulation of the control arm indicated that the actual value of damage was 0.0085, which was 15% less than the predicted value based on the corresponding metamodel. The ratio of the maximum von Mises stress in the optimum design to that of the baseline model was found to be 1.01 whereas the ratio for damage index was 0.112.

To investigate the influence of multiscale damage model on optimum design, we changed the design constraint from damage index to von Mises stress (case 2). Here, the upper limit on the von Mises stress was set equal to the largest value observed in case 1. Starting with the same initial design, the final weight was also found to be 25.3% lighter. This design was subsequently analyzed to find its damage index. Although this design first gave the appearance of being identical to that in case 1, it was found to have a damage index that was more than two times greater. Figure 7 provides the baseline and optimal designs together with their stress fringe plots and damage locations.

A reliability analysis on the optimum design in case 1 showed a damage reliability index of 6.48, which is already very high. However, to compare the solution with that of an RBDO problem, we set the target reliability to eight and minimized the

weight subject to a reliability-based constraint on damage.

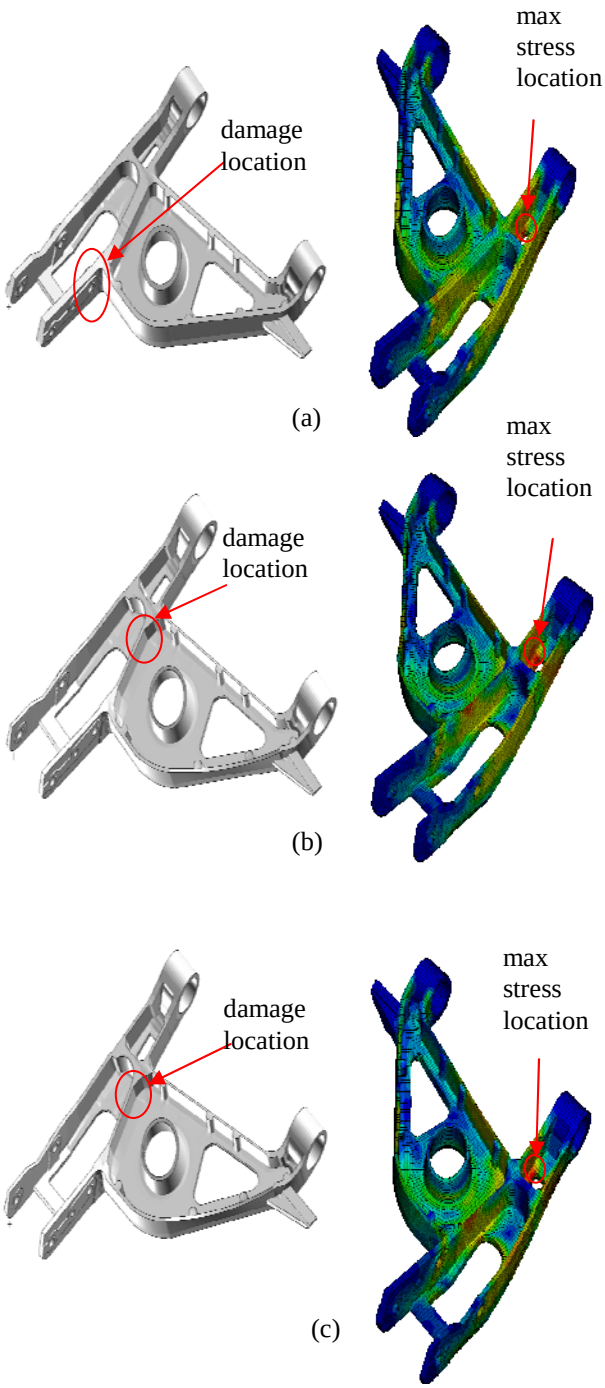

Figure 7. Comparison of (a) baseline and deterministic optimum designs using (b) multiscale and (c) plasticity models.

Not surprisingly, the optimal weight was found to be slightly heavier than in case 1. The geometry and stress plot of the reliability-based optimum design are shown in Figure 8.

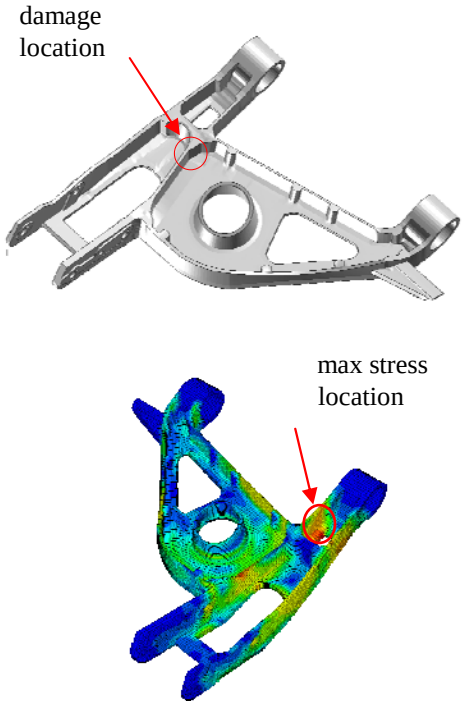

Figure 8. Optimum geometry and fringe plot of von Mises stress for the reliability-based optimum design.

A more detailed description of this study can be found in Solanki et al [2007]. In summary, we have, for the first time, documented a RDBO study that included microstructural heterogeneities in a FE simulation to predict the damage state under real-scenario design environments in order to redesign a component.

Structural Reliability

The reliability assessment of a structural component requires the evaluation of the failure probability of one or more possible failure modes. If the limit state or safety margin for a particular mode is defined by the function $G(\boldsymbol{X},\boldsymbol{Y})$, where $\boldsymbol{X}$ and $\boldsymbol{Y}$ denote the vectors of random and design variables, respectively, then safety is defined as $G(\boldsymbol{X},\boldsymbol{Y})>0$ and failure as $G(\boldsymbol{X},\boldsymbol{Y})\le 0$. The probability of failure is computed according to the multi-integral equation

$$P_f = P(G < 0) = \int_{G(\boldsymbol{X},\boldsymbol{Y})\le 0} f_X(\boldsymbol{X})d\boldsymbol{X} \quad (3)$$

where $f_X(\boldsymbol{X})$ is the joint probability density function of random variables. For most engineering problems, the analytical integration of Eq. (3) or the full distributional approach is not possible. Hence, numerical techniques such as Monte Carlo simulation, fast probability integration [Wu and Wirsching, 1987], or first- and second-order reliability methods (FORM, SORM) [Madsen et al. 1986] are often used for the evaluation of P_f or estimation of the corresponding reliability index, β. Although, depending upon the form of the limit state function and the number of random variables involved, the analytical methods tend to be less accurate than the simulation-based methods (e.g., Monte Carlo simulation, Adaptive Importance Sampling), they are more efficient especially when combined with optimization for RBDO of complex systems.

Here, we introduce a methodology for structural reliability analysis involving multidimensional and nonlinear performance functions. First, the first few statistical moments (usually the first four) of the performance function are estimated. Then, a probability distribution (preferably cumulative distribution function (CDF) or probability density function (PDF)) of the performance function is approximated with a flexible function. Finally, reliability is calculated using the approximate CDF or PDF. In this procedure, the accuracy of the reliability estimation depends on the accuracies of the estimated statistical moments and probability distribution.

Calculation of the statistical moments of a multidimensional performance function requires evaluation of multidimensional integrals. These integrals are usually simpler to compute than failure probability because the integration is not restricted to the failure domain; rather, it covers the entire random-variable space.

The dimension-reduction (DR) technique proposed by Rahman and Xu [2004] based on the additive decomposition of the response function is shown to be an efficient technique for calculating the moments of the performance function, especially when it is influenced by a moderate to large number of random variables. In DR, an N-dimensional integral of the response function is converted into N one-dimensional integrals. This approach has been successfully applied by others [Youn et al. 2006; Huang and Du 2006] in estimating statistical moments. Depending on the complexity of the response function, the one-dimensional integrals can be analytically or numerically evaluated using, for instance, the moment-based quadrature rule of Rahman and Xu [2004]. However, Youn et al. [2006] found that, for some nonlinear problems, the moment-based quadrature rule may lead to unstable moment predictions. They proposed to approximate the performance function using an approximate model (metamodel), which is then numerically integrated using one of several numerical methods.

After the statistical moments are estimated, the next step is to approximate the probability distribution of the performance function. Commonly-used distribution fitting approaches include the use of the Pearson or Johnson family of distributions, Saddlepoint approximations, and generalized lambda distributions.

The Pearson distribution has been shown to give unstable results near the boundaries of families in the skewness-kurtosis plane [Youn et al., 2006]; on the other hand, when only moment information is available, it is difficult to determine the parameters of the Johnson distribution [Johnson et al., 1995]. Furthermore, the numerical procedure followed in the Saddlepoint approximation is also prone to singularities [Huang and Du, 2006]. To avoid these difficulties, in this work we use the extended generalized lambda distribution (EGLD), which is based on the generalized lambda distribution (GLD) combined with the generalized beta distribution (GBD). After the moments of the performance function are calculated, the parameters of EGLD are computed via least -square regression. To demonstrate the performance and effectiveness of the proposed methodology for structural reliability analysis, two example problems were considered, the results for one of which are reported here.

We considered the vehicle side-impact problem [Youn et al. 2006] as one example. In this example, the crashworthiness of the vehicle is evaluated based on the velocity of the door at the B-pillar location. Youn et al. [2006] provided an explicit relationship for velocity, V_d in terms of seven random input parameters (X_1 through X_7) given as

$$V_d = 0.75 - 0.489X_1X_4 - 0.843X_2X_3 + 0.0432X_5X_6 - 0.0556X_5X_7 - 0.000786X_6^2$$

The statistical parameters of the random variables are taken from Youn et al. [2006]. Out of seven random variables, only two are normal, while the remaining ones follow beta or uniform distributions.

The reliability analysis results for this example are provided in Table 5. For evaluation of accuracy and efficiency, the proposed method (DR+EGLD) is compared with Monte Carlo simulation (MCS) and FORM. Clearly, the proposed method is very accurate as indicated by the proximity of the estimated reliability with that from MCS and is very efficient as noted by the number of function evaluations required.

Table 5. Summary of results for vehicle crash example.

Method	No. of Function Evaluations	Reliability
DR+EGLD	29	0.8071
MCS	1,000,000	0.8039
FORM	74	0.7344

The results of the example problems examined show that the methodology is computationally efficient as well as accurate for estimating the probability density functions of nonlinear performance functions and the calculation of structural reliability.

Conclusions

A summary of research progress under the general area of simulation-based design optimization was provided. Good progress has been made in the areas of reliability-based design optimization focusing on issues related to the integration of design optimization, reliability analysis, metamodeling, mesh morphing, and vehicle-crash simulations; metamodeling of nonlinear and noisy responses; design optimization using a multiscale material model; and an analytical method for accurate and efficient evaluation of structural reliability. Research activities have resulted in a number of technical papers and presentations.

Presentations/Publications/Patents

1. Rais-Rohani, M., Solanki, K., and Eamon, C., "Reliability-Based Optimization of Lightweight Automotive Structures for Crashworthiness," Proceedings of the 11th AIAA/ISSMO Multidisciplinary Analysis and Optimization Conference, Portsmouth, VA, Sep 6-8, 2006.
2. Rais-Rohani, M., "On Shape and Sizing Optimization of Automotive Structural Components for Crashworthiness," VR&D Optimization Users Meeting, Monterey, CA, Oct 30-31, 2006. (presentation only)
3. Rais-Rohani, M., "Reliability-based Design Optimization of Automotive Structures for Improved Crash Performance," TMS 2007 Annual Meeting, Orlando, FL, Feb 25 – Mar 1, 2007. (presentation only)
4. Solanki, K., Acar, E., Rais-Rohani, M., Eamon, C., Horstemeyer, M., "Reliability-Based Structural Optimization using a Multiscale Material Model," Proceedings of the 48th AIAA/ASME/ ASCE/AHS Structures, Structural Dynamics and Materials Conference, Honolulu, HI, Apr 23-26, 2007.

References

1. Bammann, D. J., Chiesa, M. L., Horstemeyer, M. F., and Weingarten, L. I., Failure in ductile materials using finite element methods, Structural Crashworthiness and Failure, edited by T. Wierzbicki and N. Jones, Elsevier Applied Science, The Universities Press (Belfast) Ltd., 1993.
2. Bishop, C.M., 1995, "Neural Networks for Pattern Recognition," Oxford University Press Inc., New York, NY, pp. 364-369.
3. Clarke, S.M., Griebsch, J.H., and Simpson, T.W., Analysis of Support Vector Regression for approximation of complex engineering

analyses, ASME Journal of Mechanical Design, Vol. 127, No. 11, 2005, pp. 1077-1087.
4. Dyn, N., Levin, D. and Rippa, S., Numerical procedures for surface fitting of scattered data by radial basis functions, SIAM Journal of Scientific and Statistical Computing, Vol. 7, No. 2, 1986, pp. 639-659.
5. Goel, T., Haftka, R.T., Shyy, W., and Queipo, N.V., "Ensemble of Surrogates," Structural and Multidisciplinary Optimization, Vol. 33, No. 3, 2007, pp. 199-216.
6. Gunn, S. R., Support Vector Machines for classification and regression, Technical Report, Image Speech and Intelligent Systems Research Group, University of Southampton, UK, 1997.
7. Horstemeyer, M.F., From Atoms to Autos, A new design paradigm using microstructure-property modeling, Part 1: monotonic loading conditions," Sandia National Laboratories, Sand2000-8662, March 2001.
8. Horstemeyer, M.F., Solanki, K. and Steele, W.G., Uncertainty methodologies to characterize a damage evolution model," Plasticity Conference, 2005.
9. Huang, B., and Du, X., "Uncertainty Analysis by Dimension Reduction Integration and Saddlepoint Approximations," Journal of Mechanical Design, ASME, Vol. 126, No. 1, 2006, pp. 26-33.
10. Johnson, N.L., Kotz, S., and Balakrishnan, N., "Continuous univariate distributions," Vol. 2, 2nd Edition. John Wiley, New York, 1995.
11. Li, W. and Yang, L, "An Effective Optimization Procedure Based on Structural Reliability," Computers and Structures, Vol. 52, No. 5, 1994, pp. 1061-1067.
12. MacKay, D.J.C., Introduction to Gaussian Processes, Neural Networks and Machine Learning, edited by C.M. Bishop, Vol. 168 of NATO ASI Series, Springer, Berlin, 1998, pp. 133-165.
13. Madsen, H. O., Krenk, S., and Lind, N. C., Methods of Structural Safety, Prentice Hall, Englewood Cliffs, NJ, 1986.
14. Martin, J.D., Simpson, T.W., Use of Kriging models to approximate deterministic computer models, AIAA Journal Vol. 43, No. 4, 2005, pp. 853-863.
15. Mourelatos, Z.P., Kuczera, R.C., and Latcha, M., An efficient Monte Carlo reliability analysis using global and local metamodels, Proceedings of 11th AIAA/ISSMO Multidisciplinary Analysis and Optimization Conference, Portsmouth, VA, 6-8 September 2006.
16. Mullur, A.A. and Messac, A., Extended radial basis functions: more flexible and effective metamodeling, Proceedings of 10th AIAA/ISSMO Symposium on Multidisciplinary Analysis and Optimization, August 30 – Sept 1, 2004, Albany, New York.
17. Myers, R.H., and Montgomery, D.C., Response surface methodology: process and product optimization using designed experiments, Wiley, New York, NY, 2002.
18. Rahman, S., and Xu, H., "A Univariate Dimension-Reduction Method for Multi-dimensional Integration in Stochastic Mechanics," Probabilistic Engineering Mechanics, Vol. 19, 2004, pp. 393-408.
19. Rais-Rohani, M., Solanki, K., and Eamon, C., "Reliability-Based Optimization of Lightweight Automotive Structures for Crashworthiness," Proceedings of the 11th AIAA/ISSMO Multidisciplinary Analysis and Optimization Conference, Portsmouth, VA, Sep 6-8, 2006.
20. Rasmussen, C.E., and Williams, C.K.I., Gaussian Processes for Machine Learning, The MIT Press, 2006.
21. Sacks, J., Welch, W. J., Mitchell, T. J. and Wynn, H. P., Design and analysis of computer experiments, Statistical Science, Vol. 4, No. 4, 1989, pp. 409-435.
22. Simpson, T.W., Mauery, T.M., Korte, J.J., and Mistree, F., 2001, Kriging models for global approximation in simulation-based multidisciplinary design optimization, AIAA Journal, Vol. 39, No. 12, pp. 2233-2241.
23. Smith, M., Neural Networks for statistical modeling, Von Nostrand Reinhold, New York, 1993.
24. Solanki, K., Acar, E., Rais-Rohani, M., Eamon, C., Horstemeyer, M., "Reliability-Based Structural Optimization using a Multiscale Material Model," Proceedings of the 48th AIAA/ASME/ ASCE/AHS Structures, Structural Dynamics and Materials Conference, Honolulu, HI, Apr 23-26, 2007.

25. Vapnik, V., Golowich, S., and Smola, A., Support Vector Method for function approximation, regression estimation, and signal processing, Advances in Neural Information Processing Systems, edited by Mozer, M., Jordan, M., and Petsche, T., MIT Press, Cambridge, MA, 1997, pp. 281-287.
26. Wang, L., Beeson, D., and Wiggs, G., Gaussian Process metamodels for efficient probabilistic design In complex engineering design spaces, ASME 2005 International Design Engineering Technical Conferences & Computers and Information in Engineering Conference, Long Beach, CA, September 2005.
27. Wu, Y.-T. ad Wirsching, P. H., "New Algorithm for Structural Reliability Estimation," ASCE Journal of Engineering Mechanics, Vol. 113, No. 9, 1987, pp. 1319-1336.
28. Youn, B.D., Xi, Z., Wells, L.J., and Wang, P., "Enhanced Dimension Reduction (EDR) Method for Sensitivity-Free Uncertainty Quantification," Proceedings of the 11th AIAA/ISSMO Multidisciplinary Analysis and Optimization Conference, Portsmouth, VA, Sep 6-8, 2006.

H. Fatigue of Lightweight Automotive Materials

James C. Newman, Jr.: Co-Principal Investigator
314C Walker Engineering Building
Mississippi Sate University (MSST)
P.O. Box A
Mississippi State, MS 39762
(662) 325-1521; fax: (662) 325-5433; e-mail: j.c.newman.jr@ae.msstate.edu

Yibin Anna Xue: Co-Principal Investigator
Assistant Research Professor, Center for Advanced Vehicular Systems (CAVS)
MSST
Mississippi State, MS 39762-5405
(662) 325-5450; fax: (662) 325-5433; e-mail: axue@cavs.msstate.edu

Mark F. Horstemeyer
CAVS Chair in Solid Mechanics & Professor, Mechanical Engineering
MSST
206 Carpenter Bldg., PO Box ME
Mississippi State, MS 39762
(662) 325-7308; fax: (662) 325-7223; e-mail: mfhorst@me.msstate.edu

Paul T. Wang
Manager, Computational Manufacturing and Design
CAVS
MSST, P.O. Box 5405
Mississippi State, MS 39762-5405
(662) 325-2890; fax: (662) 325-5433; e-mail: pwang@cavs.msstate.edu

Technology Area Development Manager: Joseph A. Carpenter
(202) 586-1022; fax: (202) 586-1600; e-mail: joseph.carpenter@ee.doe.gov

Contract Monitor: Aaron Yocum
(304) 285-4852; fax: (304) 285-4403; e-mail: aaron.yocum@netl.doe.gov

---

Contractor: MSST
Contract No.: 4000054701

Objective

- Our objective is to develop and experimentally validate prognostic tools for in-service life prediction and fatigue design of lightweight automotive materials and components. An extensive test program is being conducted on AZ31D Mg-alloy extrusions. Two fatigue models are being developed. The first is the multistage fatigue (MSF) model, which considers life to be composed of incubation, microstructurally and physically small-crack growth, and large-crack growth; and the second model, Small-Crack Theory, is based on small- and large-crack propagation alone, which assumes that micro-cracks (1 to 300-μm in size) initiate very early in the fatigue life from microstructural features (no incubation life).

Approach

- Develop methodologies for simulating microstructurally and physically small cracks in selected Mg alloys. Observation of the incubation lives for the selected Mg alloys, measurement and correlation of the growth of microstructurally and physically small cracks and large-crack behavior will be conducted for development of the physics-based models (Task 1).
- Perform literature survey on fatigue and small-crack behavior in Mg alloys; conduct fatigue and crack-growth tests on selected Mg alloys; conduct monotonic and cyclic stress-strain tests, uniaxial and multi-axial fatigue tests on AZ31; conduct "Round Robin" fatigue tests on AM30 Mg alloy under the leadership of General Motors (GM) for the United States Council for Automotive Research (USCAR); and use Mg fatigue data from the Fatigue and Durability Research Test 3 in the Mg-front-end project (5.C) to validate the models (Task 2).
- Perform *in-situ* scanning electron microscope (SEM) fatigue tests on selected alloy(s) to identify crack-initiation site(s) and metallurgical features. We will conduct in-situ studies on the fatigue and crack behavior of the selected Mg alloy (Task 3).
- Correlate the influence of grain boundaries, crack shapes and plasticity effects on the fatigue models. We will conduct microstructural studies on the influence of grain boundaries on crack growth and the effects of plastic deformations on the fatigue and fatigue-crack-growth behavior (Task 4 and collaboration with the optimization task in the Center for Virtual Manufacture and Design (CVMD).
- Experimentally validate the models with a selected material and non-proprietary, automotive component tested under in-service loading specified by sponsors (Task 5).

Accomplishments

- Conducted literature surveys on fatigue and small-crack growth in Mg alloys (Task 2).
- Developed a detailed statement of work (SOW) on "Development of Microstructure-Based Multistage Fatigue Models for Alloys Utilized in Automotive Mg Front End Project" (Task 2).
- Developed test matrix and test specimens for tensile and fatigue tests on the Mg alloys to determine material parameters for the MSF and Small-Crack Theory models (Task 2).
- Conducted MSF analyses of cast AZ91 material and components (Task 1).
- Conducted preliminary fatigue-crack-growth analyses and correlations of crack-growth rates for AZ91E to determine material parameters for Small-Crack Theory model (Task 1).
- Conducted fatigue analyses on unnotched strain-controlled tests on AZ91E coupons using Small-Crack Theory (Task 1).
- Acquired two AZ31D extrusions from General Motors (GM) (Task 2).
- Determined composition and particle morphology and distributions for AZ31D Mg alloy from GM (Task 2).
- Developed a detailed test plan for the tensile and fatigue specimens to be machined from AZ31D extrusions (Task 2).
- Initiated tensile testing on the extruded AZ31D alloy (Task 2).
- Submitted an abstract to TMS 2008 on fatigue of Mg AZ31 (Task 1).

Future Direction

- Evaluate and model fatigue behavior of self-piercing rivet (SPR) lap-joint configuration (May 2008).
  - Develop candidate SPR specimen.
  - Uniaxial tensile strain-life testing ($R > 0$).
  - Microstructural evaluations.

- Evaluate and model fatigue behavior of Mg AZ31D extrusions (August 2008).
  - Evaluate grain size, orientation and distribution for AZ31 Mg alloy.
  - Conduct fatigue-crack-growth tests on compact specimens made of AZ31 alloy.
  - Complete the monotonic and cyclic stress-strain tests on the AZ31 extrusion.
  - Conduct uniaxial strain-life test with mean stress effects (stress ratios R = -1 and R = 0.1).
  - Evaluate fractographs of fatigue specimens, identify incubation site(s), and fatigue stages.
  - *In-situ* SEM tests on AZ31 coupons to study fatigue incubation and crack-growth behavior (collaboration with Chinese partners).
  - Perform MSF analyses of the uniaxial, strain-controlled, fatigue tests on unnotched AZ31 coupons.
  - Perform Small-Crack Theory analyses of the uniaxial, strain-controlled, fatigue tests on unnotched AZ31 coupons.
- Fatigue components design (starting May 2008)
  - Obtain in-service spectrum loading sequence from the automotive industry.
  - Conduct MSF and Small-Crack Theory fatigue analyses under in-service, variable-amplitude loading.
- Publications and reports
  - Submit a paper on the fatigue analysis of the AZ91E alloy using Small-Crack Theory to International Journal of Fatigue (December 2007).
  - Complete a paper for MTS 2008 on fatigue of AZ31 (December 2007),
  - Complete a full report on fatigue analyses of AZ31D under constant- and variable-amplitude loading (August 2008).

Introduction

Prognostic tools for in-service life prediction of lightweight automotive materials and components are being developed and validated for Mg alloys. An extensive test program is being conducted on AZ31D Mg alloy from extrusions obtained from the automotive industry. Monotonic and cyclic stress-strain tests and fatigue tests under low- and high-cycle fatigue conditions are being conducted. Detailed observations of the fatigue-failure process will guide the development of the physics-based models. Two fatigue models are being developed using the extensive test program, a USCAR Round Robin, and other tests from the automotive consortium.

The first model is the MSF model, which considers life to be comprised of incubation, microstructurally and physically small-crack growth, and large-crack growth regimes. Material parameters in the MSF model will be evaluated from the extensive test program. The second model, Small-Crack Theory, based on small- and large-crack growth alone, assumes that microcracks (1 to 300-μm in size) initiate very early in the fatigue life from microstructural features (no incubation life). Fatigue-crack-growth tests will provide basic material properties from threshold to fracture and a crack-closure model will be used to correlate and predict the fatigue behavior. Both models will be validated by test coupons and automotive components.

MSF Model

The MSF approach [1] decomposes fatigue life into four consecutive stages (that we break down into three stages) based on the microstructural details of fatigue crack growth, similar to the approach summarized by Suresh [2], i.e.,

$$N_{\text{Total}} = N_{\text{Inc}} + N_{\text{MSC/PSC}} + N_{\text{LC}}, \quad (1)$$

where N_{Total} is the total fatigue life; N_{Inc} is the number of cycles to incubate a crack at a micronotch or a microscale discontinuity that nucleates crack-like damage and earlier crack propagation through the region of the micronotch root influence; N_{MSC} is the number of cycles

required for propagation of a microstructurally small crack (MSC) with the crack length, $a_i < a < k$ MS, with MS defined as a characterized microstructural length scale of interaction with microstructural features; N_{PSC} is the number of cycles required for propagation of a physically small crack (PSC), k MS < a < O (10 MS), during the transition from MSC status to that of a dominant long crack (LC). Depending on the microstructural inclusion morphology, texture of the matrix and loading, the PSC regime may extend to 200 ~ 800 μm in the high-cycle fatigue (HCF) regime. In Equation (1), the MSC and PSC regimes are combined into one mathematical form. The number of cycles required for LC propagation is given by N_{LC}. In McDowell *et al*. [1], MS was defined as the dendrite cell size (DCS) for cast Al alloys, k on the order of 1-3 as the nondimensional factor that is representative of a saturation/percolation limit for the three-dimensional crack front encountering a set of microstructural obstacles to propagation. When considering the MSF model for the low-cycle fatigue (LCF) and HCF regimes of Mg alloys for automobile component applications [3], MS was also defined as the DCS; however, k was found to be higher in certain cases due to large gas pores (on the order of 10 μm) and the refined DCS (on the order of 5~10 μm) acted as a site of crack formation. For extruded Mg alloys, the MS will primarily represent the average grain size.

Figure 1 shows a schematic of three distinct regions of the constant-amplitude, completely-reversed uniaxial strain-life [4]. In this plot, the length scale, 'D' , pertains to the diameter of the inclusion, i.e., a typical particle or a gas pore for the case. The length scale, l , pertains to the size of the plastic zone at the micronotch root, defined as the scale over which the local plastic shear strain is greater than or equal to 0.01%. The constrained microplasticity regime is defined by the l/D ratio at which l/D is linearly varying with respect to the applied strain amplitude corresponding to the HCF regime. We can make the connection that macroscopic plasticity (hysteresis in the global stress-strain curve) is apparent when the local microplasticity develops past the constrained state – we define this as the domain of unconstrained microplasticity. Hence, we introduce a percolation limit for microplasticity through the microstructure as the transition away from the linearity. Eventually, as l/D approaches unity, the plasticity becomes extensive and the macroscopic state of cyclic plasticity, as measured in test specimens, is virtually indistinguishable from the connected microplasticity – we term this as the regime of limited plasticity corresponding to the LCF regime. Note that constrained microplasticity exists even below the macroscopic yield point, which leads to the formation and growth of fatigue cracks.

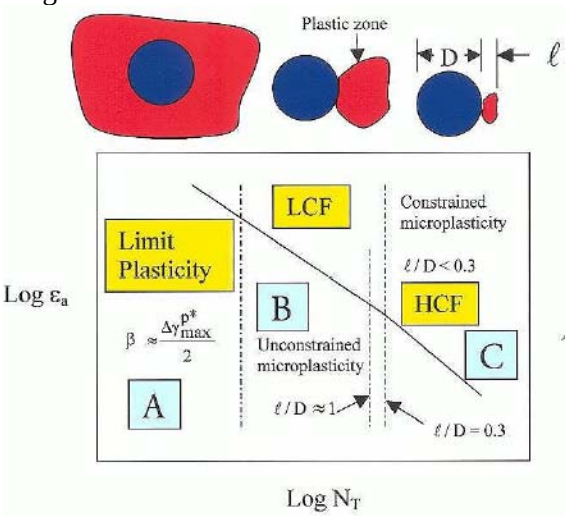

Figure 1. Regimes characterizing cyclic microplasticity at particles and casting pores: (A) elastic-plastic fracture mechanics (EPFM) crack-propagation-dominated, (B) transition regime, and (C) incubation-dominated (l/D = *0.3* is for A356 Al alloy).

Modifications of MSF Model for Cast Mg Alloys

Most of the fatigue damage formed at large casting pores near or at the edge of the specimens. Since the sizes of the casting pores dominated the fatigue life, the effect of the inclusion size was incorporated into the incubation model in a stronger fashion. The damage formation site often exhibited a region with relatively higher porosity when compared to the rest of the specimens. Therefore, the porosity affected fast-crack growth in the MSC/PSC regime and was incorporated into the crack-tip displacement.

The nonlocal maximum shear strain range at the micronotch, β, can be estimated using micro-mechanics analysis of a representative volume cell with a nonlocal averaging procedure [5],

$$\beta = \frac{\Delta\gamma^P_{\max}}{2} = Y\left[(\varepsilon_a - \bar{\varepsilon}_{th})\right]^q, \qquad \frac{l}{D} \le \eta_{\lim} \qquad (2a)$$

$$\beta = \frac{\Delta\gamma^P_{\max}}{2} = Y\left(1 + \xi\frac{l}{D}\right)\left[(\varepsilon_a - \varepsilon_{th})\right]^q, \ \eta_{\lim} < \frac{l}{D}, \qquad (2b)$$

where, Y, q, $\eta_{\lim}$ are material and microstructure-related parameters obtained using micro-mechanical simulations at inclusions. Parameter Y depends on the remote load ratio; based on finite-element analysis for A356 Al alloy, it was assumed

$Y = \left[y_1 + (1+R)y_2\right]\left(\frac{D}{D_0}\right)^{d'}$ with y_1 and y_2 as constants.

D_0 is the diameter of the pore in the specimen that caused fatigue failure and d' depicts the effect of pore size on the local plastic strain, which is taken as $0.1 < d' < 0.6$.

The crack-tip-opening displacement is related to the remote loading as,

$$\Delta CTD = f(\bar{\phi})g(\phi)C_{11}\left(\frac{DCS}{DCS_0}\right)^{0.1}\left[\frac{U\Delta\hat{\sigma}}{S_{ut}}\right]^{\zeta} a + C_1\left(\frac{\Delta\gamma^P{}_{\max}}{2}\bigg|_{macro}\right)^2 \qquad (3)$$

where C_1, C_{II} and ζ are material parameters to be determined based on fatigue-rack growth experiments in the MSC regime. The equivalent stress is defined as a linear combination of the von Mises stress and the maximum stress,

$\Delta\hat{\sigma} = \theta_1\left[\frac{3}{2}\frac{\sigma'_{ij}}{2}\frac{\sigma'_{ij}}{2}\right]^{0.5} + \theta_2\Delta\sigma_1$, with θ_1 and θ_2 as load-path-dependent and combined stress state-dependent parameters. Similar to MSF for A356 Al alloy, $\zeta = 4.2$ was found suitable for Mg alloy. Here, two porosity related functions are considered: (1) the variation of average porosity in the specimens: $f(\bar{\phi}) = 1 + \omega\left\{1 - \exp\left(-\frac{\bar{\phi}}{2\phi_{th}}\right)\right\}$, and the porosity threshold (considered as 0.0001); (2) the porosity in front of the microstructurally small crack that reduces the load- bearing capacity of the matrix,

$g(\phi) = (1-\phi)^{-\lambda}$ and $0 < \lambda < 1$.

The MSF model correlations were based on the crack-like damage initiating at casting pores of 25 microns in diameter. The endurance limit for AZ91D was determined as 55 MPa, which is one-third of the cyclic yield strength.

MSF Model Correlations for an AZ91 Cast Mg Alloy

Two types of specimens were prepared: as-cast and cut from a cast automotive component. The general static and fatigue strain-life, stress-life, and cyclic hardening properties were obtained by Westmoreland Testing and Research. Figure 2 shows strain versus fatigue life under R=-1 strain-controlled, constant-amplitude tests at room temperature and in lab air. Multistage fatigue models were correlated based on the static, cyclic and strain-life test results.

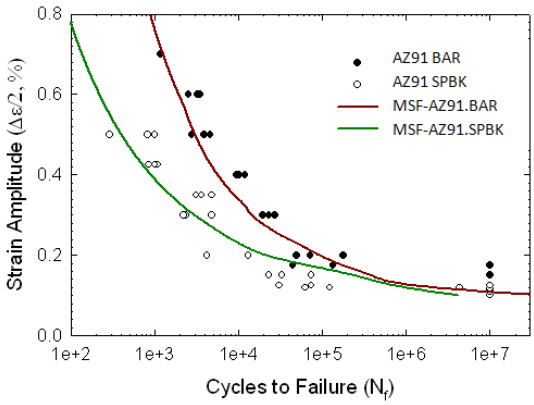

Figure 2. Strain-life test and calculated results on cast bars (BAR) and machined from a support bracket (SPBK) under R=-1 strain control at room temperature and lab air.

Evaluation of an AZ31 Extruded Mg Alloy

Extruded Mg AZ31 alloy was provided in an extruded engineering piece shown in Figure 3. Surfaces representing various features in the extrusion pieces were cut and polished/etched to reveal the extrusion metallurgical features. After mechanical polishing, the inclusion particles were first examined using an optical microscope. Figure 4 shows the optical micrographs of typical surfaces perpendicular to the extrusion direction and to the normal direction. Digitized-image analysis will be implemented to quantify the variations in inclusion-particle distributions and distinguish the variations among different

surfaces. Then, the surface will be etched using an acetic-picral solution. The grain structure and morphology will be revealed in the optical micrographs.

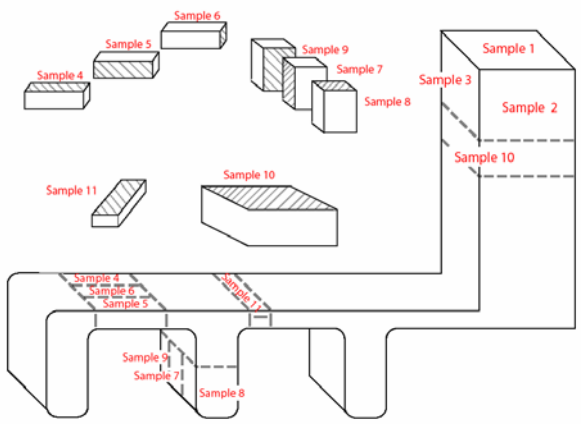

Figure 3. Sketch of extruded AZ31 Mg alloy and surfaces prepared to evaluate various extrusion-specific microstructural features.

Static Tensile Properties of an AZ31 Extruded Mg Alloy

Quasi-static, uniaxial tensile tests were performed at the strain rate of 10^{-3}/s on the specimens along the extrusion and transverse directions. Figure 5 shows the true stress-strain curves of the AZ31 Mg alloy along extrusion direction at room temperature and 100°C and along the transverse direction at room temperatures, respectively. Strong anisotropic yield strength and hardening behavior are demonstrated for the extruded AZ31 Mg alloy.

FASTRAN and Small-Crack Theory

For a number of engineered materials, the fatigue process has been shown to be dominated by "crack propagation" from metallurgical features or discontinuities such as voids, inclusion-particle clusters and grain-boundary locations. These materials were 2024 and 7075 (bare and clad) Al alloys, 2090 Al-lithium alloy, 4340 steel and titanium (Ti)-6Al-4 vanadium (V) titanium engine disc forgings [6-8]. Thus, the fatigue life is primarily composed of the cyclic life for microstructurally and physically small cracks and large-crack behavior. For these materials, observations of the fatigue process indicated that microcracks are present when the material is processed or they crack very early from microscale plasticity at local discontinuities.

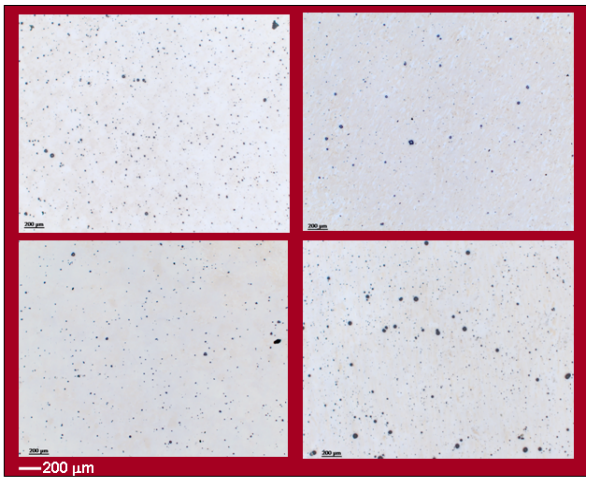

Figure 4. The optical micrographs of typical surfaces of extruded AZ31 Mg alloy. LD, TD, and ND are the extrusion, transverse, and normal direction of the processing coordinate, respectively. LD_TD and TD_ND are the planes formed by the two directions, respectively.

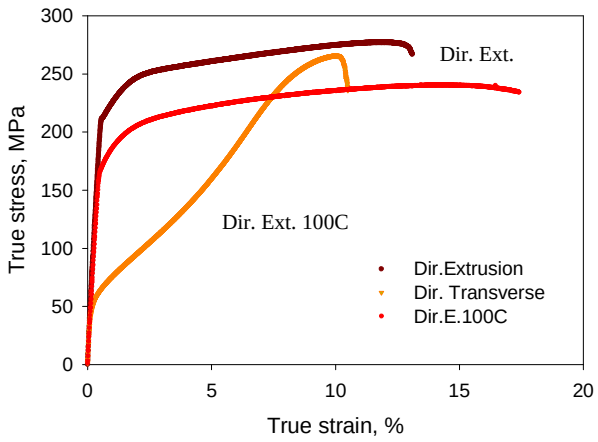

Figure 5. Stress-strain curve of AZ31 Mg alloy under uniaxial tension at room temperature and 100°C along extrusion and transverse directions.

For the 2024 and 7075 alloys, the initial flaw sizes have ranged from 6 to 20 µm [6 and 8]. The 4340 steels have exhibited 8 to 30 µm flaws from calcium-aluminate and manganese-sulfide particles [9]. Initial flaw sizes in the Al alloys and steels were determined by measuring the inclusion particle sizes that precipitated fatigue failures. The Ti alloy forgings had 2 to 20 µm flaws, but these were determined by an equivalent-initial-flaw-size

(EIFS) procedure. In the EIFS procedure, nonlinear fracture mechanics and fatigue-crack growth-rate (small and large crack) properties were used to determine the particular flaw size to fit the stress (S) versus number of cycles-to-failure (N) S-N behavior.

Small-Crack Theory, which assumes an initial flaw size from 1 to 30 μm for various materials, has been used with the fatigue-rack growth-rate properties and a crack-closure model [10] to predict or calculate the S-N curves under both constant and variable amplitude loading. In the Small-Crack Theory approach, no distinction is made between microstructurally- and physically-small cracks. They are both considered "small" cracks and the influences of microstructure are in the measured crack growth-rate data. Small-crack growth behavior is achieved by continuum-mechanics analyses using monotonic and cyclic plasticity and the crack-closure transients under the prescribed load histories.

One of the objectives of the current project is to determine whether Mg alloys have similar initial flaw sizes in their microstructure that precipitate fatigue failure from crack propagation alone. In an effort to address the feasibility of using Small-Crack Theory to calculate fatigue lives on a Mg alloy, fatigue strain, ε, versus N data were recently obtained at MSST for AZ91D (B. Jordon, MSST, private communication, 2007).

Fatigue-Crack Growth

Fatigue-crack growth-rate (dc/dN, change in crack length, c, with change in cycles, N) data on a AZ91E Mg alloy have been obtained from Dr. Andy Newman, U.S. Army at NASA Langley Research Center. These data were determined from compact tension specimens under two stress ratios ($R = P_{min}/P_{max}$ = 0.1 and 0.7), and these data are shown as symbols in Figure 6. The crack-growth-rate data were measured from threshold to near fracture and the fracture toughness was estimated to be about 15 ksi-in$^{1/2}$. Cracks in the high stress-ratio tests have fully-open cracks (no crack-closure). Thus, these data are used to establish the effective stress-intensity factor against rate (ΔK_{eff}-rate) baseline curve for the material and test conditions (room temperature and lab air). (The ΔK_{eff}-rate baseline curve is used in the FASTRAN model [10] to predict small- and large-crack growth under constant and variable amplitude loading.) Because the high-R tests fracture at lower values of ΔK than low-R tests, i.e., $\Delta K_c = K_c (1-R)$, the low-R test results are also used to estimate the ΔK_{eff}-rate curve at high rates.

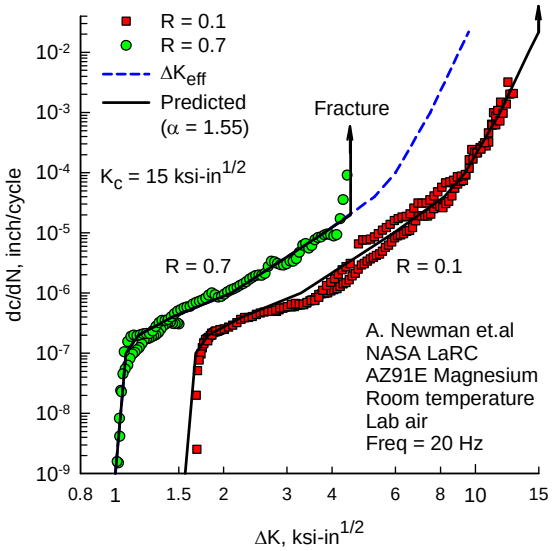

Figure 6. Fatigue-crack growth-rate data on AZ91E Mg alloy.

For high rates, an iterative procedure is used because the curves are a function of the crack-front constraint factor, α. For these data, α was found to be 1.55, which is lower than expected. Increased crack-closure effects due to crack-surface roughness may have caused the lower value. The solid (black) curves are the predicted curves from the FASTRAN model.

Strain-Life Tests on Mg Alloy

Fatigue data were obtained from Jordon at MSST for the Mg alloy AZ91D. Fatigue test (ε-N) data generated on K_T = 1 bar specimens under fully-reversed loading are shown in Figure 7 (diamond symbols). The data from Figure 2 are also included for comparison. Jordon's data also included the full-strain- and load-against-cyclic history on eight specimens. The bar specimens were 0.12 inches thick by 0.25 inches wide and tested at three strain levels (0.002, 0.003 and 0.0035). These data fell in between the fatigue data shown in Figure 2.

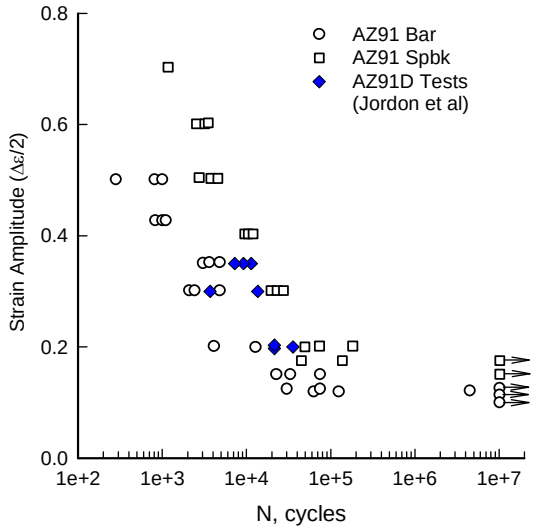

Figure 7. Strain against cycles-to-failure on AZ91 Mg alloys.

The cyclic strain and load histories were available on all LCF specimens (LCF-3 to 10) as shown in Figure 9. A rapid (vertical) drop off of stresses indicated failure of the specimens as illustrated in Figure 8. Based on the measurements, the applied strains were very accurately maintained during the duration of the tests. Figure 8 shows the applied stress (maximum and minimum) for test specimen LCF-3. The maximum applied stress was nearly constant (S_{max} ~ 20.5 ksi) during the duration of the test, but showed a slight reduction near the end of life due to cracking. But the minimum applied stress showed more variation (–18 to –22 ksi). The reason for this behavior was unknown but could be related to the tensile and compressive stress-strain curves being different (as shown in Figure 5), cyclic strain hardening, or variations in the stress-strain response from different sections of the Mg material.

Fatigue-Life Calculations on Mg Alloy

The FASTRAN life-prediction code was used to calculate the fatigue lives on the AZ91D alloy specimens using crack propagation from an EIFS. The effective stress-intensity factor against crack-growth- rate curve had previously been obtained on an AZ91E alloy from NASA Langley. The significance of the Mg alloy treatment, D or E, could not be addressed.

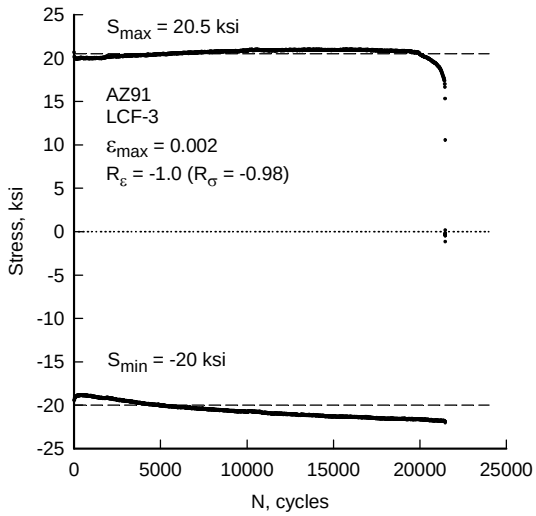

Figure 8. Applied stress against cycles for LCF-3.

Since the FASTRAN code is based on the "applied stress" instead of applied strain, either an average stress history or the variations in both minimum and maximum stresses would have to be considered in the fatigue-life analyses. For simplicity, an average stress history (S_{max}, S_{min}) was selected for each specimen and these values were used in the fatigue-life analyses. Some typical results are shown in Figure 8, which shows the maximum and minimum stresses applied to LCF-3 as a function of cycles. This test had a stress ratio R_σ (S_{min}/S_{max}) of –0.98. The rapid (vertical) drop off of stress indicated failure of the specimen at 21,500 cycles. While the cyclic strains were very accurately maintained during the duration of the test, the stresses showed some variations. The range of stress ratios from the eight tests was from –0.98 to –0.42.

The maximum applied stress against cyclic life (S-N) for the AZ91 alloy is shown in Figure 9. As noted, the applied stress ratio (R_σ) varied. Thus, calculations have been made at –1 and –0.4. A trial-and-error procedure was used to find the EIFS to fit the test data. The EIFS was found to be a 0.012-inch (305-μm) semi-circular surface flaw. The R = –1 curve agrees well with five of the eight specimens. The R = –0.4 curve agrees well with specimen LCF-5, which had an applied stress ratio of –0.42. But, the results for test specimens LCF-3 and 4 showed that the calculated curves were very conservative.

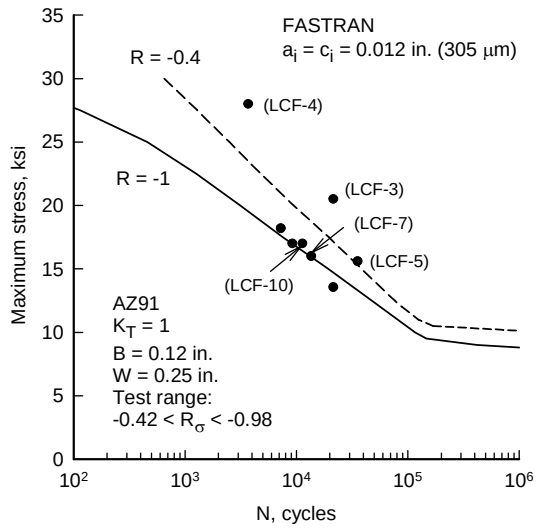

Figure 9. Stress against cycles-to-failure on AZ91 Mg alloy.

A typical fatigue surface from the AZ91 alloy is shown in Figure 10. The initiation site appeared to be a large void (620-μm deep by 250-μm wide) located near the edge of the specimen. Using Murakami's area rule, a 280-μm semi-circular surface crack would have the same area. Thus, the assumed 305-μm radius surface flaw was very close to the void area.

Most of the calculations fell within ± 30%, but calculations made on specimens LCF-3 and 4 were very conservative (factor-of-10) and the calculation on specimen LCF-6 was un-conservative by over a factor-of-2. A determination of the distribution of void sizes in the AZ91 alloy would be useful. Specimens LCF-3 and 4 could have had smaller voids that precipitated failure due to the very small specimen tested. FASTRAN could be used with the distribution of voids to make an upper and lower bound estimate for the fatigue scatter.

The MSF and FASTRAN calculations represented the AZ91 Mg alloy very well, in that the fatigue lives on six of eight tests were accurately calculated. However, these tests were basically LCF results. Whether Small-Crack Theory will work well on the Mg alloys for HCF is yet to be studied. In the past, the fatigue-crack-growth thresholds and the initial flaw sizes have correlated very well with the endurance limits on the materials previously studied with Small-Crack Theory. Thus, Small-Crack Theory has worked well for HCF conditions on Al alloys, Ti alloys and steels. The key for any physics-based model is to observe the fatigue process very early in life to assess the state of damage or cracking.

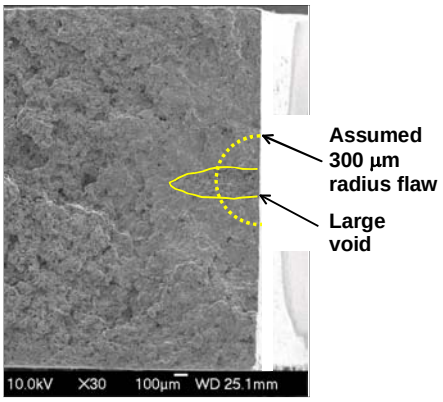

Figure 10. Initiation site at large void and assumed EIFS in AZ91 alloy.

Conclusions

Preliminary studies on the AZ91 alloy have been used to exercise the two fatigue models: (1) the MSF model and (2) Small-Crack Theory using a crack-closure model. The initial evaluations were made under fully-reversed fatigue-loading conditions. The MSF model accounted for the influence of the manufacturing process on the strain-life behavior. The Small-Crack Theory model used fatigue crack growth properties and a 300-μm semicircular flaw to calculate the fatigue lives under the strain-controlled loading conditions.

Two AZ31D Mg extrusions from the automotive industry are being machined into a wide range of tensile and fatigue specimens to generate the mechanical properties for calibration of the two fatigue models.

Presentations/Publications/Patents

Xue, Y., Lugocamarena, M., Horstemeyer, M.F. and Newman, J.C., Jr., "Multistage Fatigue Model for an Extruded AZ31 Mg Alloy," TMS 2008 (accepted for presentation).

References

1. McDowell, D.L., Gall, K., Horstemeyer, M.F. and Fan, J., "Microstructure-based fatigue modeling of cast A356-T6 alloy," Engineering Fracture Mechanics, 70 (2003), 49-80.Suresh, S., Fatigue of Materials, 2nd Edition, Cambridge University Press, p. 543, 2003.
2. Xue, Y., Horstemeyer, M.F., McDowell, D.L., El Kadiri, H. and Fan, J., Microstructure-based multistage fatigue modeling of cast AE44 Mg alloys, *International Journal of Fatigue* 2007; 29:666-76.
3. Horstemeyer, M.F., Fan, J., and McDowell, D.L., "From Atoms to Autos: Part 2 Fatigue Modeling," Sandia National Laboratories Report, SAND2001-8661.
4. Xue, Y., Burton, C.L., Horstemeyer, M.F. and McDowell, D.L., Multistage Fatigue Modeling of Cast A356-T6 and A380-F Aluminum Alloys, *Metallurgical & Materials*, Trans. B (in press).
5. Newman, J.C., Jr. and Edwards, P.R., Short-Crack Growth Behaviour in an Aluminum Alloy - an AGARD Cooperative Test Programme, AGARD R-732, 1988.
6. Short-Crack Growth Behaviour in Various Aircraft Materials, AGARD R-767, P.R. Edwards and J.C. Newman, Jr., editors, 1990.
7. Newman, J.C., Jr., Wu, X., Venneri, S. and Li, C., "Small-Crack Effects in High-Strength Aluminum Alloys," NASA RP-1309, May 1994.
8. Swain, M.H., Everett, R.A., Jr., Newman, J.C., Jr. and Phillips, E., "The Growth of Short Cracks in 4340 Steel and Aluminum-Lithium 2090," AGARD R-767, 1990, pp. 7.1-7.30.
9. Newman, J.C., Jr., "A Crack-Closure Model for Predicting Fatigue Crack Growth Under Aircraft Spectrum Loading," ASTM STP-748, 1981, pp. 53-84.

I. Materials Design for Magnesium Alloys

Seong-Gon Kim: Co-Principal Investigator
Assistant Professor
Physics and Astronomy
Hilbun Hall, Rm 237
Mississippi State University (MSST), P.O. Box 5405
Mississippi State, MS 39762-5405
(662) 325-8031; fax: (662) 325-8898; e-mail: kimsg@ccs.msstate.edu

Mark F. Horstemeyer: Principal Investigator
Center for Advanced Vehicular Systems (CAVS) Chair in Solid Mechanics & Professor, Mechanical Engineering
MSST
206 Carpenter Bldg., PO Box ME
Mississippi State, MS 39762
(662) 325-7308; fax: (662) 325-7223; e-mail: mfhorst@me.msstate.edu

Randall German: Co-Principal Investigator
Professor and Director CAVS
MSST, P.O. Box 5405
Mississippi State, MS 39762-5405
(662) 325-5431; fax: (662) 325-5433; e-mail: german@cavs.msstate.edu

Hongjoo Rhee: *Co-Principal Investigator*
Postdoctoral Associate
CAVS
MSST, P.O. Box 5405
Mississippi State, MS 39762-5405
(662) 325-9221; fax: (662) 325-5433; e-mail: hrhee@cavs.msstate.edu

Sungho Kim: Postdoctoral Associate
CAVS, CAVS 2182-C
MSST
Mississippi State, MS 39762-5405
(662) 325-9241; fax: (662) 325-5433; e-mail: sk5@msstate.edu

Greg Olson: Co-Principal Investigator
Winson-Cook Chaired Professor in Engineering Design
The Steel Research Group at Northwestern
Northwestern University
Department of Mechanical Engineering
2145 Sheridan Road
Evanston, Illinois 60208-3111
(847) 491-2847; fax: (847) 491-7820; e-mail: g-olson@northwestern.edu

Qingyou Han: Co-Principal Investigator
Purdue University
Mechanical Engineering Technology Department
401 North Grant Street
Knoy Hall - Room 107
West Lafayette, IN 47907-2021
(765) 494-7528; fax: (765) 494-6219; e-mail: hanq@purdue.edu

Joseph A. Carpenter: Technology Area Development Manager
(202) 586-1022; fax: (202) 586-1600; e-mail: joseph.carpenter@ee.doe.gov

Expert Technical Monitor: Philip S. Sklad
(865) 574-5069; fax: (865) 574-6098; e-mail: skladps@ornl.gov

Contractor: MSST
Contract No.: 4000054701

Objective

- Design low-cost magnesium (Mg) alloys with improved castability, ductility, and high-temperature creep-deformation mechanisms for automotive applications.

Approach

- In support of the collaborative materials-design effort proposed here aimed at lightweight components for automotive applications, a systems approach to materials design [Olson98] will be applied. Working within a multiscale hierarchy of microstructural subsystems governing desired property combinations for structural performance, key microstructural elements will be identified for the calibration, application, and validation of process/structure and structure/property design models defining key theoretical parameters and critical experiments enabling parametric design of novel alloy compositions.

- We will use quantum mechanical, first-principles methods such as Density Functional Theory (DFT) [Kresse96, Kohn65] to elucidate the origin of the alloying effects. A fundamental understanding of solidification, dislocation, creep, fatigue, crack nucleation and failure of Mg-based alloy systems also requires accurate atomistic modeling of nanoscale systems containing up to hundreds of thousand atoms. We will perform large- scale atomistic simulations using efficient and reliable empirical interatomic potential methods such as the modified embedded-atom method (MEAM) [Baskes92, Daw84, Daw83] and force-matching-embedded-atom-method (FMEAM) potentials.

- Various state-of-the-art experimental techniques will also be employed in this project. Scanning electron microscopy (SEM) and transmission electron microscopy (TEM) will be used to obtain microscale as well as nanoscale structural information of Mg alloys. The structure and energies of dislocation cores and planar defects, including stacking faults and twin boundaries, determine the mechanical behavior of the Mg alloys. Electron backscatter diffraction (EBSD) and X-ray diffraction (XRD) measurements will be used to keep track of texture evolution during deformation. An *in-situ* chemical analysis and mapping of alloying elements can be used to keep track of these elements. Three-dimensional atom probe (3DAP) is capable of resolving the chemical identity and position of individual atoms in 3D with atomic resolution in the z-direction and sub-nanometer resolution in the lateral direction. Furthermore, fundamental thermo-mechanical experiments to measure creep resistance and ductility will be carried out under various loading conditions. Experimental failure analysis will be performed to understand the microstructure-driven mechanism of plasticity and damage growth under monotonic and cyclic loadings. X-ray computed tomography (CT) will be used to quantify in three-dimensions, morphological and topological evolutions of voids and relevant microstructural features to material damage. A depth-sensoring microindenter and a nanoindenter will also be used to evaluate the micromechanical properties of each microstructural phase present in the Mg alloys. These measurements will be used to validate and, in turn, guide the computational material design of new Mg alloys.

- Construct and validate reliable interatomic potentials to model various phases of Mg-based alloys.
- Obtain the electronic, structural and mechanical properties of the Mg alloys.
- Investigate the effect of various additives on the thermo-mechanical properties of Mg alloys;

- Develop rigorous models for investigating the effect of various fabrication processes on the thermo-mechanical properties of the Mg alloys;
- Perform experiments to validate new design models.

Accomplishments

The first-year objectives were met by accomplishing the following:

- Mg alloys AM50B, AM60B, and AE44 have been cast at ORNL by Qingyou Han (now at Purdue) as the base alloys for the project.
- The nanostructure of an experimental, low-melting-point Mg- 7 zinc (Zn) - 3Al prototype alloy was characterized by 3D atom-probe microanalysis in a local-electrode atom probe (LEAP) after aging at 150^{o}C for 100 hours (hrs) to peak hardness corresponding to a yield strength of 190 MPa. The strengthening phase composition was consistent with the ternary Phi phase, including metastable compositions. The equivalent sphere diameter of the precipitates at peak strengthening is measured as 20-50 nm, providing an important strength- model calibration for materials design. The experimental results are available as a preprint:

  Shengjun Zhang and Gregory B. Olson, 3D-atom probe investigation of strengthening precipitates in a Mg-7Zn-3Al alloy, preprint.
- The MEAM potentials for Mg-Al alloys have been developed. We improved upon the potentials previously published [Baskes92, Lee03] to achieve better agreement with experiments and first-principles method based on quantum mechanical, density functional theory (DFT). The potential parameters and validation data have been published in:

  B. Jelinek, J. Houze, Sungho Kim, M. F. Horstemeyer, M. I. Baskes, Seong-Gon Kim, "Modified embedded-atom method interatomic potentials for the Mg-Al alloy system", Phys. Rev. B, vol. 75, pp. 054106 (2007).
- A multi-objective optimization methodology to construct empirical interatomic potentials with minimal manual fitting has been developed and applied to construct a new MEAM interatomic potential for Mg. This new methodology is designed to optimally reproduce multiple target values that consist of several essential materials properties obtained from experiments and first-principles calculations based on DFT. The optimized target quantities include elastic constants, cohesive energies, surface energies, vacancy formation energies, and the forces on atoms in a variety of structures. The new procedure has been applied successfully to develop a new MEAM potential for Mg. The accuracy of the new potential is assessed by computing several material properties of Mg and comparing them with those obtained from other potentials previously published. We found that the present MEAM potential yields a significantly better overall agreement with DFT calculations and experiments. The new methodology and its application to Mg potential along with its validation data have been submitted to a peer-reviewed journal for publication:

  J. Houze, Sungho Kim, Amitava Moitra, B. Jelinek, Sebastien Groh, M. F. Horstemeyer, Erdem Acar, Masoud Rais-Rohani, Seong-Gon Kim, "A multi-objective optimization procedure to develop modified-embedded-atom-method potentials: an application to magnesium", submitted to Phys. Rev. B, http://arxiv.org/abs/0708.0075

Future Direction

- Develop new MEAM potentials for Mg – oxygen (O) and Al-O alloy systems to study the effect of oxygen in Mg-Al-based alloys.
- Validate Mg-O and Al-O MEAM potentials with DFT calculations.
- Perform large-scale molecular dynamics simulations to study the effect of additive elements on material properties of Mg-based alloys.
- Carry out microstructure and mechanical properties characterization of the base-alloys (AM50B, AM60B, and AE44) to understand fundamental materials and mechanical properties.
- Available thermodynamic databases and literature on precipitation-strengthening phases will be reviewed in support of theoretical feasibility assessment of microstructural strategies for castable alloys with creep resistance at 150 ^{o}C. Candidate alloy systems will be identified for further 3D atom-probe microanalytical studies.

Introduction

Mg alloys are currently used in relatively small quantities for automotive components, generally limited to die castings. Two main barriers to wider impact of Mg alloys to automotive industry are poor creep resistance at temperatures above 150 °C for powertrain applications and poor ductility for structural body parts, engine components, engine cradle and control arms.

To achieve the goal of improving the fuel efficiency of the cars built in the future, the automobile industry needs to have Mg-alloy, light-weight, high-strength materials with better materials properties. We need to perform compositional design of Mg-based alloys in a manner that increases creep resistance and ductility while keeping production cost low.

The future state of this technology will be the development of Mg-based alloys that have lower mass densities and increased strength compared to Al-based alloys, and have better creep resistance than that of AE44-grade Mg alloy and cost comparable to that of AZ19D-grade Mg alloy. The new Mg-based alloys should also exhibit sufficiently high ductility to allow conventional fabrication processes to be used, but generate adequate strength after the fabrication process.

Approach

In support of the collaborative materials design effort proposed here aimed at lightweight components for automotive applications, a systems approach to materials design [Olson98] will be applied. Working within a multiscale hierarchy of microstructural subsystems governing desired property combinations for structural performance, key microstructural elements will be identified for the calibration, application, and validation of process/structure and structure/property design models defining key theoretical parameters and critical experiments enabling parametric design of novel alloy compositions.

Figure 1 shows an overall flowchart of the project procedure along with proper technical approaches. First, reliable, empirical interatomic potentials to model various phases of Mg-based alloys are constructed and validated. Next, the structural, electronic, and mechanical properties of the main phases of Mg-based alloys are obtained by DFT and atomistic simulations. In order to design a novel Mg-based alloy with improved castability and ductility, the effects of various phases, novel additives, and precipitates on the materials and mechanical properties of the Mg-based alloys are investigated by DFT and atomistic simulations. At this stage, various base alloys of interest with

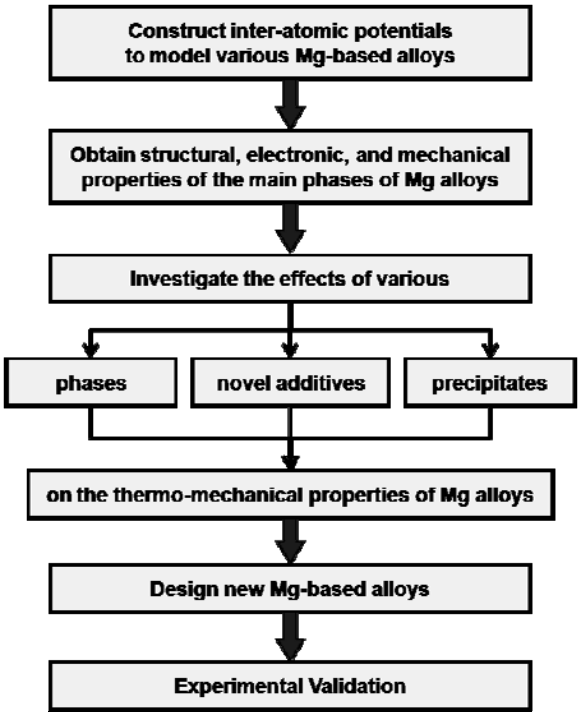

Figure 1. Overall flowchart of the project procedure along with proper technical approaches.

different intrinsic materials properties will be provided by collaborators at ORNL. Various experiments on the base alloys will be carried out to understand fundamental materials/mechanical properties and the output will be provided for materials-designing efforts. Such experiments include chemical analysis, microstructure observation, and micro- and macro-mechanical tests.

Computational Approach

We use a hierarchical, multiscale methodology to investigate the effect of nanoscale precipitates and additives to the overall strength and ductility in Mg-based alloy design for automotive applications. In a hierarchical multiscale framework, numerical methods are run independently at dispa-

rate length scales. Then, a bridging methodology such as statistical analysis methods, homogenization techniques, or optimization methods are used to distinguish the pertinent cause-effect relations at the lower scale to determine the relevant effects for the next higher scale [E03]. One effective hierarchical method for multiscale bridging is the use of thermodynamically-constrained internal state variables (ISVs) that are physically based on microstructure-property relations [Coleman67, Rice71, Kestin70, Hasan95, Espinosa01, Gailly02]. We will adopt the strategy developed by Horstemeyer and his co-workers who used ISVs as a top-down hierarchical approach to bring the pertinent nanoscale, microscale, and mesoscale phenomena into the macroscale [Horst01, Horst03, Olson98, Olson00, Hao03, Hao04].

At the electronic level, quantum-mechanical, first-principles simulations are performed to investigate the interfacial interactions between matrix and the primary and the secondary precipitates. All first-principles, total-energy calculations and geometry optimizations are performed within the DFT [Kresse96, Kohn65] using Blöchl's all-electron projector augmented wave (PAW) method [Blochl94] as implemented by Kresse et al. [Kresse99]. For the treatment of electron exchange and correlation, we generally use the local-density approximation (LDA) [Ceperley80, Perdew81] and sometimes the generalized gradient approximation (GGA) [Perdew96] depending on the accuracy required. The Kohn-Sham equations are solved using a preconditioned band-by-band conjugate-gradient (CG) minimization [Kresse93].

At the atomistic level, accurate atomistic simulations will be performed using efficient and reliable empirical interatomic potentials such as the MEAM or FMEAM [Li03, Liu96] potentials. The interatomic potentials are constructed by optimizing the potential parameters to reproduce various experimental materials properties and atomic force data from DFT calculations. Large-scale atomistic simulations will be conducted to study the effect that size, shape, and volume fraction of different precipitates have on the thermo-mechanical properties of Mg-based alloys. Many factors that govern the yield and hardening behavior of solids, such as crack-tip propagation, dislocation nucleation, dislocation motion, and the interaction of dislocations with grain boundaries, will be investigated through these simulations. Results will be used to guide quantitative alloy composition designs to improve castability and creep resistance of Mg alloys.

Experimental Approach

Various state-of-the-art experimental techniques will be employed in this project. The overall chemical analysis of the base-alloys of interest will be performed by using a spectrometer. Microstructures of the alloys will be investigated by an optical microscope (OM) and a SEM. SEM and TEM will be used to obtain microscale as well as nanoscale structural information of Mg alloys. The structure and energies of dislocation cores and planar defects, including stacking faults and twin boundaries, determine the mechanical behavior of Mg alloys. EBSD and XRD measurements will be used to keep track of texture evolution during deformation. The quantitative as well as qualitative chemical compositions of each phase present in the alloys will be individually analyzed by an energy-dispersive x-ray (EDX) spectroscopy technique. An *in-situ* chemical analysis and mapping of alloying elements can be used to keep track of these elements. 3DAP is capable of resolving the chemical identity and position of individual atoms in 3D with atomic resolution in the z-direction and sub-nanometer resolution in the lateral direction. Conventional hardness tests will be conducted to gain overall properties of the alloys, while depth-sensoring microindentation and nanoindentation tests (NITs) will be performed to obtain micro-mechanical properties of each microstructural phase present in Mg alloys. These measurements will be used to validate and, in turn, guide the computational material design of new Mg alloys. Furthermore, fundamental thermo-mechanical experiments to evaluate creep resistance and ductility will be carried out under various conditions. In order to obtain fundamental mechanical properties and attain proper stress levels for creep tests, tensile tests will be carried out at elevated and room temperatures. The creep behaviors of the base alloys will be extensively investigated to determine better ways for developing novel Mg alloys with improved creep resistance. The creep specimens will be machined from the as-cast condition and the density of the samples will be measured prior to and after the creep tests.

An X-ray computed tomography (CT) will be used before and after the creep tests to quantify the 3D morphological and topological evolutions of voids and microstructural features relevant to material damage. Experimental failure analysis will be performed to understand the microstructure-driven mechanism of plasticity and damage growth under monotonic and cyclic loadings.

By utilizing the composition-structure-property relationship extracted by aforementioned experiments and various simulations, a novel Mg alloy with improved creep resistance and ductility will be designed. A small amount of sample will then be manufactured and supplied by the industrial partners and the model validation by various experiments, including creep tests, will be carried out.

Empirical Interatomic Potentials

To meet the industrial demand for high-strength, lightweight Mg alloys, it is essential to obtain detailed understanding of the effect of individual alloying elements on the properties of Mg alloys. The alloying elements can form interstitial or substitutional defects, or can precipitate into small particles creating complex interface structures. The interactions between these alloying elements need to be investigated using atomistic simulation techniques such as molecular dynamics (MD) or Monte Carlo simulations. These atomistic simulations require accurate atomic interaction potentials to compute the total energy of the system. First-principles calculations certainly can provide the most reliable interatomic potentials. However, realistic simulations of alloy systems often require a number of atoms that renders these methods impractical – they either require too much computer memory or take too long to be completed in a reasonable amount of time. One alternative is to use empirical interatomic potentials that can be evaluated efficiently, so that the atomistic approaches that use them can, in certain cases, handle systems with more than a million atoms.

There are two additional essential features that are expected from a useful empirical approach besides its efficiency: reliability and flexibility. A reliable interatomic potential would accurately reproduce various fundamental physical properties of the relevant element or alloy, such as elastic, structural, and thermal properties. Reliability also includes transferability. A transferable interatomic potential would perform reasonably well even under circumstances that were not used during its construction phase. A flexible empirical approach can represent interaction potentials among a wide variety of elements and their alloys using a common mathematical formalism.

Within the embedded-atom method (EAM) [Daw84, Daw83] approach, the total energy of the system can be written as

$$E = \sum_i E_i \tag{1}$$

where

$$E_i = \frac{1}{2}\sum_{j(\neq i)} V(r_{ij}) + F(n_i) \tag{2}$$

$V(r)$ is the pair interatomic potential, $F(n)$ is the embedding energy function, n_i is the total 'atomic density' at atom i from the surrounding atoms, and it is assumed that

$$n_i = \sum_{j(\neq i)} \rho(r_{ij}) \tag{3}$$

where $\rho(r)$ is the 'atomic density' around an isolated atom, and *r* is the interatomic distance [Daw84]. The EAM was able to reproduce physical properties of many metals and impurities. The EAM was applied to hydrogen embrittlement in nickel [Daw83], and to nickel and palladium with hydrogen [Daw84].

Baskes *et al.* [Baskes87] proposed the MEAM, which is an extension of EAM to include angular forces. The MEAM potential proposed was the first empirical interatomic potential method to use a single formalism for face-centered cubic (fcc), body-centered cubic (bcc), hexagonal close-packed (hcp), diamond-structured materials and even gaseous elements, in good agreement with experiments or first-principles calculations [Baskes87, Baskes89, Baskes92, Baskes94]. Cherne *et al.* made a careful comparison of MEAM and EAM calculations in a liquid nickel system [Cherne01].

In the FMEAM, a force-matching method [Ercolessi94] is applied to the conventional EAM. Unlike the MEAM, however, the FMEAM approach does not use any analytic functional form for $\rho(r)$, $V(r)$, or $F(n)$. Instead, each of these functions is described as a set of control points whose values are the parameters to be optimized. A cubic spline function is used to interpolate the values between the control points. The control points are optimized by matching the forces of this potential to those of quantum mechanical, *ab initio* calculations for a large set of different configurations. The potential parameters are simultaneously fit to several critical experimental data such as equilibrium lattice constant, cohesive energy, bulk modulus, and elastic constants.

Multi-objective Optimization

A generic, multi-objective optimization (MOO) problem can be formulated as [Kim05, deWeck04]:

$$\begin{aligned} &\min\ \vec{J}(\vec{x}) \text{ s.t. } x \in S \\ &\text{where } \vec{J} = \left[J_1(\vec{x}) \cdots J_m(\vec{x})\right]^T \\ &\vec{x} = \left[x_1 \cdots x_n\right]^T \end{aligned} \tag{4}$$

Here, $\vec{J}$ is a column vector of *m* objectives, whereby $J_i \in \Re$ (a real number). The individual objectives are dependent on a vector $\vec{x}$ of *n* design variables in the feasible domain *S*. The design variables are assumed to be continuous and vary independently. Typically, the feasible-design domain is defined by the design constraints and the bounds on the design variables. The problem is to minimize all elements of the objective vector simultaneously. The most widely used method for MOO is scalarization using the weighted-sum method. The method transforms the multiple objectives into an aggregated scalar objective function $\vec{J}$ that is the sum of each objective function J_i multiplied by a positive weighting factor w_i:

$$J(\vec{x}) = \sum_{i=1}^{m} w_i J_i(\vec{x}) \tag{5}$$

In this project, the overall goal is to develop FMEAM potentials for Mg-based alloys. The individual objective functions are constructed from the normalized differences between the FMEAM-generated values and the target values:

$$J_i(\vec{x}) = \left[\frac{Q_i(x) - Q_i^0}{Q_i^*}\right]^2 \tag{6}$$

Here, Q_i is the physical quantity computed using the current FMEAM-potential parameters and Q_i^0 is the target value to reproduce. The target values are usually experimental values, but the computed values from the first-principles method are chosen when the experimental data are not available. The normalization factor Q_i^* is a typical value for the given materials parameter and often $Q_i^* = Q_i^0$ is assumed. The overall objective function $J(\vec{x})$ can be minimized using usual multi-dimensional optimization routines. To avoid unnecessary complications, we use the *downhill simplex method* [Press92], which requires only function evaluations, not derivatives.

Mg Interatomic Potential

The MOO procedure was applied to develop a new interatomic potential for Mg based on MEAM. We used the previously published MEAM potential by Baskes [Baskes92] as the initial set of the parameters for our MOO.

Figure 2 shows the cohesive energy of Mg atoms in the hcp structure, its lowest-energy crystal structure, as a function of the lattice constant. MEAM-potential calculations (open circles) are compared with the Rose equation-of-state (solid curve). The Rose equation-of-state is constructed from experimental data—optimum lattice constant, the cohesive energy, and the bulk modulus. Our results show that MEAM potential for Mg reproduces experimental data extremely accurately over a wide range of lattice constants.

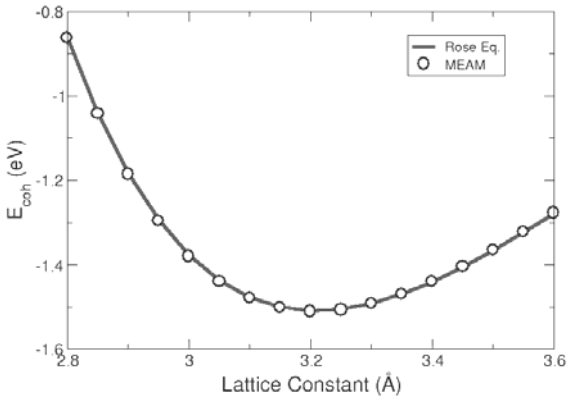

Figure 2. The cohesive energy of Mg atoms in the hcp cubic crystal structures as a function of the lattice constant *a* (open circles), compared with the Rose equation (solid curve).

To validate the transferability of our new MEAM potential, we calculated the cohesive energies of Mg atoms in three common configurations, namely, hcp, fcc, and bcc crystal structures, as a function of the atomic volume. The results are summarized in Figure 3. Our results show that the new MEAM potential for Mg atoms correctly predicts the order of stability among these common structures. In addition, the differences in equilibrium cohesive energies among these configurations are reasonably close to those of DFT calculations.

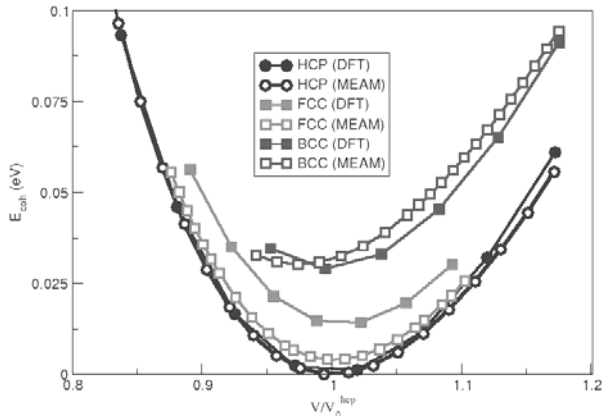

Figure 3. The cohesive energies of Mg atoms in hcp, fcc, and bcc crystal structures as a function of the atomic volume. The values reproduced with MEAM potentials are compared with DFT calculations. Volumes are scaled by the equilibrium atomic volume of the hcp structure.

Semi-infinite surface is one of the simplest forms of defects. To test the transferability of Mg MEAM potential, surface-formation energies for several different surfaces are computed. Surface-formation energy per unit surface area, E_{surf}, is defined as

$$E_{surf} = (E_{tot} - N\varepsilon)/A, \quad (7)$$

where E_{tot} is the total energy of the structure with a surface, N is the number of atoms in the structure, ε is the total energy per atom in the bulk, and A is the surface area. Table 1 shows the surface formation energies of many different surfaces constructed from hcp Mg crystals. Results from the present MEAM potentials are in good agreement with the DFT calculations, representing a significant improvement over two of the previously published MEAM potential by Hu *et al.* [Hu01] and EAM potentials by Liu *et al.* [Liu97].

Table 1. Surface-formation energies for hcp Mg. The units are mJ/m^2. The second column indicates if the structure was relaxed. Comparisons with DFT calculations and other previously developed MEAM potentials are also given.

Surface	Relax	DFT	MEAM[a]	MEAM[b]	EAM[c]
(0001)	No	638	604		500
(0001)	Yes	637	595	310	499
(1010)	No	855	642		517
(1010)	Yes	846	523	316	515

[a]The present MEAM potential [Jelinek07]
[b]MEAM potential by Hu *et al.* [Hu01]
[c]EAM potential by Liu *et al.* [Liu97]

Stacking fault is another kind of structure that occurs frequently in real materials and provides a good test environment for empirical potentials. Stacking-fault energy per unit area is defined by

$$E_{sf} = (E_{tot} - N\varepsilon)/A, \quad (8)$$

where E_{tot} is the total energy of the structure with a stacking fault, N is the number of atoms in the system, ε is the total energy per atom in the bulk, and A is the surface area that is perpendicular to the stacking fault. Four stacking-fault types from the calculation of Chetty and Weinert [Chetty97] were examined. Total-energy calculations for I_1, I_2, T_2, and E stacking-fault types were per-

formed using both DFT and MEAM calculations. The results are compared in Table 2. The present

Table 2. Stacking-fault energies for hcp Mg. Results from the present MEAM and DFT calculations are compared. Stacking-fault energies per unit area are given in mJ/m^2. Comparisons with other previously-developed empirical potentials are also given.

Fault	**MEAM**[a]	EAM[b]	MEAM[c]	DFT[d]	DFT[e]
I_1	**7**	27	4	18	21
I_2	**15**	54	8	37	44
T_2	**15**	54		45	51
E	**22**	81	12	61	68

[a]The present MEAM potential [Jelinek07]
[b]EAM potential by Liu *et al.* [Liu97]
[c]MEAM potential by Hu *et al.* [Hu01]
[d]DFT calculations from the present work [Jelinek07]
[d]DFT calculations by Chetty *et al.* [Chetty97]

MEAM potential shows a substantial improvement over the previously published MEAM potential by Hu *et al.* [Hu01]. The stacking-fault energies are consistently underestimated by the present MEAM potentials compared to the results of the DFT calculations, while the results by the EAM potential Liu *et al.* [Liu97] are consistently overestimated.

Recently, we developed another empirical interatomic potential for Mg atoms based on FMEAM instead of MEAM. This new potential is very similar to our previous MEAM potential [Jelinek07] in its performance, but has superior thermal properties during MD simulations. To demonstrate one of its thermal properties, we calculated the melting temperatures of pure Mg crystals. We followed a single-phase method as described by Kim and Tománek [Kim94], in which the temperature is increased at a constant rate and the internal energy of the system is monitored. Figure 4 shows the internal energies of Mg crystal in hcp structure as a function of temperature. The plot was obtained from the ensemble average of five hcp structures containing 448 Mg atoms. The initial velocity vectors were set randomly according to the Maxwell-Boltzmann velocity distribution at T = 100 K. The temperature of the system was controlled by using a Nosé-Hoover thermostat [Nose84, Hoover83]. It is clearly seen from Figure 4 that the internal-energy curve makes an

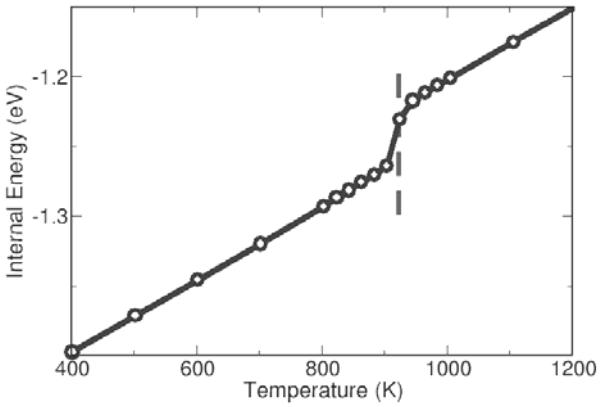

Figure 4. The internal energies of Mg crystal in hcp structure as a function of temperature. The energies are obtained from the ensemble average of the MD simulations of five structures containing 448 Mg atoms. The vertical dashed line indicates the experimental melting temperature 923 K.

abrupt transition from one linear region to another, marking the melting point. Using this method, we obtained 920 K as the melting temperature of Mg crystals. This result is in good agreement with the experimental value of 923 K. Our result represents a substantial improvement in accuracy from 745 K obtained from a previously-published EAM potential [Liu96] or 780 K from a MEAM potential [Jelinek07].

Al Interatomic Potential

We applied the MOO procedure to develop a new interatomic potential for Al based on the MEAM. We used the previously published Al MEAM potentials by Baskes [Baskes92] as the initial set of the parameters for our MOO procedure.

To test the validity of this new Al MEAM potential, we computed the atomic energy of Al atoms in four common configurations, namely fcc, hcp, bcc, and simple cubic (sc) crystal structures, as a function of the atomic volume. The results are summarized in Figure 5. As expected, the curve for the fcc structure produced by the MEAM potential retraces the results of DFT calculations nearly perfectly since fcc was used as the reference structure during the potential construction process. The agreement between the MEAM potential and DFT for the hcp structure is also remarkable. The most important result, however, is the fact that the new MEAM potential correctly identified fcc as the most stable structure for Al.

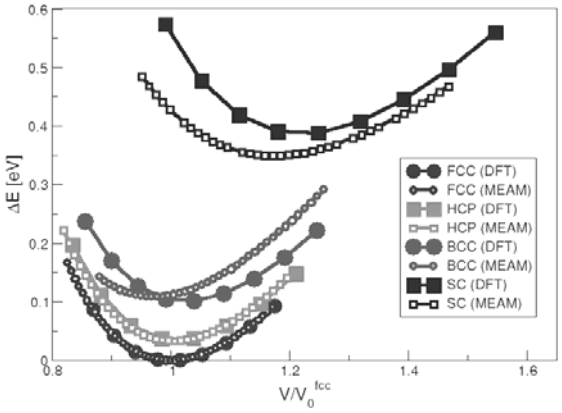

Figure 5. Atomic energies (total energies per atom) as a function of the atomic volume (volume per atom) for Al atoms in fcc, hcp, bcc, and simple cubic (sc) crystal structures. The energies are measured from the equilibrium atomic energy of fcc structure. Volumes are scaled by the equilibrium atomic volume of the fcc structure.

Furthermore, the sequence of the structures is correctly predicted in the order of stability by the Al MEAM potential. The relative cohesive energies, with respect to the one for the fcc structure, are also in good agreement with the DFT calculations, although the result for the simple cubic structure is slightly underestimated.

The relative equilibrium atomic volumes, with respect to the one for the fcc structure, are also well reproduced. We point out that the equilibrium atomic volume for fcc Al, obtained by the MEAM potential (16.61 $Å^3$), is slightly different from the one predicted by DFT (15.76 $Å^3$). This is due to the fact that the MEAM parameters are fitted to reproduce the experimental volume, while DFT within LDA tends to underestimate the equilibrium lattice constants by roughly 1% [Droogenbroeck04, King94].

As another test for the transferability of the Al MEAM potential, surface formation energies for several different surfaces are computed. Table 3 shows the surface formation energies of many different surfaces constructed from fcc Al crystals. Results from the present MEAM potentials are in good agreement with the DFT calculations, representing a significant improvement over two of the previously published MEAM potential by Lee *et al.* [Lee03] and EAM potentials by Liu *et al.* [Liu97].

Table 3. Surface-formation energies for fcc Al. The units are mJ/m^2. The second column indicates if the structure was relaxed. Comparisons with DFT calculations and other previously-developed MEAM potentials are also given.

Surface	Relax	DFT	MEAM[a]	MEAM[b]
(111)	No	992	737	
(111)	Yes	988	731	629
(110)	No	1371	1068	
(110)	Yes	1349	1035	948
(100)	No	1213	1025	
(100)	Yes	1212	1025	

[a]The present MEAM potential [Jelinek07]
[b]MEAM potential by Lee *et al.* [Lee03]
[c]EAM potential by Liu *et al.* [Liu97]

Stacking fault is another kind of structure that occurs frequently in real materials and provides a good test environment for empirical potentials. Three stacking-fault types from the calculation of Chetty and Weinert [Chetty97] were examined. Total energy calculations for I, E, and T stacking-fault types were performed using both DFT and MEAM calculations. The results are compared in Table 4. For the case of stacking fault type *I*, our MEAM result is in good agreement

Table 4. Stacking-fault energies for fcc Al. Results from the present MEAM and DFT calculations are compared. Stacking-fault energies per unit area are given in mJ/m^2. Comparisons with other previously-developed empirical potentials are also given.

Fault	Relaxed	**MEAM[a]**	EAM[b]	DFT[c]	Expt.[d]
I	No	**150**	169	136	
I	Yes	**146**	142	133	140-160
E	No	**150**	169	135	
E	Yes	**148**	154	133	
T	No	**75**	84	62	
T	Yes	**74**	77	61	

[a]The present MEAM potential [Jelinek07]
[b]EAM potential by Liu *et al.* [Liu97]
[c]DFT calculations from the present work [Jelinek07]
[d]Experimental results by Hirth *et al.* [Hirth82]

with the available experimental value even though our DFT result is lower than the experimental value. In all cases considered, the present MEAM potential shows better overall agreement with DFT calculations compared with the EAM potential by Liu *et al.* [Liu97].

Mg-Al Alloy Interatomic Potential

Based on interatomic potentials for Mg and Al atoms, we developed a new interatomic potential for Mg-Al alloy system based on the MEAM by applying the MOO procedure. We used the previously-published MEAM potentials for Mg-Al alloys by Baskes [Baskes92] as the initial set of the parameters for our MOO procedure.

To test the validity of this new MEAM potential for Mg-Al alloy system, we computed the heat of formation per atom for different configurations. In order to compare Mg-Al alloy systems with different stoichiometric coefficients, we define the heat of formation per atom as

$$H_f = \frac{E_{tot} - N_{Mg}\varepsilon_{Mg} - N_{Al}\varepsilon_{Al}}{N_{Mg} + N_{Al}}, \qquad (9)$$

where E_{tot} is the total energy of the system, N_{Mg} and N_{Al} are the numbers of Mg and Al atoms in the system, and ε_{Mg} and ε_{Al} are the total energies per atom for Mg and Al in their ideal bulk structures, respectively. Figure 6 shows the heat of formation per atom H_f for the *B*1, *B*2, and *B*3 structures compared with the results from the DFT calculations. The *B*1 (cubic rocksalt) structure was used as the reference structure for the Mg-Al alloy MEAM potential. Figure 6 shows that the sequence of the structures in the order of stability is predicted correctly by the MEAM potential for the Mg-Al alloy system. The relative cohesive energies, with respect to the one for the reference structure, are also in good agreement with the DFT calculations. The equilibrium atomic volume and bulk modulus of Mg-Al in the *B*1 structure are reproduced almost exactly.

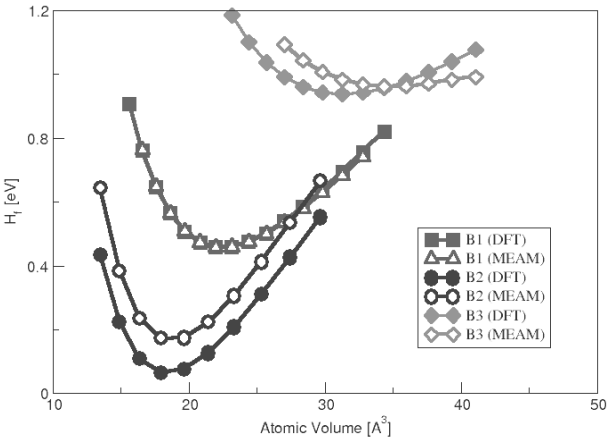

Figure 6. The heat of formation per atom for Mg-Al alloys in the *B*1, *B*2, and *B*3 crystal structures.

To further demonstrate the validity of our potentials, we computed the heat of formation per atom for many intermetallic phases of Mg-Al alloys. The total energy values in Eq. (9) of *B*1, *B*2, *B*3, *C*1, *C*3, *C*9, *C*15, *D*03, *D*09, *A*15, *L*12, and *A*12 structures were evaluated at the optimal atomic volume for each structure. The results from the MEAM calculations, compared with the ones from the DFT calculations, are summarized in Figure 7. Although the Mg and Al atoms in these intermetallic phases are in a chemical environment very different from the one in the reference structure (*B*1), the agreement between MEAM and DFT is quite satisfactory. In most cases, MEAM preserves the order of stability predicted by DFT.

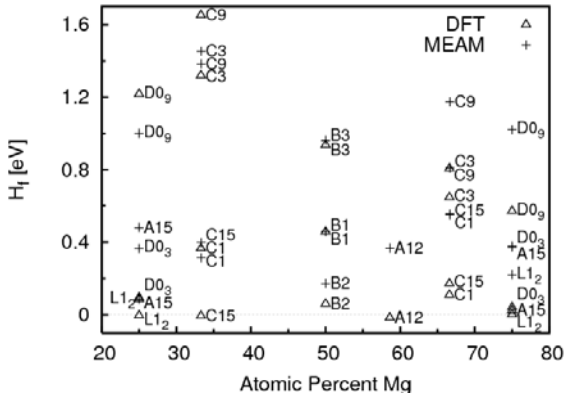

Figure 7. The heat of formation per atom for Mg-Al alloys in various intermetallic phases with different stoichiometric coefficients. The results obtained from the Mg-Al MEAM potentials are compared with the DFT calculations. The structure names are written next to the symbols (open triangles for DFT and crosses for MEAM).

The differences in the heat of formation per atom from MEAM and DFT are less than 0.5 eV at most. However, we note that the MEAM failed to predict that the formation of one of the experimentally-observed Mg-Al alloy structures [Singh03, Okamoto98], $\gamma(Mg_{17}Al_{12})$, denoted as the *A*12 structure in Figure 7, as an exothermic process. In comparison, our DFT calculation correctly predicted the H_f for this structure to be a negative value (−0.017 eV).

Precipitates in a Mg-7Zn-3Al alloy

While typical Mg-Al-Zn casting alloys such as AZ91 are Al-rich, Zn-rich alloys associated with the Zn-rich lower ternary eutectic can provide low-melting compositions with the potential for greater precipitation strengthening. A previous study demonstrated that a MgZnAl aged to peak hardness at 150°C for 100 hrs could reach a yield strength of 190 MPa [Shiao06].

While details of precipitation strengthening in MgAlZn alloys are not well known, the precipitation strengthening in binary MgZn alloys has been well studied. The precipitation sequence in Mg-Zn is well documented starting from Guinier-Preston (GP) zone formation, followed by the formation of β_1' and β_2' metastable precipitates before reaching the formation of equilibrium β phase [Sturkey59, Gallot64, Wei95]. In the present work, the precipitates in a Mg–7Zn–3Al (in wt. %) alloy aged to peak hardness at 150°C have been characterized by 3DAP microanalysis as the basis for calibration of precipitation-strengthening models for alloys design.

3D LEAP Tomography

A ZA73 alloy (Mg–7Zn–3Al) was induction melted under an Ar atmosphere and cast into ingots. The samples were encapsulated together in a pyrex tube in vacuum to prevent oxidation of the Mg and then backfilled with argon to prevent vaporization of the Zn. These samples were heated in a furnace at a solution treatment temperature of 358 °C for 24 hours and then quenched in oil to retain a super-saturated solid solution. Samples were then encapsulated individually and aged in a furnace for 100 hours at 150 °C corresponding to the peak hardness conditions identified in a previous study [Shiao06].

Square bars having a dimension of 0.5 mm × 0.5 mm × 12 mm were cut from the bulk specimens and electropolished to make sharp needle specimens for atom probe analysis. The electropolishing electrolyte was 2% perchloric acid + 2-butoxy ethanol (2% $HClO_4$ + $CH_3(CH_2)_3O(CH_2)_2OH$) and the voltage was initially set at 30 V and reduced to 10 V when pulsing. The sharpened specimens were rinsed in ethanol after electroplishing.

In order to analyze the microstructure of these nanoscale precipitates, 3DAP tomography was employed. Atom-probe tomography utilizes a combination of time-of-flight mass spectrometry and point-projection microscopy to chemically identify and locate individual atoms within a bulk sample. Atom-probe specimens are needles or tips sharpened to less than 100 nm in diameter. A positive voltage pulse is applied to the sharpened tip, causing field evaporation of positively-charged metal ions that are subsequently drawn to a detector plate along a voltage differential. The chemical identity of each ion is revealed through the mass-to-charge ratio as determined by the time-of-flight between the applied pulse and point of detection. The x and y coordinate of each ion within the sample is then determined from the point of impact on the two-dimensional (2D) detector, and the depth (or z coordinate) is determined by the sequence number or absolute time of impact.

For this research, a new generation atom probe is employed termed a local-electrode atom probe (LEAP^{TM}). The LEAP improves upon conventional 3DAP by generating the electric field through a localized extraction electrode. Due to the close proximity of the electrode to the specimen tip, the voltage requirements for field evaporation are much smaller and can be pulsed at much higher frequencies (2×10^5 Hz), significantly raising the data-collection rate. The electrode also serves to shield evaporated ions from the effect of the cycling electric field near the specimen tip, providing for increased mass resolution (greater than 1/500 full-width at half-maximum (FWHM)) at large fields-of-view up to 40. The practical result of these improvements is the ability to

reconstruct significant volumes of material (>10^6 nm^3) in a matter of hours instead of days, making the LEAP comparable to other conventional forms of microscopy used to study the nanoscale. The LEAP tomograph at the Northwestern University Center for Atom Probe Tomography (NUCAPT) was employed in this study.

Atom-probe tomography was performed using a LEAP™ 3000 tomograph manufactured by Imago Scientific Instruments Corporation in Madison, WI. Analyses were performed after cooling specimens to a temperature of 40 K to minimize atomic motion while under ultra-high vacuum (residual pressure <10^{-8} Pa). Field evaporation of atoms from the specimen tip was achieved through applied high-voltage pulses at a frequency of 200 kHz. Voltage is applied to the specimen tip through a standing direct-current (DC) voltage with voltage pulses applied through the extraction electrode at a pulse-to-DC voltage ratio of 15%. The voltage levels required for field evaporation are dependent on the radius of curvature of each specimen tip, with the standing DC voltage ranging from 500 V for very sharp tips (diameter < 10 nm) to 15,000 V for larger tips (~ 100 nm diameter). Steady field evaporation rates of 400-10,000 atoms/second were maintained through software-controlled manipulation of the voltage levels, with applied voltage steadily increased to account for tip blunting with continued specimen evaporation.

An alternative mode of operation of pulsed-laser evaporation reduces the frequency of nanowire fracture by eliminating the voltage pulses in favor of more localized laser excitation, which does not produce a repetitive stress on the sample. The precise mechanisms by which the laser promotes ion evaporation are still being debated, but it seems clear that local heating on very short (picosecond) timescales promotes thermally-assisted field evaporation. In addition to reducing specimen fracture, laser pulsing generally produces sharper mass spectra and fewer unidentified peaks. Both voltage-pulse and laser-pulse modes of field evaporation were applied in this study.

Reconstruction and quantitative analysis of collected data sets were performed with the IVAS 3.0 software from Imago Scientific Instruments.

The volume of the analyzed material (v_{total}) was calculated from the total number of ions in the reconstruction (n) using

$$v_{total} = \frac{n\Omega}{f} \qquad (10)$$

where the average atomic volume, Ω, is set equal to that of bcc Fe (1.18×10^{-2} nm^3) and the overall detection and reconstruction efficiency (f) is estimated at 0.6. Standard deviations (σ) of measured compositions through the LEAP analysis were calculated using Eq. (10) [Miller00]:

$$\sigma_c = \sqrt{c(1-c)/N} \qquad (11)$$

where c is the measured composition of the particular element, N is the total number of atoms detected. To quantify the two precipitate dispersions, two tools are used in the IVAS software: isoconcentration surfaces and 1D composition profiles. Isoconcentration surfaces are essentially 3D compositional contour maps, where a threshold composition is selected for one or a combination of elements and a surface is drawn connecting the selected concentration. 1D compositional profiles were generated through a cylindrical selection volume 1 nm in diameter at various lengths. Composition profiles are generated by counting the number and type of each atom contained within the cylinder over increments 0.1-nm thick.

Results and Discussion

Figure 8 displays LEAP tomographic reconstructions for the ZA73 alloy aged at 423 K for 100 hours using the voltage mode. Compared

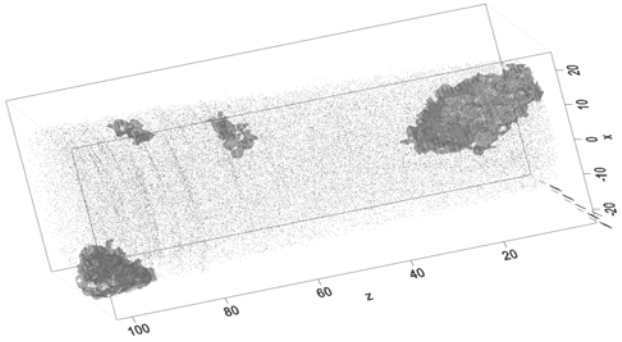

Figure 8. LEAP tomographic reconstructions of 5 % Zn isoconcentration surfaces for the ZA73 alloy aged at 423 K for 100 hours using the voltage mode.

with the bulk alloy composition, a good agreement has been obtained in the Zn content. However, a small discrepancy exists in the Al content.

A proximity histogram (proxigram) showing the concentration of Mg, Zn, Al and Ca as a function of radial distance from the precipitate interface is also presented in Figure 9. It is apparent that both Zn and Al partition to the precipitates. The Zn and Al contents are very low in the matrix. The approximate chemical compositions of the matrix and the precipitates can be read in this proximity diagram. The average chemical compositions of the matrix and the precipitates are reported in Table 5.

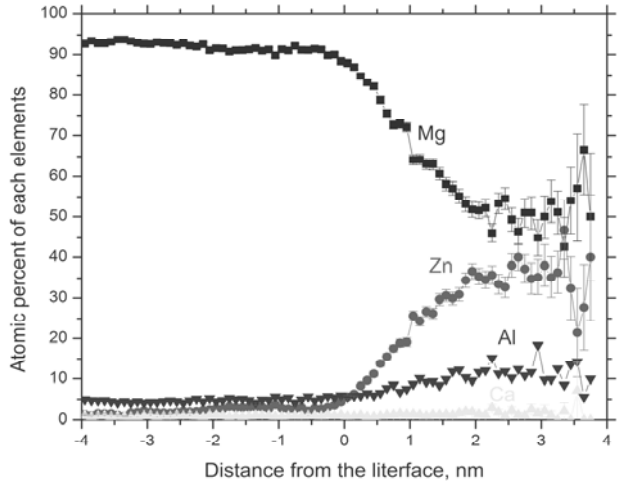

Figure 9. Proximity histogram for the LEAP tomographic reconstructions displayed in Figure 8 showing the average concentration of Mg, Al, Zn and Ca as a function of distance from the Mg-Zn-Al ternary heterophase interface, as defined by a 5 at. % Zn isoconcentration surface. Concentration error bars are calculated as $\sigma_c = \sqrt{c(1-c)/N}$, where N is the total number of atoms detected.

Table 5. Composition of the matrix and the precipitates in ZA73 alloy as measured by LEAP spectrometry (voltage mode) and by calculations using Thermo-Calc and COST2 database.

at %	Matrix			Precipitates		
Elements	Mg	Zn	Al	Mg	Zn	Al
LEAP	95.06	1.08	4.50	51.79	38.08	10.13
Thermo-Calc	96.97	1.63	1.40	37.46	47.47	15.07

Figure 10 displays LEAP tomographic reconstructions for a second equivalent specimen using the laser mode. Compared with Thermo-Calc predictions, good agreement has been obtained in the Zn content. However, a small discrepancy exists in the Al content. The specimen composition is distinctly different from the first specimen, consistent with the expected inhomogeneity of the cast alloy.

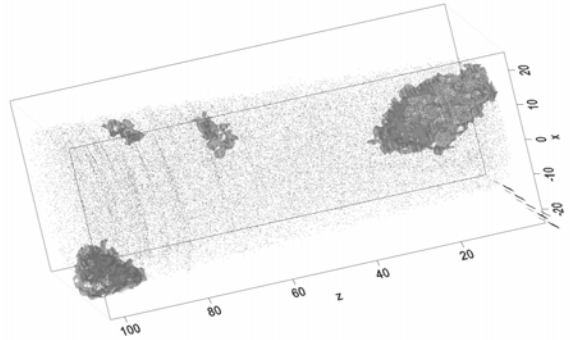

Figure 10. LEAP tomographic reconstructions of 5 % Zn isoconcentration surfaces for the ZA73 alloy aged at 423 K for 100 hours using the laser mode.

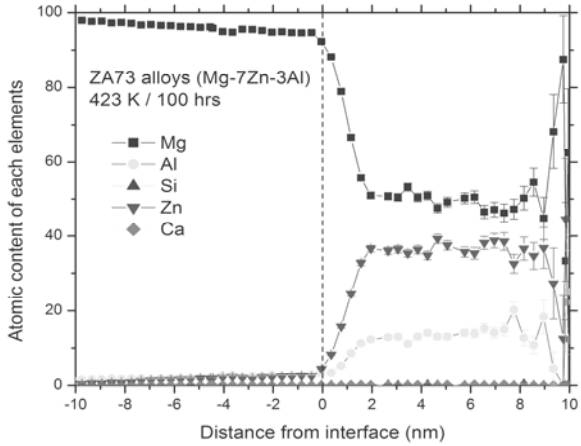

Figure 11. Proximity histogram for the LEAP tomographic reconstructions displayed in Figure 10 showing the average concentration of Mg, Al, Zn and Ca as a function of distance from the Mg-Zn-Al ternary heterophase interface, as defined by a 5 at. % Zn isoconcentration surface. Concentration error bars are calculated as $\sigma_c = \sqrt{c(1-c)/N}$, where N is the total number of atoms detected.

A proxigram showing the concentration of Mg, Zn, Al and Ca as a function of radial distance from the precipitate interface is also presented in Figure 11. It is again apparent that both Zn and Al partition to the precipitates, while the Zn and Al contents are very low in the matrix. The average chemical compositions of the matrix and the precipitates are reported in Table 6.

Table 6. Composition of the matrix and the precipitates in ZA73 alloy as measured by LEAP spectrometry (laser mode) and by calculations using Thermo-Calc and COST2 database.

at. %	Methods	Mg	Zn	Al	Ca
Matrix	LEAP	98.25	0.54	1.16	0.04
	Thermo-Calc	98.52	0.57	0.91	--
Precipitate	LEAP	54.80	32.39	12.75	0.055
	Thermo-Calc	54.55	23.85	21.61	--

The Thermo-Calc calculation shows that hcp and φ phases ($Mg_6(Zn, Al)_5$) are in equilibrium. The calculated isopleth section of Mg-3Al-Zn alloy with the different Zn content and isothermal sections of the Mg-Al-Zn system at 423 K are shown in Figures 12, 13, 14 and 15.

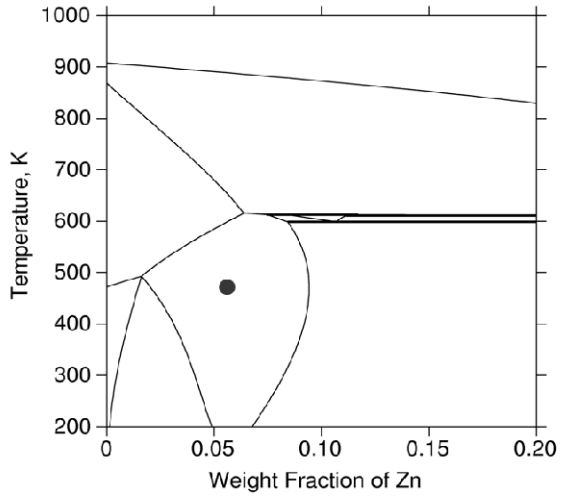

Figure 12. Calculated isopleth section of Mg-3Al-Zn alloy with varying Zn content. The dark dot is the chemical composition point of ZA73 alloy at aging temperature of 423 K.

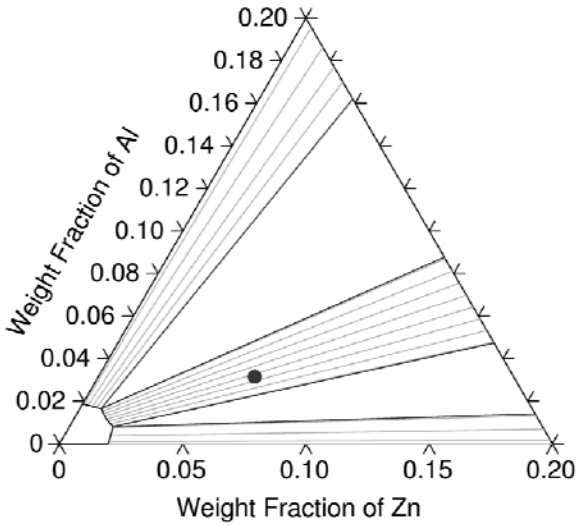

Figure 13. The enlarged view of the Zn-rich corner at 423 K. The light-grey lines are the tie lines which indicate the two phases' regions. The dark dot is the chemical composition point of the ZA73 alloy.

Combining the results using voltage mode and the laser mode, the equivalent sphere diameter of precipitates is 20 – 50 nm at peak hardness, providing calibration for precipitation-strengthening models.

Figure 14 shows the enlarged view of the Zn-rich corner at 423 K represented in mole fractions with

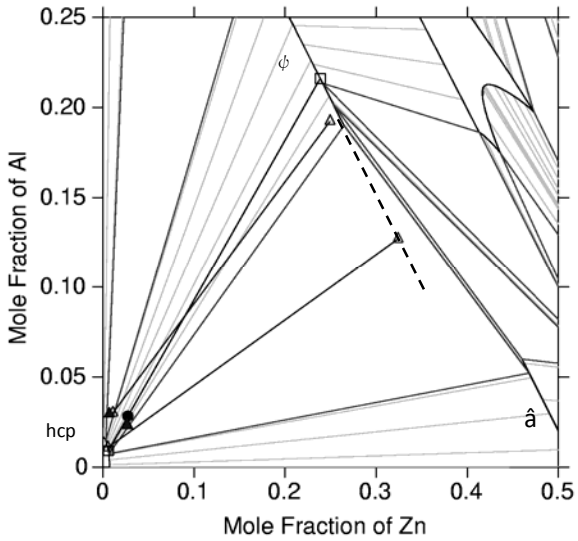

Figure 14. The enlarged view of the Zn-rich corner at 423 K represented in mole fraction. The light-grey lines are the predicted tie lines which indicate the two phases regions. The darker lines are the tie-lines measured by LEAP. The tie-line via voltage mode connects to the extended φ phase. The tie-line via laser mode is in the stable hcp + φ two phase region.

the darker tie-lines detected by LEAP. The tie-line of the sample analyzed via voltage mode connects to the extended φ phase. The tie-line of the sample analyzed via laser mode is in the stable hcp + φ two-phase region.

Figure 15 displays the calculated metastable two-phase region between the hcp and φ phase at 423 K, with light-grey tie-lines to show their directions. The trends are similar to the experimental tie-lines of Figure 14.

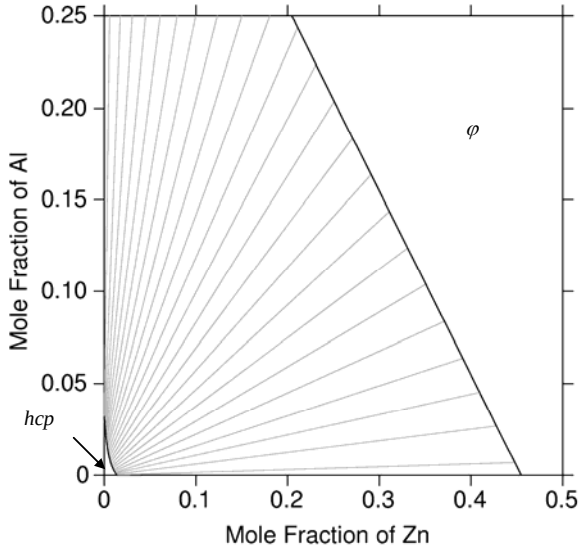

Figure 15. Calculated metastable isothermal section at 423 K between hcp and φ phase. The light-grey lines are the calculated tie lines showing directions similar to the data of Figure 14.

Conclusions

One of the main goals of this project is to understand the effect of nanoscale precipitates and novel additives to the overall strength and ductility in Mg alloy systems. We developed a new MOO methodology as a robust procedure to construct reliable and transferable interatomic potentials for Mg-based alloy systems. This MOO procedure was applied to construct transferrable interatomic potentials for Mg and Al atoms using the FMEAM. We also established a basic framework for the accelerated development of reliable and efficient interatomic potentials for other combinations of alloy systems to perform large-scale, realistic atomistic simulations.

The nanostructure of strengthening precipitates in a Mg-7Zn-3Al aged to peak hardness at 423 K for 100 hrs was investigated. The chemical compositions of the alloys as well as the matrix and the precipitates were measured by LEAP spectrometry and compared with the results calculated by the Thermo-Calc software based on the COST2 database. Ternary nano-sized precipitates have been found. The precipitates have compositions consistent with the ternary φ phase including its metastable extension. The precipitate size at peak hardness corresponds to an equivalent sphere diameter of 20 – 50 nm.

This investigation should facilitate the design of a new generation of Mg-based alloys with improved castability and high-temperature creep resistance by providing fundamental understanding of several critical issues that include the selection of key combination of precipitates and matrices, interaction of precipitate and matrix phases and, ultimately, composition-structure-property relationship.

Presentations/Publications/Patents

1. Bohumir Jelinek, Sungho Kim, Jeffery Houze, Seong-Gon Kim, M. F. Horstemeyer, and M. I. Baskes, *"Development and testing of MEAM Potentials for Al-Mg Alloys"*, APS 2006 SESAPS Meeting, Williamsburg, VA, November 2006.
2. B. Jelinek, J. Houze, Sungho Kim, M. F. Horstemeyer, M. I. Baskes, and Seong-Gon Kim, *"Modified embedded-atom method interatomic potentials for the Mg-Al alloy system"*, Phys. Rev. B, 75, 054106 (2007).
3. J. Houze, Sungho Kim, Amitava Moitra, B. Jelinek, Sebastien Groh, M. F. Horstemeyer, Erdem Acar, Masoud Rais-Rohani, Seong-Gon Kim, *"A multi-objective optimization procedure to develop modified-embedded-atom-method potentials: an application to magnesium"*, submitted to Phys. Rev. B., arXiv:0708.0075.
4. Shengjun Zhang and Gregory B. Olson, *"3D-atom probe investigation of strengthening precipitates in a Mg-7Zn-3Al alloy"*, preprint.
5. S. Groh, B. Jelinek, J. Houze, Seong-Gon Kim, M. F. Horstemeyer, *"Mobility of <a> dislocations in Mg and Mg/Al alloys by molecular dynamic simulations"*, submitted to Computational Materials Science.

References

1. [Baskes87] M. I. Baskes, *"Application of the Embedded-Atom Method to Covalent Materials: A Semiempirical Potential for Silicon"*, Phys. Rev. Lett. 59, 2666 (1987).
2. [Baskes89] M. I. Baskes, J. S. Nelson, and A. F. Wright, *"Semiempirical modified embedded-atom potentials for silicon and germanium"*, Phys. Rev. B 40, 6085 (1989).
3. [Baskes92] M. I. Baskes, *"Modified embedded-atom potentials for cubic materials and impurities"*, Phys. Rev. B 46, 2727 (1992).
4. [Baskes94] M. I. Baskes, J. E. Angelo and C. L. Bisson, *"Atomistic calculations of composite interfaces"*, Modell. Simul. Mater. Sci. Eng. 2, 505 (1994).
5. [Blochl94] P. E. Blöchl, *"Projector augmented-wave method"*, Phys. Rev. B 50, 17953 (1994).
6. [Ceperley80] D. M. Ceperley and B. J. Alder, *"Ground State of the Electron Gas by a Stochastic Method"*, Phys. Rev. Lett. 45, 566 (1980).
7. [Cherne01] F. J. Cherne, M. I. Baskes, and P. A. Deymier, *"Properties of liquid nickel: A critical comparison of EAM and MEAM calculations"*, Phys. Rev. B 65, 024209 (2001).
8. [Chetty97] N. Chetty and W. Weinert, *"Stacking faults in magnesium"*, Phys. Rev. B 56, 10844 (1997).
9. [Coleman67] B. D. Coleman and M. E. Gurtin, *"Thermodynamics with internal state variables"*, J. Chem. Phys. 47, 597 (1967).
10. [Daw83] M. S. Daw and M. I. Baskes, *"Semiempirical, Quantum Mechanical Calculation of Hydrogen Embrittlement in Metals"*, Phys. Rev. Lett. 50, 1285 (1983).
11. [Daw84] M. S. Daw and M. I. Baskes, *"Embedded-atom method: Derivation and application to impurities, surfaces, and other defects in metals"*, Phys. Rev. B 29, 6443 (1984).
12. [Droogenbroeck04] Joris Van Droogenbroeck, Karla Tersago, Christian Van Alsenoy and Frank Blockhuys, *"A systematic study of the effect of correlation, DFT functional and basis set on the structure of Roesky's ketone"*, Chem. Phys. Lett. 399, 516 (2004).
13. [deWeck04] O. L. de Weck, *"Multiobjective Optimization: History and Promise (The Third China-Japan-Korea Joint Symposium on Optimization of Structural and Mechanical Systems"*, Kanazawa, Japan, (2004).
14. [E03] W. E and B. Engquist, *"Multiscale Modeling and Computation"*, Notices of the AMS 50, 1062 (2003).
15. [Espinosa01] H. D. Espinosa, H. -C. Lu, P. D. Zavattieri, and S. Dwivedi, *"A 3-D Finite Deformation Anisotropic Visco-Plasticity Model for Fiber Composites,"* J. of Composite Materials 35, 369 (2001).
16. [Ercolessi94] F. Ercolessi and J.B. Adams, *"Interatomic potentials from first-principles calculations: the Force-Matching method"*, Europhys. Lett. 26, 583 (1994).
17. [Gailly02] B. A. Gailly and H. D. Espinosa. *"Modelling of Failure Mode Transition in Ballistic Penetration with a Continuum Model Describing Microcracking and Flow of Pulverized Media*", Int. J. for Numerical Methods in Engineering, 54, 365 (2002).
18. [Gallot64] J. Gallot and R. Graf, Comptes. Rendus. Acda. Sci. 258, 2818 (1964).
19. [Hao03] Su Hao, Brian Moran, Wing Kam Liu, and Gregory B. Olson, *"A hierarchical multi-physics model for design of high toughness steels"*, Journal of Computer-Aided Materials Design, 10, 99 (2003).
20. [Hao04] Su Hao, Brian Moran, Wing Kam Liu, and Gregory B. Olson, *"Multi-scale constitutive model and computational framework for the design of ultra-high strength"*, Computer Methods in Applied Mechanics and Engineering 193, 1865 (2004).
21. [Hasan95] O. A. Hasan and M. C. Boyce, *"A Constitutive Model for the Nonlinear Viscoelastic Behavior of Glassy Polymers,"* Polymer Engng. and Sci. 35, 331 (1995)/.
22. [Hirth82] J. P. Hirth and J. Lothe, *"Theory of Dislocations,"* John Wiley and Sons Inc, New York (1982).
23. [Horst01] M. F. Horstemeyer, S. J. Plimpton, and M. I. Baskes. *"Size Scale and Strain Rate Effects on Yield and Plasticity of Metals"*, Acta Matallurgica 49, 4363 (2001).
24. Horst03] M. F. Horstemeyer and P. Wang. *"Cradle-to-grave simulation-based design incorporating multiscale microstructure-property modeling: Reinvigorating design with science"*, Journal of Computer-Aided Materials Design 10, 13 (2003).

25. [Hoover83] William G. Hoover, *"Canonical dynamics: Equilibrium phase-space distributions"*, Phys. Rev. A 31, 1695 (1983).
26. [Hu01] Wangyu Hu, Bangwei Zhang, Baiyun Huang, Fei Gao and David J Bacon. *"Analytic modified embedded atom potentials for HCP metals"*, J. Phys.: Condens. Matter 13, 1193 (2001).
27. [Jelinek07] B. Jelinek, J. Houze, Sungho Kim, M. F. Horstemeyer, M. I. Baskes, and Seong-Gon Kim, *"Modified embedded-atom method interatomic potentials for the Mg-Al alloy system"*, Phys. Rev. B 75, 054106 (2007).
28. [Kim94] S. G. Kim and D. Tománek, *"Melting the fullerenes: A molecular dynamics study"*, Phys. Rev. Lett. 72, 2418 (1994).
29. [Kim05] I. Y. Kim and O. L. de Weck, Structural and Multidisciplinary Optimization 31, 105 (2005).
30. [King94] R. D. King-Smith and David Vanderbilt, *"First-principles investigation of ferroelectricity in perovskite compounds"*, Phys. Rev. B 49, 5828 (1994).
31. [Kohn65] W. Kohn and L. J. Sham, *"Self-consistent Equations Including Exchange and Correlation Effects*", Phys. Rev. 140, A1113 (1965).
32. [Kresse93] G. Kresse and J. Hafner, *"Ab initio molecular dynamics for liquid metals"*, Phys. Rev. B 47, 558 (1993).
33. [Kresse96] G. Kresse and J. Furthmüller, *"Efficient iterative schemes for ab initio total-energy calculations using a plane-wave basis set"*, Phys. Rev. B 54, 11169 (1996).
34. [Kresse99] G. Kresse and D. Joubert, *"From ultrasoft pseudopotentials to the projector augmented-wave method,"* Phys. Rev. B 59, 1758 (1999).
35. [Kestin70] J. Kestin and J. R. Rice, *"Paradoxes in the application of thermodynamics to strained solids"*, in "A Critical Review of Thermodynamics", edited by E.G. Stuart, B. Gal-Or, and A. J. Brainard, Mono Book Corp., Baltimore, 275 (1970).
36. [Lee03] Byeong-Joo Lee, Jae-Hyeok Shim, and M. I. Baskes, *"Semiempirical atomic potentials for the fcc metals Cu, Ag, Au, Ni, Pd, Pt, Al, and Pb based on first and second nearest-neighbor modified embedded atom method"*, Phys. Rev. B 68, 144112 (2003).
37. [Lee06] Byeong-Joo Lee, *"A modified embedded-atom method interatomic potential for the Fe—C system,"* Acta Materialia 54, 7011 (2006).
38. [Li03] Youhong Li, Donald J. Siegel, James B. Adams, and Xiang-Yang Liu, *"Embedded-atom-method tantalum potential developed by the force-matching method"*, Phys. Rev. B 67, 125101 (2003).
39. [Liu96] Xiang-Yang Liu, James B Adams, Furio Ercolessi and John A Moriarty, *"EAM potential for magnesium from quantum mechanical forces,"* Modell. Simul. Mater. Sci. Eng. 4, 293 (1996).
40. [Liu97] X.-Y. Liu, P. P. Ohotnicky, J. B. Adams, C. Lane Rohrer, and R. W. Hyland, Jr., *"Anisotropic surface segregation in Al-Mg alloys"*, Surf. Sci. 373, 357 (1997).
41. [Miller00] M. K. Miller, *"Atom probe tomography: analysis at the atomic level,"* Kluwer Academic/ Plenum Publishers, New York, (2000).
42. [Nose84] Shuichi Nosé, *"A unified formulation of the constant temperature molecular dynamics methods"*, J. Chem. Phys. 81, 511 (1984).
43. [Okamoto98] H. Okamoto, *"Al-Mg (Aluminum--Magnesium)"*, J. Phase Eq. 19, 598 (1998).
44. [Olson98] G. Olson. *"Systems design of hierarchically structured materials: Advanced steels"*, Journal of Computer-Aided Materials Design 4, 143 (1998).
45. [Olson00] G. Olson. *"New age of design"*, Journal of Computer-Aided Materials Design 7, 143 (2000).
46. [Perdew81] J. P. Perdew and A. Zunger, *"Self-interaction correction to density-functional approximations for many-electron systems"*, Phys. Rev. B 23, 5048 (1981).
47. [Perdew96] J. P. Perdew, K. Burke, and M. Ernzerhof, *"Generalized Gradient Approximation Made Simple"*, Phys. Rev. Lett. 77, 3865 (1996).
48. [Press92] William H. Press, Brian P. Flannery, Saul A. Teukolsky, and William T. Vetterling, *Numerical Recipes in C: The Art of Scientific Computing*, 2nd ed., Cambridge University Press, Cambridge (1992).
49. [Rice71] J.R. Rice, *"Inelastic constitutive relation for solids: An internal variable theory*

and. its application to metal plasticity", J. Mech. Phys. Solids 19, 433 (1971).
50. [Shiao06] C. Shiao, *"Design of a Self-Healing Alloy for the Application of Unmanned Aerial Vehicles"*, Senior Project Report, Northwestern University (2006).
51. [Singh03] D. Singh, C. Suryanarayana, L. Mertus, and Chen R.-H., *"Extended homogeneity range of intermetallic phases in mechanically alloyed Mg-Al alloys,"* Intermetallics 11, 373 (2003).
52. [Sturkey59] L. Sturkey and J. B. Clark, Journal of the Institute of Metals 88, 177 (1959).
53. [Wei95] L. Y. Wei, G. L. Dunlop and H. Westengen, Metall. Mater. Trans. A-Phys. Metall. Mater. Sci. 26, 1705 (1995).

J. Multiscale Microstructure-Property Plasticity Considering Uncertainty

Mark F. Horstemeyer: Principal Investigator
Chair in Solid Mechanics & Professor, Mechanical Engineering
Center for Advanced Vehicular Systems (CAVS)
Mississippi State University (MSST)
206 Carpenter Bldg., PO Box ME
Mississippi State, MS 39762
(662) 325-7308; fax: (662) 325-7223; e-mail: mfhorst@me.msstate.edu

D. J. Bammann: Co-Principal Investigator
Professor, Mechanical Engineering
MSST
210 Carpenter Bldg.
Mississippi State, MS 39762
(662) 325-3260; Home: (662) 294-2585; fax: (662) 325-5433; *e-mail: bammann@cavs.msstate.edu*

E. B. Marin: Co-Principal Investigator
Senior Structural Analyst
CAVS
MSST
200 Research Blvd.
Mississippi State, MS 39762
(662) 325-6696; fax: (662) 325- 5433; e-mail: ebmarin@cavs.msstate.edu

Kiran Solanki: Research Associate II
CAVS
MSST
200 Research Blvd.
Mississippi State, MS 39762
(662) 325-5454; fax: (662) 325-5433; e-mail: kns3@cavs.msstate.edu

Sebastien Groh: Postdoctoral Fellow
CAVS
MSST
200 Research Blvd.
Mississippi State, MS 39762
(662) 325-5431; fax: (662) 325- 5433; e-mail: groh@cavs.msstate.edu

Technology Area Development Manager: Joseph A. Carpenter
(202) 586-1022; fax: (202) 586-1600; e-mail: joseph.carpenter@ee.doe.gov

Contract Monitor: Aaron Yocum
(304) 285-4852; fax: (304) 285-4403; e-mail: aaron.yocum@netl.doe.gov

---

Contractor: MSST
Contract No.: 4000054701

Objective

- Develop a multiscale, nested, internal state variable (ISV) modeling methodology that includes statistical variations from the material microstructure for lightweighting designs made of various structural alloys.

Approach

- The approach is to quantify structure-property relations through multiscale modeling and multiscale experiments so the macroscale ISVs can capture the lower length-scale effects. Once the cause-effect relations are quantified for various engineering metal alloys, then statistical methods can be used in the context of the ISVs and used for constitutive models in finite-element analysis (FEA). As such, the FEA can be used for a simulation-based design methodology as manufacturing processes and in-service life are accurately modeled.

Accomplishments

- We have made progress at all scales of simulations and have applied the current nested ISVs into a macroscale finite-element code. We have introduced a crystal-plasticity code that can include different volume fractions of hexagonal close-packed (hcp) magnesium (Mg) with different volume fractions of face-centered cubic (fcc) aluminum (Al) in order to evaluate the plastic deformation of different alloying solutions. With the macroscale ISV theory, we have conducted some materials-processing studies that capture the structure-property relations in the model-correlation and model-validation stages for hydroforming and rolling of various metals. In doing so, we show the importance of the deformation history. In these simulations we are working with other projects at MSST: "Simulation-Based Design Optimization" (see 6.G), "Material Design for Steel Alloys" (atomistic simulations, see 5.M), "Cyberinfrastructure" (see 6.K), and "Mission Eggcellence – K-12 Outreach Program" (see 12.E). These projects are also sponsored by DOE. Finally, we have started the inclusion of the statistical variations and uncertainty within the macroscale ISV model.

Future Direction

- In the next year, we will conclude these studies that we have started and start bridging the different length-scale studies and the different manufacturing histories and in-service life histories.

Introduction

Several sections will show the multiscale modeling and the macroscale modeling of the history of the materials-processing steps for several processes and materials.

Mesoscale Crystal-Plasticity Simulations of Mg-Al Alloys

Renewed interest has been shown in Mg alloys as methods of forming and working have improved and the need for lighter-weight components has increased. Al is one of the most common alloying elements used to improve the properties of Mg. In this regard, particular reference can be made to the Al-zinc (Zn) ternary systems (AZ alloys) where the Al content is important. These alloys are widely used in industrial applications, with major commercial grades being AZ31 (3% Al), AZ61 (6% Al) and AZ91 (9% Al). In general, the addition of Al atoms to pure Mg leads to the formation of solid solutions and/or new second phases, with the particular microstructure formed being strongly influenced by the concentration of Al atoms as well as the heat-treatment conditions (temperature and cooling rate) employed to produce the alloy. Equilibrium (stable) or metastable structures can be obtained in this process and which can be analyzed with the help of phase diagrams.

In this work, a crystal-plasticity (mesoscale) model is used to examine the deformation behavior of Mg alloys with varying amounts of Al. For this study, it is assumed that the Mg-Al alloy has a hypothetical microstructure where the Al impurity atoms have formed a dispersed second phase (fcc grains) in the Mg matrix (hcp grains). The study of this system using a crystal-plasticity approach allows a more-accurate representation of the microstructure as discrete grains and their crystallographic properties (slip systems); and, some aspects of phase distribution can be explicitly modeled. This is particularly beneficial

in this case as the differences in texture evolution and grain interaction due to the presence of the Al can be observed. The tests will begin to show how properties of the two phases combine to form the macroscopic properties of the alloy and how the individual properties of each separate phase change due to the presence of the other phase.

Modeling Procedure

The model used is a crystal elasto-viscoplastic model based upon a previous rigid viscoplastic formulation (Marin and Dawson, 1998). The kinematics of the model assume that crystallographic slip is the dominant mechanism of deformation. The model does not incorporate twinning behavior although it has been shown to have a profound effect on Mg behavior. Implementation of twinning to more accurately capture the deformation process is planned for next year. The current model was implemented as a user material routine in *ABAQUS.* Meshes were created to show the change in stress-strain response when varying the number of Al grains present in the Mg alloys. Each case used a cube of 25x25x25 elements with each of the 15,625 elements representing a single grain. For these simulations, eight-node brick elements with reduced integration were selected. The percentages of Al grains tested were 0%, 3%, 6%, 9%, 12%, and 15% with the remaining grains being Mg. The Al grains were assigned randomly as can be observed in the models shown in Figure 1.

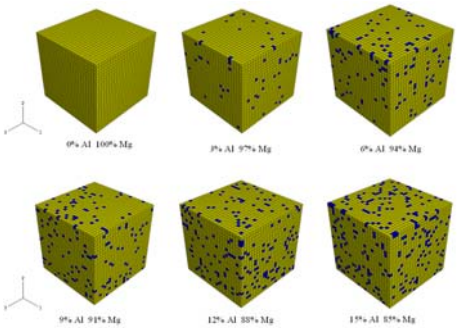

Figure 1. Models showing composition of Al and Mg.

For each of the models. the Euler angles of the grains were assigned randomly so that no initial texture was present. The models were loaded in plane-strain compression at a constant strain rate of 10^{-3} by fixing the faces normal to the 1 direction, the rear face normal to the 3 direction, and the bottom face normal to the 2 direction. Displacement loading was specified on the top face in the -2 direction and the left-front face in the 3 direction. The elastic constants used for the Al were taken from (Dawson, Boyce, MacEwen, and Rogge, 2001). The material parameters for the crystal-plasticity model for Al were taken from (Marin and Dawson, 1998). The elastic constants for the Mg were taken from (Kocks, Tome, and Wenk, 1998). The material parameters for the Mg were determined by fitting published experimental compression data of pure untextured Mg from (Agnew, Yoo, and Tome, 2001). The deformed meshes are shown in Figure 2. The stress-strain responses of the cases are shown in Figure 3.

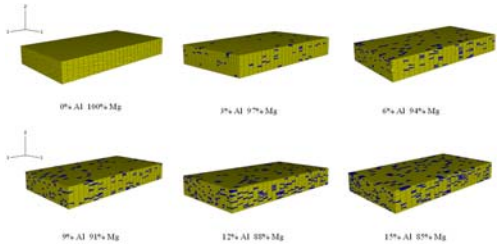

Figure 2. Models after plane-strain compression.

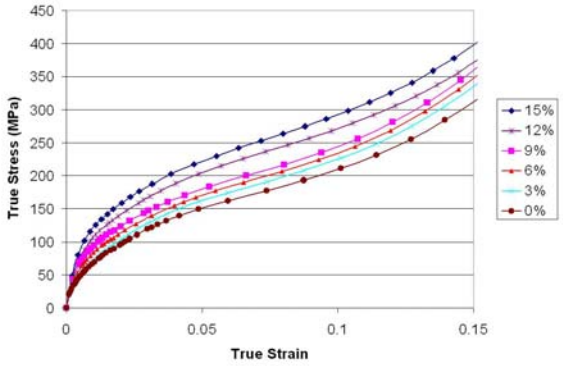

Figure 3. Stress-strain response of Mg alloys containing varying percentages of Al.

Summary and Future Work

The inhomogenous deformation of the models is apparent in Figure 2 as the grains all deformed differently from one another. The considerable difference in shape of the final deformed grains is due to the crystal anisotropic properties, the difference in crystallographic orientation between neighboring grains, and the presence of grains of two distinct phases. Figure 3 shows that the

strength of the alloy increases as the amount of Al increases. This demonstrates the usefulness of alloying in improving the properties of Mg as the 15%-Al Mg alloy is considerably stronger than the pure Mg. The curves also seem to indicate a rule of mixtures as the strength increases by an amount consistent with the increase in Al. The results are encouraging and suggest that more information may be gathered through crystal-plasticity testing of this type.

Future plans include the representation of twinning behavior in the crystal-plasticity model and examination of the texture evolution of the fcc and hcp phases. The evaluation and incorporation of lower length-scale hardening rules are planned from the use of atomistic simulations and dislocation dynamics. Experiments are also planned to help quantify the evoluation to texture, twinning, and dislocation activity upon various stress states.

Modeling the Hydroforming Process of T-Shape Copper (Cu) Tube Fittings

Tube hydroforming is an important forming technology used in the automotive industry. Although steel has been typically used in the majority of automotive applications, Al hydroforming has started to have its place in this area, in particular, for the production of lightweight automotive structures.

In this section, we present a summary of the macroscale ISV modeling and simulation work that has been performed in tube hydroforming using some aspects of the technology being developed in this program. Although the material used in this work is Cu and the application is plumbing, the established methodology and models can be extended to other materials and application areas. The specific work concerns the numerical analysis of the hydroforming process of Cu tube fittings used by a local manufacturing company (Mueller Industries, Inc.).

This study involves constructing a finite- element (FE) model of the process, performing mechanical and microstructural characterization analyses on the tube's material, using a multiscale constitutive model to represent the material response during the process, validating the hydroforming model, and performing the statistical analysis of the forming process to determine the most important parameters of the process. Through this numerical study, the manufacturer should be able to learn more about the process behavior and, hence, establish guidelines to better plan/improve its hydroforming process.

A synopsis of the Mueller hydroforming process is presented in Figure 4. A Cu blank with a previous deformation history (extruded, drawn, annealed) is being formed by a simultaneous application of axial velocity and internal pressure loads.

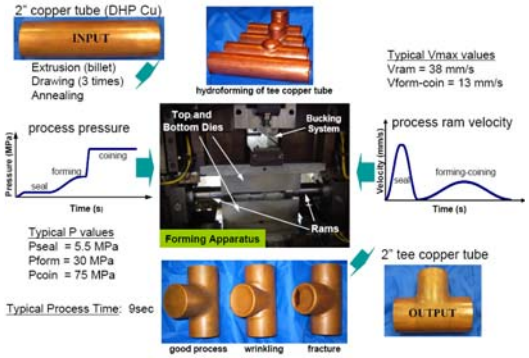

Figure 4. Mueller's hydroforming process for 2" T-shape Cu tube fittings.

In general, modeling the hydroforming process should account for the six components of the system: two rams, top and bottom die, Cu blank, and the bucking plate; see Figure 5. However, due to symmetry, only one quarter model can be used. The three-dimensional FE mesh of the hydroforming components (die, bucking plate, ram and Cu billet) is also presented in Figure 5. In this FE model, all components are represented as rigid bodies except the Cu blank, which is deformable.

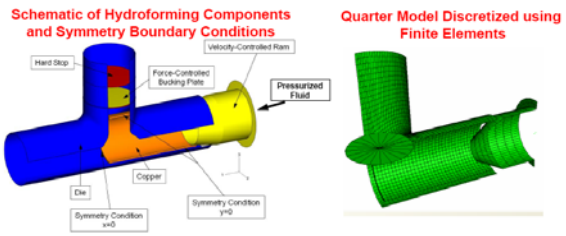

Figure 5. Hydroforming components and finite-element mesh of quarter model.

Characterization studies have been performed on the tube's material (Deoxidized High Phosphorus (DHP) Copper - DHP Cu) to understand the effect of the deformation history on the material microstructure as well as to obtain experimental data to calibrate the multiscale ISV model. Figure 6 presents a summary of these studies: the stress-strain response, the grain structure and the deformation texture.

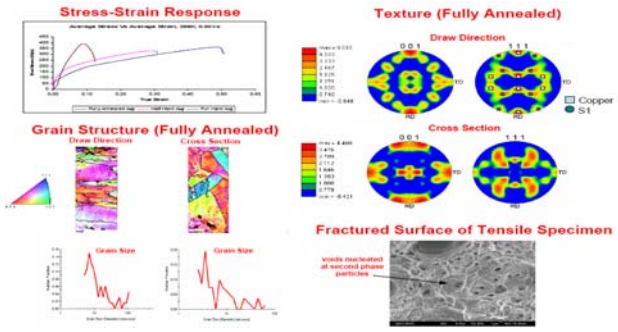

Figure 6. Mechanical and microstructural characterization of Mueller's Cu Tube.

The ISV material model (Bammann, 1990; Bammann et al. 1993, Horstemeyer et al. (2000a, 2001), based upon a hierarchical, multiscale methodology, has been calibrated with the experimental data presented above. The corresponding experimental and computed responses as well as the the geometry of the tensile specimen (physical sample and FE model) are presented in Figure 7.

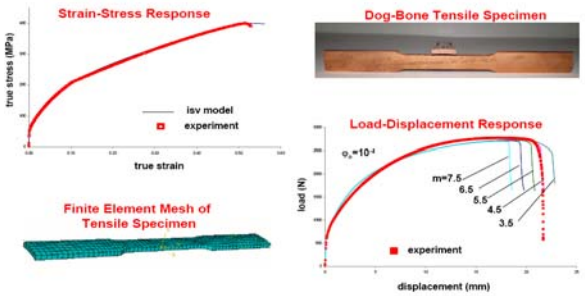

Figure 7. Calibration of the plasticity and damage parameters of the ISV model using experimental data. The geometry of the dog-bone tensile specimen is also shown.

A validation study was performed with the constructed FE model of the hydroforming process and the calibrated multiscale ISV material model. The material model was implemented in ABAQUS through a user material routine.

Figure 8 depicts the formation of the T-shape fitting during the hydroforming process as predicted by the numerical model. The process curves for the ram velocity and fluid pressure used in the simulation are shown at the top of the figure. These curves have vertical markers indicating the times at which the snapshots of the deforming tube have been extracted from the simulation, so that one can relate the progression of the forming process with the different stages (sealing, forming, coining) defined by the processing variables.

The validation of the numerical model was accomplished by comparing the material flow patterns and tube geometry between simulated and manufactured T-shape tube fittings. The experimental flow patterns were obtained from a Cu blank etched with straight lines before being hydroformed. The resulting flow patterns are presented in Figure 9 together with the predicted ones from the simulations. Clearly, the flow lines match well. The same figure also presents a comparison of the thickness profiles between the predicted and manufactured T-shape fittings. Again, the results from the FE model agree well with the experimental ones.

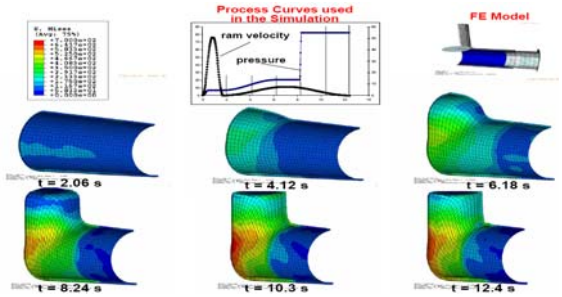

Figure 8. Snapshots showing the formation of the T-shape fitting during the hydroforming simulation.

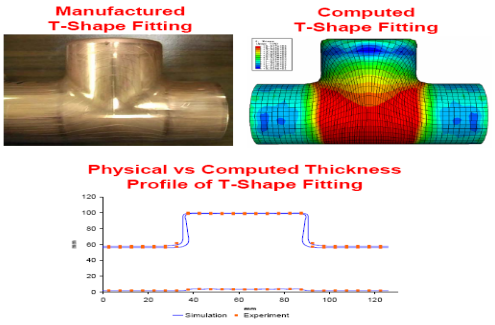

Figure 9. Comparison of flow patterns and thickness profiles between manufactured and simulated T-shape fittings.

The validated numerical model was used in a statistical study of the hydroforming process using numerical experiments designed based on a design and analysis of computer experiments (DACE) methodology. The numerical experiments have been performed in two phases: a screening analysis using a fractional factorial design and a full study employing a full factorial design. The screening study is mainly focused on computing the "main effects" of an initial set of design variables in order to rank their effect on the outcome of the process. In DACE, an outcome is typically a chosen "metric" that characterizes the response of a system (hydroforming process). Based on this preliminary ranking, one can then select a few of the most important variables to perform the full study of the process, study that involves not only main effects but also interaction effects. With this last analysis, one can then suggest recommendations regarding the main process parameters that should be carefully controlled/set to improve the outcome of the hydroforming process.

The set of design variables selected for the screening study together with their range of possible values (design space) are displayed in Figure 10. As shown in the figure, some of these variables define specific features of the velocity and pressure curves and, hence, they control the profile of the processing curves. To select the combination of parameter values to use in the numerical simulations, we have used a 1/32, two-level, fractional factorial design (sampling procedure) to build the matrix of numerical experiments (design matrix with 32 simulation runs). The main effects of these design variables have been quantified using a number of performance metrics which included measures of product quality (thickness of the Cu fitting at different locations) and mechanical rupture (von Mises stress, stress triaxiality, effective plastic strain). The computed values of the metrics have been analyzed using statistical tools widely employed in DACE approaches: main-effect plots, normal probability plots and analysis of variance (ANOVA).

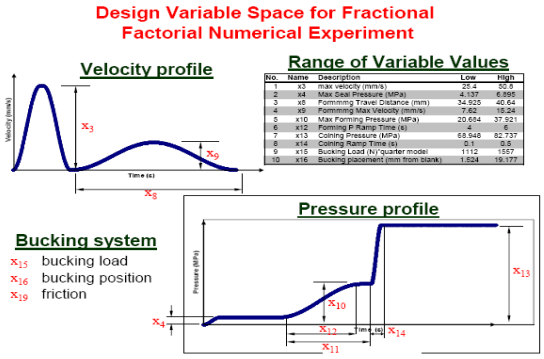

Figure 10. Design variables selected for screening study of hydroforming process.

The results of the screening study have indicated that five parameters are the most influential in the hydroforming process. These parameters are listed in Figure 11, where the column denoted "occurrences" lists the number of times the parameter shows up as an influential factor for a particular metric. At this point, discussions were held with the process experts from Mueller to get their input regarding the results of the study. These discussions have produced a reduced and modified set of design parameters which are also listed in Figure 11. Based on this, a full study has been performed using a two-level, full factorial design which involved 16 numerical experiments. The experimental matrix for this design is presented in Figure 11 as well.

Influential Design Parameters from Screening Study

Variable	Description	Occurances
x4	Maximum Sealing Pressure	2
x8	Forming Travel distance	9
x9	Forming Maximum Velocity	5
x10	Forming Pressure	13
x14	Coining Ramp Time	1

Design Parameters for Final Study

Variable	Description
x4	Maximum Sealing Pressure
x9	Forming Maximum Velocity
x10	Forming Pressure
x12	Forming Pressure Ramp Time

Design Matrix for Two-Level Full Factorial Numerical Experiment

Sim No.	1	2	3	4	5	6	7	8	9	10	11	12	13	14	15	16
x4	1	2	1	2	1	2	1	2	1	2	1	2	1	2	1	2
x9	1	1	2	2	1	1	2	2	1	1	2	2	1	1	2	2
x10	1	1	1	1	2	2	2	2	1	1	1	1	2	2	2	2
x12	1	1	1	1	1	1	1	1	2	2	2	2	2	2	2	2

1: low value of parameter, 2: high value of parameter

Figure 11. Influential design parameters used in a full numerical experiment of the hydroforming process.

The T-shape tube fitting geometries obtained from the final 16 simulation runs are presented in Figure 12. Note that the simulations predict that wrinkling of the Cu tube happens for some combinations of the design parameters. An analysis of the computed performance metrics mentioned above has also been carried out using the following statistical tools: ANOVA, normal-

probability plots, Paretto charts, main-effects plots, and two-way and three-way interaction plots. A sample of the results from this statistical study is shown in Figure 13, which depicts the analysis of the maximum value for the von Mises stress (a metric for mechanical rupture) using some of the statistical tools referred above. A main conclusion of this full-factorial numerical study is that, for the range of parameter values used, the hydroforming process is mainly driven by major interactions among the most important process parameters and, hence, these interaction effects should be considered when selecting/setting the process curves for the hydroforming process.

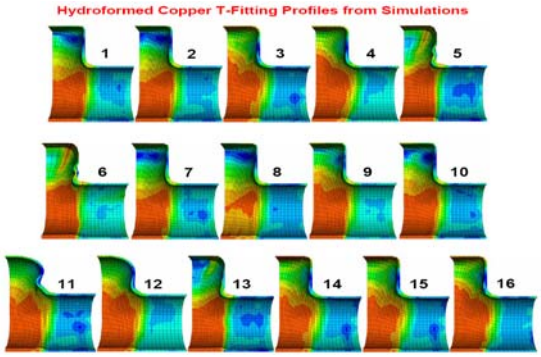

Figure 12. Simulation results from final DACE study of hydroforming process.

Based on this study, a number of suggestions have been proposed for Mueller to better control its hydroforming process and avoid typical process failures such as bursting and wrinkling. It is important to mention here that this study has also shown that using FE simulations together with a DACE methodology is a powerful tool to understand the process-product relationship of complex industrial forming processes.

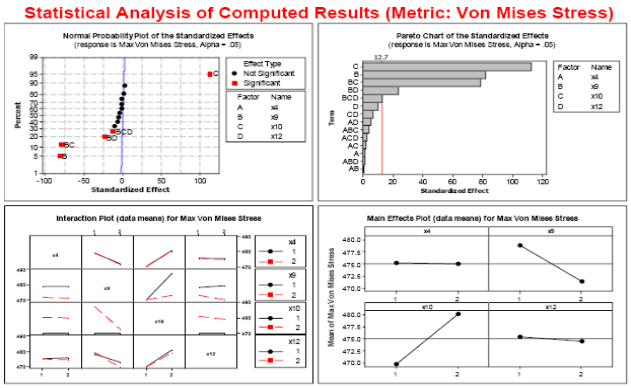

Figure 13. Statistical analysis from final DACE study: metric "von Mises stress".

Rolling History Microstructure-Property Relations of a Rolled 6022 Al Alloy

This section covers microstructure analyses and mechanical properties of 6022 Al alloy at various stages of the rolling process. The history effect reflected from these stages will provide a database for advanced material modeling. The rolling steps comprise reductions of a 6-inch slab to a 3-inch slab to a 1/8-inch sheet, an annealing process of the 1/8-inch sheet, and finally a reduction to the 1/32-inch finish-gauge sheet. The microstructural content was obtained through scanning electron microscope (SEM) analyses, optical microscopy (OM) analyses, and X-ray tomography. Research results obtained here should be useful for the improvement of manufacturability of 6022 Al-alloy closure panels applied in the automotive industry.

The 6022 Al alloy was developed by Alcoa in the late 1980's primarily for automotive closure-panel applications. The automotive body panels are fabricated using a stamping process of thin-gauge Al sheets. The 6022 Al alloy displayed enhancements in formability and hemming performance, superior surface quality, and excellent paint-bake response which are vital for performance in the stamping process. The 6022 Al alloy also displayed improved corrosion resistance over other commercially-available alloys (Kamat et al., 2002).

Experimental Procedure

The 6022 Al-alloy material was provided by Alcoa Inc. at various stages of the manufactured rolling process.

Microstructure Analysis

The strengthening of Al-Mg-Si alloys is based on a precipitation hardening process. According to Miao et. al. (Miao and Laughlin, 1999), the precipitation sequence for the 6022 Al alloy is defined as:

α (sss) $\rightarrow$ *GP* zones $\rightarrow$ needle–like β''

$\rightarrow$ rod-like β' + lath-like precipitates $\rightarrow \beta$ + Si

where α (sss) is the supersaturated solid solution. GP (Guinier-Preston) zones are generally considered spherical clusters with unknown structure. The β'' are fine, needle-shaped zones along $<100>_{Al}$ with a monoclinic structure, and β' are rod-shaped precipitates along $<100>_{Al}$ with a hexagonal crystal structure. The β are usually Mg_2Si platelets.

The microstructural analysis was conducted on material samples taken from the various stages of the manufacturing rolling process. The samples were mounted using a cold-mounting epoxy and polished using Struers automatic polishing equipment and procedures. The specimens were analyzed with a JEOL field-emission SEM with attached x-ray-electron diffraction spectroscopy (X-EDS) spectrometers and a Zeiss high-power microscope. The material matrix and second-phase precipitate compositions were determined through energy-dispersive x-ray (EDX) evaluation. X-ray scans of the material were conducted using a Phoenix dual-tube Xtome machine to determine any porosity present throughout the thickness of the material.

The SEM images and EDX evaluations of the material reveal a supersaturated solid solution matrix with second-phase particles and inclusions in the samples taken from the 6-inch to 1/8-inch hot-rolled material as seen in Figure 14. The 1/8-inch sheet is put through an annealing process where the Mg_2Si precipitates are formed as seen in Figure 15. These Mg_2Si precipitates are then flattened, as seen in Figure 16, during the cold-rolling process used to produce the final gauge thickness of the material. The X-ray scans revealed the presence of microporosity located at the center of the thickness in the 6-inch material.

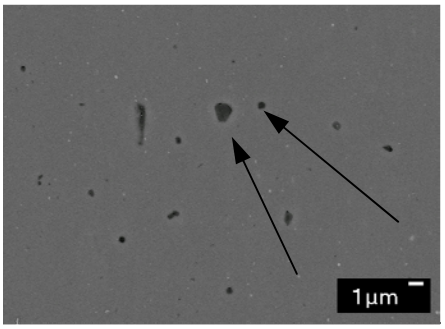

Figure 14. SEM image at 1000X magnification of a Al 6022 sample taken from the 1/8-inch sheet (before annealing) material. The black spots are Mg_2Si precipitates.

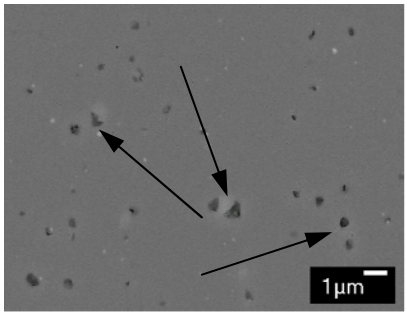

Figure 15. SEM image at 1400X magnification of a Al 6022 sample taken from the 1/8-inch sheet (after annealing) material. The increase in Mg_2Si precipitates after the annealing process can be seen.

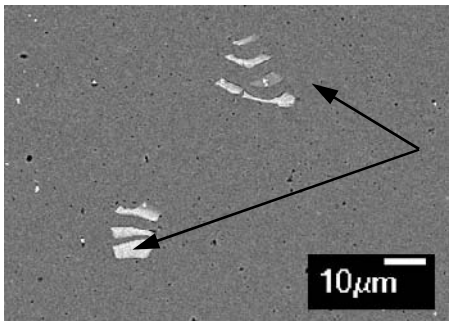

Figure 16. SEM image at 400x magnification of an Al 6022 sample taken from the 1/32-inch sheet material. The flattening of the second-phase particles can be seen as noted by the arrows.

Mechanical Testing

Mechanical tests were performed on specimens oriented in the rolling direction, long transverse direction, and short transverse direction for each stage of the manufacturing rolling process.

Tensile specimens were fabricated using a computerized numerical control (CNC) milling machine according to American Society for

Testing and Materials (ASTM) E8 subsize specimen standards. Tensile specimens were tested using an Instron 5882 electromechanical machine at ambient temperature with a constant strain rate of 0.0001 sec^{-1}. A clip-on style extensometer was used for measurement and control of the strain.

Results

The tensile test results, shown in Figure 17, of the specimens oriented in the rolling direction (L direction) showed a slight decrease in strength and ductility during the hot-rolling reduction process from the 6-inch slab to the 3-inch slab. An increase in strength and a decrease in ductility were observed in the 1/8-inch hot-rolled sheet. After the annealing process, a decrease in strength and increase in ductility were observed in the 1/8-inch sheet. An increase in strength and decrease in ductility were observed in the 1/32-inch finish-gauge sheet.

The tensile-test results, shown in Figure 18, of specimens oriented in the long transverse direction (T-direction) showed observations similar to the rolling direction results. The exception was an increase in ductility during the hot-rolling reduction process from the 6-inch slab to the 3-inch slab.

Tensile-test specimens oriented in the short transverse direction (S-direction) could only be extracted from the 6-inch slab. These tests showed similar strength values in all directions. Only slight differences in ductility were observed as shown in Figure 19. However, significant differences can be seen in the 1/32-inch sheet tensile test results in the different orientations as seen in Figure 18.

Using the BCJ (Bammann, Chiesa, and Johnson, 1996) ISV model to fit the experimental data, parameters can be found that describe the material response at the various stages of the rolling process. Figure 20 shows a comparison of the model fit using these parameters and the experimental data from the tensile tests.

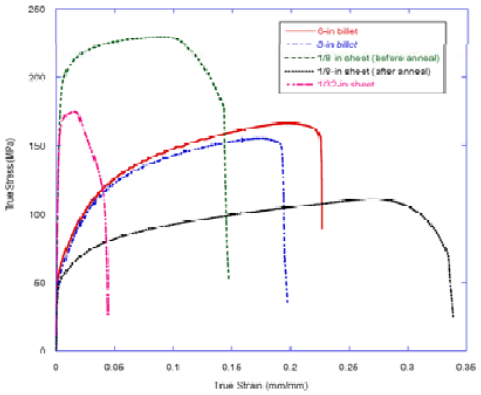

Figure 17. True-stress versus true-strain curves from tensile tests performed at ambient temperature for Al 6022 specimens taken from the various rolling stages oriented in the rolling direction (L direction).

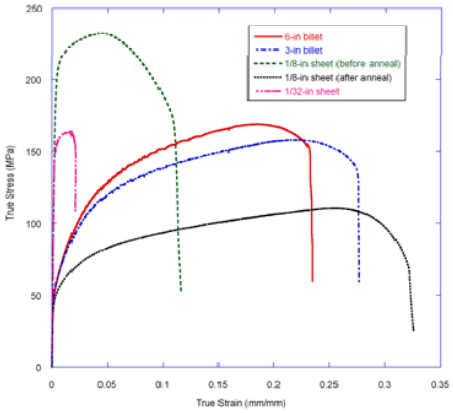

Figure 18. True-stress versus true-strain curves from tensile tests performed at ambient temperature for Al 6022 specimens taken from the various rolling stages oriented in the long transverse direction (T direction).

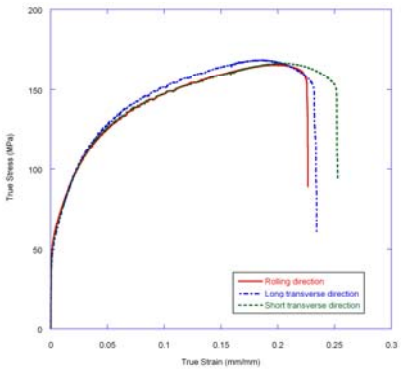

Figure 19. True-stress versus true-strain curves from tensile tests performed at ambient temperature for Al 6022 specimens taken from the 1/32-inch sheet oriented in different directions.

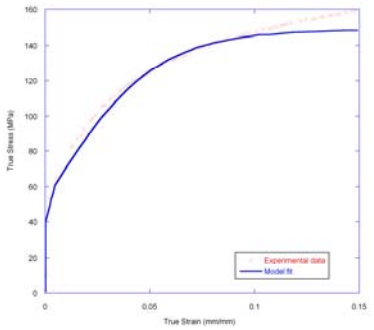

Figure 20. True-stress versus true-strain curves from tensile tests performed at ambient temperature for Al 6022 specimens taken from the 1/32-inch sheet oriented in different directions.

Summary

We investigated the material behavior of Al 6022 alloy throughout various stages of the rolling process. The preliminary structure-property relationship indicates that the mechanical properties are strongly related to the microstructural state of the material at each stage. In the initial stages of the rolling process, texturing effects are negligible. However, in the later stages texturing effects can be seen with the differences in the strength and ductility for different orientations of the specimens. For the heat-treatable 6022 Al alloy, it follows the anticipated microstructure development during anneal process.

This effort will enable us to develop a comprehensive ISV model of the material response during the rolling process.

Future Work

Further work on the grain distribution, size, and orientation gradients from the center of the bulk material to the rolling surface of the initial manufacturing stages will be investigated. Additional mechanical tests will be conducted, such as compression and torsion, at additional strain rates and temperatures. Parameters will be determined for implementation into a FE code for simulations of material responses during the various stages of the rolling manufacturing process.

Microstructural-Property Characterization of a Dodge Neon Passenger Car

Passenger-vehicle occupant safety and crashworthiness are essential attributes in today's automotive industry. In this study, a detailed FE model of a 1996 Plymouth/Dodge Neon was used (originally developed at the Federal Highway Administration/National Highway Transportation Safety Administration (FHWA/NHTSA) National Crash Analysis Center and later modified at CAVS) to perform crashworthiness simulations under different impact scenarios. Based on the initial crashworthiness simulations, the ten most energy-absorbing components were selected to develop their microstructure-property relationships. Test specimens were extracted from the as-built vehicle. Microstructural analyses were conducted to characterize grain sizes and their distribution for each component. Mechanical tests, including tension and hardness tests, were performed. Different microstructure-property relations, mechanical properties and microstructural spatial clustering were found for each component. The research objective of this work is to perform material characterizations of critical Dodge Neon components for material response refinement in crashworthiness simulations to improve occupant safety.

Introduction

Crashworthiness simulations using full-scale FE vehicle models are becoming an increasingly important part of vehicle design to decrease vehicle weight and yet increase the performance and safety under different crash scenarios. Lightweighting and safety improvement have been critical issues for both the automobile and its related manufacturing industries. According to NHTSA, there were over six million vehicle crashes in the United States in the year 2004, which claimed the lives of more than 40,000 people. A detailed FE model of a 1996 Plymouth/Dodge Neon was developed at the FHWA/NHTSA National Crash Analysis Center as part of the Partnership for a New Generation of Vehicles (PNGV) program. Crashworthiness simulations were conducted on the NHTSA FE model for different impact crash scenarios and the top ten energy-absorbing components of the

vehicle were determined. Material for the specimens was extracted from the as-built vehicle.

Microstructural analyses of the vehicle components were conducted (at MSST) to obtain the average grain size and distribution for each component. Mechanical tests were conducted. Hardness tests were performed to determine the Vickers hardness and Young's Modulus of each component. Tension tests were performed at two different strain rates at ambient temperature conditions to determine elastic-plastic responses. The results are presented in the following sections.

Experimental Procedure

The microstructural analysis was performed using the AxioVisio Grains software developed by Zeiss. The grain size and distribution were obtained using the ASTM 112-96, which defines the ASTM grain size number, G, and assigns to each G a number of grains per unit area, average grain area and average diameter. The microhardness tests were carried out using a Hysitron TriboIndenter. Nine indentations were performed in every sample using a Berkovich tip, to obtain the load-displacement curves.

The uniaxial-tension tests were performed on material extracted from the vehicle components. These tests were conducted under constant strain-rate conditions using an extensometer for feedback control. The tension tests were conducted at two different strain rates, $0.01s^{-1}$ and $0.0001s^{-1}$, on material from the front bumper, trunk lid and rear floorboard components. The $0.0001s^{-1}$ strain-rate tension tests were carried out on an Instron Model 5869 electromechanical machine using an Epsilon extensometer. The $0.01s^{-1}$ strain-rate tension tests were conducted on a hydraulic MTS Model 810 machine. Specimen width and thickness were measured before the tension tests. All of the tests were performed at ambient temperature.

From the microhardness test, the Young's modulus and yield stress values can be obtained using the following equations (Triboindenter User Manual, 2005):

$$\frac{1}{E_r} = \left(\frac{1-\upsilon^2}{E}\right)_{material} + \left(\frac{1-\upsilon^2}{E}\right)_{indenter} \quad (1)$$

$$HV = 3.03 \cdot \sigma_y \quad (2)$$

where υ is the poisson's ratio, E is the elastic modulus (E_r is the reduced elastic modulus), σ_y is the yield strength, and HV denotes the Vickers Hardness (Vickers Pyramid Number).

The yield stress was also obtained from the tension tests using the offset method in the ASTM standard. (ASTM Standards, 2000).

Results

The Dodge Neon front bumper was the most critical component in the frontal-impact crash scenarios. The microstructure of the front-bumper material can be observed in Figure 21 and Table 1 shows the chemical composition.

Table 1. Chemical composition of the front bumper material.

Fe	C	Mn	Nb	V	Al	Others
98.3	0.078	1.2	0.103	0.063	0.048	0.218

This composition indicates that the material is a microalloyed steel, specifically niobium high-strength low-alloy (HSLA) steel.

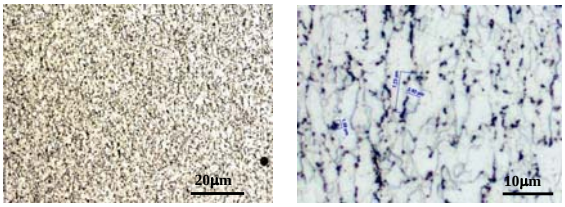

Figure 21. Photomicrographs of the front-bumper material.

All of the microstructures observed were predominantly ferritic. The samples observed presented a mixed microstructure with fine grains having an average diameter range from 2 to 7 µm, and bigger grains with an average diameter from 15 to 25 µm. The grain boundaries are irregular and the grains are elongated in the rolling direction. A darker phase, or precipitates, can be observed in the grain boundaries and some in the ferrite grains. We presumed that this phase is composed of niobium carbide. The precipitates are distributed unevenly with some grain boundaries free of precipitates.

Figure 22 shows the grain-size distribution for each sample. The grain-size mean value is G-11. Using the ASTM 112-96 standard, the mean area is 63 μm^2 and the grains per unit area at 1x is 15872 grains/mm^2. In the positions where the samples were extracted, the material displays little variation in the Vickers hardness values shown in Figure 23, indicating a homogeneous material. The mean Vickers hardness value is 265.4±14.1 HV. The mean yield point and Young's Modulus were calculated at 858.4±45.8 MPa and 181.6±20.1 GPa, respectively, using equations 1 and 2.

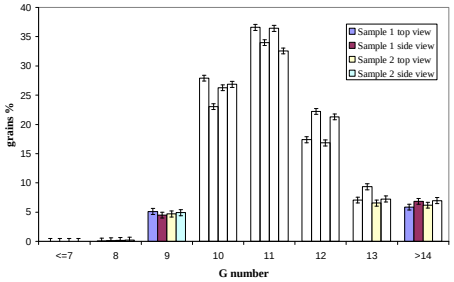

Figure 22. Grain-size distribution of the front bumper.

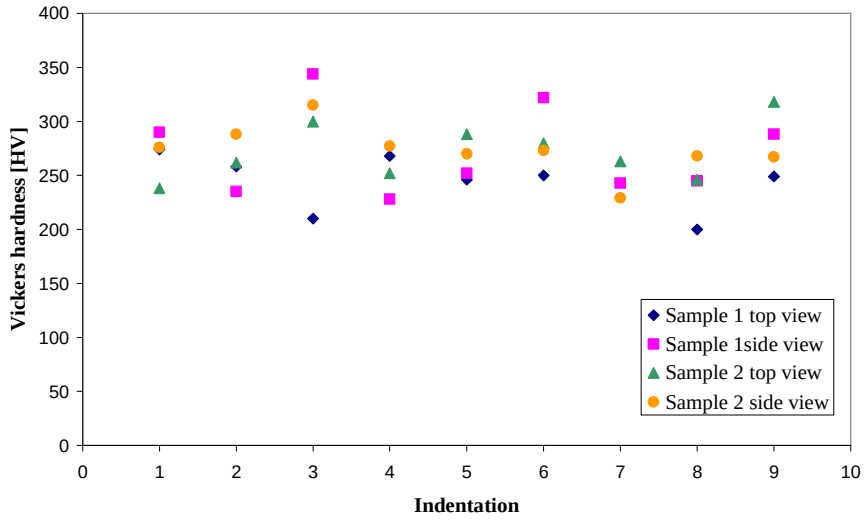

Figure 23. Vickers hardness for the front bumper.

Table 2. Front-bumper properties summary.

	Mean Values			
	Microhardness	*Tension 0.01 /s*	*Tension 0.0001 /s*	*Handbook values plain carbon steel*
Young's Modulus [GPa]	181.6±20.1	166.5±38.8	145.4±20.6	197-206
Yield Point [MPa]	858.4±45.8	511.6±192.1	486.5±193.4	206-275
Ultimate Strength [MPa]	-	601.8±13.2	579.7±39.3	340-450
Vickers Hardness [HV]	265.4±14.1	-	-	130

The summary of the properties obtained for the front-bumper material is shown in Table 2. The stress-strain curves for this material are shown in Figure 24.

We observed that the yield stress increases when the strain rate is higher. These yield-stress values are higher compared to the average values of plain-carbon steels. The Young's modulus is close to the average value for most steels.

Summary

Uncertainty related to microstructure was quantified based on the microstructure-characterization techniques. Different microstructure-property relations for each component were found.

Differences in the microstructural spatial clustering were observed. The chemical composition and optical microscope images of each component show that the material is different for every vehicle part. Therefore, the use of similar stress-strain-stress curves and material properties on a model used in crashworthiness simulations, can affect the results obtained.

Strain-rate dependency was observed in the stress-strain curves on each component tested. This dependence can be noticed in the yield stress and ultimate stress values, since they are lower for the 0.0001/s strain rate for every component.

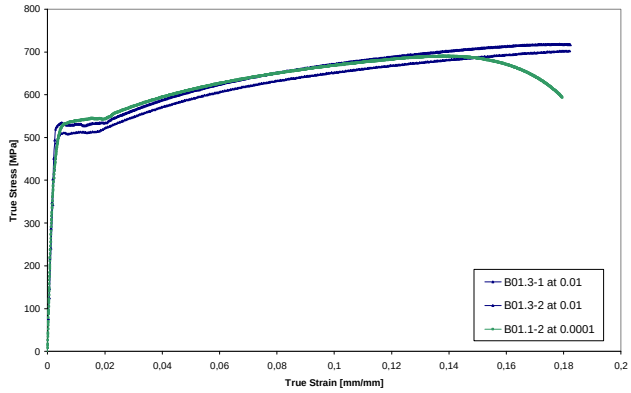

Figure 24. True-stress/true-strain curves of the front bumper.

More vehicle components were determined to be critical during the crash scenarios. To obtain better and more accurate results in crash simulations and to improve passenger safety, the actual material properties of these components should be used in the model. The microstructure characterization of these components is still being determined.

The Associated Sensitivities and Uncertainties of a Multiscale ISV Model with Damage Evolution Arising from Structure-Property Relations

In this section, we analyze the effects of uncertainties pertaining to structure-property relations of an ISV plasticity-damage model that predicts failure. In particular, the microstructural spatial variabilities, the constitutive model-parameter sensitivities, and boundary-condition uncertainties on the damage evolution and final failure using both cast- and wrought-Al alloys are examined. The cast material used in this study is A356 and wrought is Al 6022. The uncertainty analyses are performed using traditional methods like propagation rule and Monte Carlo (MC) techniques and then compared with uncertainty analysis performed by blending a dimension reduction (DR) method and a distribution fitting technique. We first calculate the first four statistical moments of damage using a DR method that reduces the multidimensional integrals (needed in calculating the statistical moments) to a series of single-dimension integrals. Then, we estimate the probability distribution of damage using an extended generalized lambda distribution. We investigated the efficiency and accuracy of this uncertainty analysis methodology on an engineering problem and found very good agreement between the uncertainty predictions of this methodology between different techniques. Finally, we applied the uncertainty analysis methodology for predicting the damage uncertainty. The scatter in damage (that is, the coefficient of variation of damage) increased as the strain increased, even though the uncertainties in the material-plasticity and microstructure parameters remain constant (Figure 30). For A356, the mathematical sensitivity analysis related to damage uncertainty is consistent with the physical nature of the damage progression. At the very beginning, the initial porosity and void nucleation are shown to drive the damage evolution. Then, void coalescence becomes the dominant mechanism. Near failure, one of the macroscale structural properties (fracture toughness)

dominates the damage-evolution process as illustrated by the sensitivity/uncertainty analysis.

Introduction

Improving structural safety requires not only understanding the history of a material through its manufacturing process and in-service life, but also assessing the correlation between the various physical scales present, from the atomic level interactions to the microstructural composition and to the macroscale behavior. With the help of such multiscale material models, it will be possible to relate structural responses of interest such as stress, strain, and toughness, to key material parameters at each length scale, such as particle size, interfacial strength and spacing. The works on multiscale modeling include those of Horstemeyer et al. (2000b, 2001, 2003; Ganapathysubramanian and Zabaras (2004), and Shilkrot et al. (2004). For a summary of recent progress in multiscale material modeling and simulations, the reader is referred to Graham-Brady et al. (2006).

In this work, we utilize the damage-evolution model developed by one of the authors (Horstemeyer et al., 2000a; 2000c; 2001) since we had good access to experimental and computational details. Horstemeyer (2001) has employed successfully a multiscale analysis for automotive structural components made of A356 cast Al. More recently, Horstemeyer et al. (2005) investigated the effect of variability in microstructures and the boundary conditions that characterize the damage evolution using first-order Taylor series (FOTS) uncertainty analysis. In particular, void-nucleation, void-growth, and void-coalescence equations were evaluated and quantified in terms of sensitivity and uncertainty of various parameters in the constitutive equations. However, uncertainty analysis using a FOTS expansion is amenable to errors, especially for nonlinear response functions (like damage). Therefore, the current work extends the work of Horstemeyer et al. (2005) in that we perform a more accurate uncertainty analysis using a DR technique proposed by Rahman and Xu (2004).

In general, modeling uncertainty exists due to numerical accuracy and simplifying assumptions and to variations in design conditions, input parameters, and other components of a model. Most of the literature on modeling uncertainty has addressed the effect of input-parameter uncertainty. Some recent work has addressed the area of verification and validation (V&V) in an attempt to estimate the other components of model uncertainty. The basis for modeling uncertainty was adapted from the widely-used experimental uncertainty analysis. The experimental uncertainty-analysis references for this study all use the same basic methodology. The worldwide standard for this experimental uncertainty analysis is authored by the International Organization for Standardization (ISO, (1995)).

In the traditional form of uncertainty analyses we incorporated propagation rule (FOTS expansion) and MC techniques. In propagation technique, the uncertainty in damage is given as (Coleman and Steele (1999))

$$U_\phi = \sqrt{\sum_{i=1}^{j}\left[\left(\frac{d\phi}{d\eta}\frac{\partial\eta}{\partial x_i}+\frac{d\phi}{dV_v}\frac{\partial V_v}{\partial x_i}+\frac{d\phi}{dC}\frac{\partial C}{\partial x_i}\right)U_{x_i}\right]^2} \quad (3)$$

where x_i are boundary condition and microstructure parameters, U_{x_i} is the uncertainty for each parameter, and $\eta, V_v, and\ C$ are nucleation, void-growth and coalescence, respectively. To measure the influences of different parameters, two main uncertainty definitions were used:

- Uncertainty magnification factor (UMF_i)

$$UMF_i = \frac{x_i}{\phi}\frac{\partial\varphi}{\partial x_i} \quad (4)$$

- Uncertainty percentage contribution (UPC_i)

$$UPC_i = \left(\left(\frac{x_i}{\phi}\frac{\partial\varphi}{\partial x_i}\right)^2\left(\frac{U_{x_i}}{x_i}\right)^2 \Big/ \frac{U_\phi{}^2}{\phi}\right)100 \quad (5)$$

The overall procedure of uncertainty analysis using uncertainty analysis using dimension reduction and distribution fitting (UDRDF) can be outlined as depicted in Figure 25. First, the physically-motivated damage calculations are performed at some selected points in the random variable space. Next, the first four statistical moments of the performance function are estimated using DR. Then, the probability distribution of the damage is approximated with EGLD (extended generalized lambda distribution). The accuracy of this analysis

is highly dependent on the accuracies of moment estimation and distribution correlation.

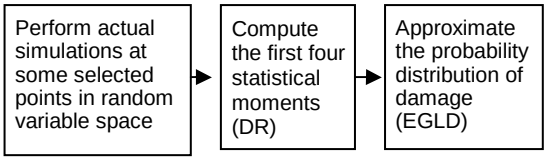

Figure 25. Procedure for UDRDF.

The main contribution of this report is to incorporate different uncertainty analysis techniques in the context of constitutive modeling to illustrate the effects of microstructural variations, along with uncertainties in the loading and boundary conditions, to assess the uncertainty in damage, which is calculated using a multiscale ISV material model. In addition, we aim to quantify the influence of uncertainty of various parameters in the constitutive equations.

Multiscale Microstructure-Property Relationships

The multiscale microstructure-property relationship modeling framework (Horstemeyer (2001), Bammann et al. (1993)) used here accounts for stress-state-dependent damage evolution. The pertinent equations in this model are denoted by the rate of change of the observable (temperature, stress state, and rate of deformation) and the ISVs. For the sake of clarity, a listing of these equations and their relation to the multiscale analysis within the context of FE methodology is briefly described here with additional details provided in (Horstemeyer (2001)).

The frame-indifferent co-rotational rate of the Cauchy stress, $\overset{\circ}{\underline{\sigma}}$, is expressed as

$$\overset{\circ}{\underline{\sigma}} = \lambda(1-\phi)tr\left(\underline{D}^e\right)\underline{I} + 2\mu(1-\phi)\underline{D}^e - \left(\frac{\dot{\phi}}{1-\phi}\right)\underline{\sigma} \qquad (6)$$

where $\underline{\sigma}$ is the Cauchy stress, ϕ is the damage fraction of material within a continuum element (an ISV that represents the damage state) with $\dot{\phi}$ representing its material time derivative, λ and μ are the Lamé elastic constants, $\underline{D}^e$ is the elastic rate of deformation tensor, and $\underline{I}$ is the second-order identity tensor. The underscore symbol in all the equations indicates a second-rank tensor.

The plastic rate of deformation tensor or the deviatoric inelastic flow rule, $\underline{D}^p$, encompasses the regimes of creep and plasticity and is determined as

$$\underline{D}^p = f(T)\sinh\left\{\frac{\left\|\underline{\sigma}'-\underline{\alpha}\right\| - \left[R+Y(T)\right](1-\phi)}{V(T)(1-\phi)}\right\}\frac{\underline{\sigma}'-\underline{\alpha}}{\left\|\underline{\sigma}'-\underline{\alpha}\right\|} \qquad (7)$$

where $\underline{\sigma}'$ is the deviatoric part of stress tensor, T is temperature in Kelvin, $\underline{\alpha}$ is the kinematic hardening (an ISV reflecting the effect of anisotropic dislocation density), and R is the isotropic hardening (an ISV reflecting the effect of global dislocation density). The function $V(T)$ determines the magnitude of rate dependence on yielding, $f(T)$ determines when the rate dependence affects initial yielding, and $Y(T)$ is the rate-independent yield stress. Functions $V(T)$, $Y(T)$, and $f(T)$ are related to yielding with Arrhenius-type temperature dependence and are given as:

$$V(T) = C_1 e^{\left(C2/T\right)};\ Y(T) = C_3 e^{\left(C4/T\right)};\ f(T) = C_5 e^{\left(C6/T\right)} \qquad (8)$$

where C_1 through C_6 are the yield-stress-related material parameters that are obtained from isothermal compression tests with variations in temperature and strain rate.

The co-rotational rate of the kinematic hardening, $\overset{o}{\underline{\alpha}}$, and the material time derivative of isotropic hardening, $\dot{R}$, are expressed in a hardening-recovery format as

$$\overset{o}{\underline{\alpha}} = \left\{h(T)\underline{D}^p - \left[\sqrt{\frac{2}{3}}r_d(T)\left\|\underline{D}^p\right\| + r_s(T)\right]\left\|\underline{\alpha}\right\|\underline{\alpha}\right\}\left[\frac{DCS_0}{DCS}\right]^z \qquad (9)$$

$$\dot{R} = \left\{H(T)\underline{D}^p - \left[\sqrt{\frac{2}{3}}R_d(T)\left\|\underline{D}^p\right\| + R_s(T)\right]R^2\right\}\left[\frac{DCS_0}{DCS}\right]^z \qquad (10)$$

where DCS_0, DCS, and z parameters capture the microstructure effect of grain size. The dislocation populations and morphology within crystallographic materials exhibit two types of recovery. In Eqs. 9 and 10, $r_d(T)$ and $R_d(T)$ are scalar functions of temperature that describe

dynamic recovery, $r_s(T)$ and $R_s(T)$ are scalar functions that describe thermal (static) recovery, whereas $h(T)$ and $H(T)$ represent anisotropic and isotropic hardening modulus, respectively. These functions are calculated as

$$r_d(T)=C_7\left[1+C_a\left(\frac{4}{27}-\frac{J_3'^2}{J_2'^3}\right)-C_b\left(\frac{J_3'}{J_2'}\right)^{3/2}\right]e^{\left(-C_8/T\right)},$$
$$R_d(T)=C_{13}\left[1+C_a\left(\frac{4}{27}-\frac{J_3'^2}{J_2'^3}\right)-C_b\left(\frac{J_3'}{J_2'}\right)^{3/2}\right]e^{\left(-C_{14}/T\right)} \quad (11)$$

$$r_s(T)=C_{11}e^{\left(-C_{12}/T\right)},\quad R_s(T)=C_{17}e^{\left(-C_{18}/T\right)} \quad (12)$$

$$h(T)=C_9\left[1+C_a\left(\frac{4}{27}-\frac{J_3'^2}{J_2'^3}\right)+C_b\left(\frac{J_3'}{J_2'}\right)^{3/2}\right]e^{\left(-C_8/T\right)}-C_{10}T,$$
$$H(T)=C_{15}\left[1+C_{22}\left(\frac{4}{27}-\frac{J_3'^2}{J_2'^3}\right)+C_b\left(\frac{J_3'}{J_2'}\right)^{3/2}\right]e^{\left(-C_8/T\right)}-C_{16}T \quad (13)$$

where $J_2'=\frac{1}{2}\left(\underline{\sigma}'-\underline{\alpha}\right)^2$, $J_3'=\frac{1}{3}\left(\underline{\sigma}'-\underline{\alpha}\right)^3$, C_7 through C_{12} are the material-plasticity parameters related to kinematic hardening and recovery terms, C_{13} through C_{18} are the material-plasticity parameters related to isotropic hardening and recovery terms, whereas C_a and C_b are the material plasticity parameters related to dynamic recovery and anisotropic hardening terms, respectively. Constants C_1 through C_{18} are determined from macroscale experiments at different temperatures and strain rates.

The two components of damage-progression mechanism are void nucleation and growth from silicon particles and pores. In this regard, the material time derivative of damage, $\dot{\phi}$, is expressed as

$$\dot{\phi}=\left(\dot{\phi}_{particles}+\dot{\phi}_{pores}\right)c+\left(\phi_{particles}+\phi_{pores}\right)\dot{c} \quad (14)$$

where $\phi_{particles}$ represents void growth from particle debonding and fracture, ϕ_{pores} represents void growth from pores, with $\dot{\phi}_{particles}$ and $\dot{\phi}_{pores}$ representing their respective time derivatives; parameter *c* represents the void coalescence that is indicative of pore-pore and silicon (Si)-pore interactions with $\dot{c}$ as its time derivative. The particle- and pore-based void growth rate and the void-coalescence rate equations are given as

$$\dot{\phi}_{particles}=\dot{\eta}v+\eta\dot{v} \quad (15)$$

$$\dot{\phi}_{pores}=\left[\frac{1}{(1-\phi_{pores})^m}-(1-\phi_{pores})\right]\sinh\left[\frac{2\left(2^{V(T)/Y(T)}-1\right)}{\left(2^{V(T)/Y(T)}+1\right)}\frac{\sigma_H}{\sigma_{vm}}\right]\left\|\underline{D}^p\right\| \quad (16)$$

$$\dot{c}=\left[Cd_1+Cd_2\left(\eta\dot{v}+\dot{\eta}v\right)\right]e^{(C_{CT}T)}\left(DCS_0/DCS\right)^z \quad (17)$$

where *v* is the void growth, η is the void nucleation, whereas σ_H and σ_{vm} are the hydrostatic and von Mises stresses, respectively. The parameters Cd_1 and Cd_2 are related to first and second normalized nearest-neighbor distance parameters, respectively, and C_{CT} is the void-coalescence temperature-dependent parameter. The void nucleation rate and void growth rate are given as

$$\dot{\eta}=\left\|\underline{D}^p\right\|\frac{C_{coeff}d^{1/2}}{K_{IC}f^{1/3}}\eta\left[a\left(\frac{4}{27}-\frac{J_3^{\,2}}{J_2^{\,3}}\right)+b\frac{J_3}{J_2^{3/2}}+c\left\|\frac{I_1}{\sqrt{J_2}}\right\|\right]e^{\left(-C_{\eta T}/T\right)} \quad (18)$$

$$\dot{v}=\frac{\sqrt{3}R_0}{2(1-m)}\left[\sinh\left(\sqrt{3}(1-m)\frac{\sqrt{2}I_1}{3\sqrt{J_2}}\right)\right]\left\|\underline{D}^P\right\| \quad (19)$$

where C_{coeff} is a material constant that scales the response as a function of initial conditions, *d* is the particle size, K_{IC} is the fracture toughness, *f* is the volume fraction of second-phase particles, $C_{\eta T}$ is the void-nucleation temperature-dependent parameter, I_1, J_2, and J_3 are the independent stress invariants, *m* is the void growth constant, R_0 is the initial void radius, whereas material constants *a*, *b*, and *c* are the void-nucleation constants that are determined from different stress states (i.e., *a* is found from a torsion test while *b* and *c* are determined from tension and compression tests, with all three having units of stress).

The time integral form of Eq. (14) is used as damage and, along with von Mises stress, represents the failure responses of interest. Based on this ISV model, failure is assumed to occur when $\phi\rightarrow 1.0$ within a finite element. For all practical purposes, material failure can be assumed at a much smaller value (percolation limit) of ϕ as damage increases very rapidly to 1.0 shortly after ϕ reaches a small percentage. The mechanical properties of a material depend upon the amount and type of microdefects within its structure. Deformation changes these microdefects and, when the number of microdefects accumulates, damage is said to have grown. By including

damage state ϕ as an ISV, different forms of damage rules can be incorporated easily into the constitutive framework.
In summary, $\underset{\sim}{\alpha}$, R, $\underset{\sim}{\sigma}$, ϕ, c, v, and η in Eqs. 6 through 19 represent the ISVs in this multiscale material model.

Material Microstructure Characterizations and Their Uncertainties

The microstructure of a typical metallic material contains a large number of microdefects such as microcracks, dislocations, pores, and particles. Some of these defects are induced during the manufacturing process and are present before the material is subjected to mechanical loads and thermal fields. In general, these defects are small and are distributed throughout most of the volume.

We are focusing on cast and wrought Al alloys. In the cast A356-T6 Al alloy, the microstructure of this material consists of the primary (Al–1.6wt.%Si) and eutectic (Al–12.6wt.%Si) phases. In the eutectic regions, large Si particles and clusters form a dendritic substructure while the Si remains solutionized in the primary phase. The microstructural alterations have a strong influence on the monotonic mechanical properties of Al castings through changes in void nucleation, growth, and coalescence characteristics.
An optical microscope image of the cast Al alloy, as shown in Figure 26, suggests that the material is more isotropic in nature. The secondary constituent particles within the matrix range from 3 to 6 μm, with the Si particles ranging from 3 to 5 μm, with an average size of 4 μm and particle volume fraction of approximately 7% (5.25% to 8.75%).

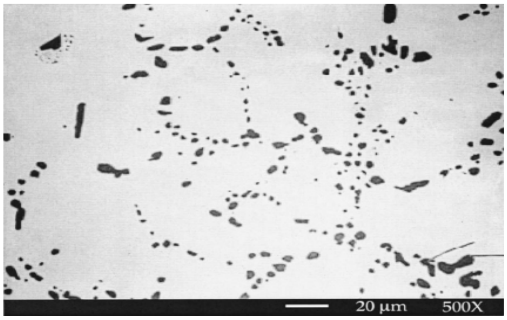

Figure 26. Optical micrograph A356 cast Al alloy which shows second-phase particles.

The microstructural analysis was conducted on a material sample taken at 6*in* slab-thickness stage of the manufacturing rolling process, as shown in Figure 27, using EBSD and image analyses software, and suggests that the material is more anisotropic in nature.

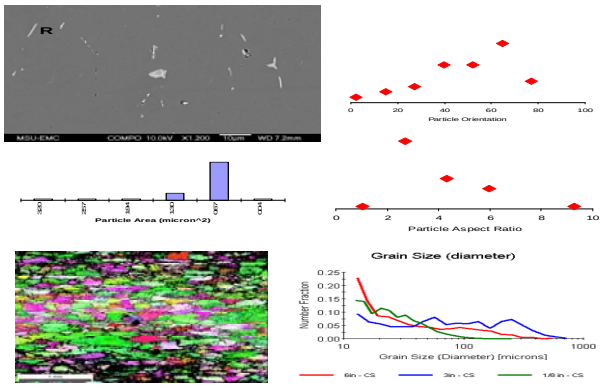

Figure 27. Microstructure clustering of wrought Al 6022 (SEM and electron backscatter diffraction (EBSD), experimental microstructure uncertainty quantification).

In this study for wrought Al alloy, we consider various stages of the rolling process, to understand the influences of manufacturing history and their subsequent effects on uncertainty analysis. (see Figure 28).

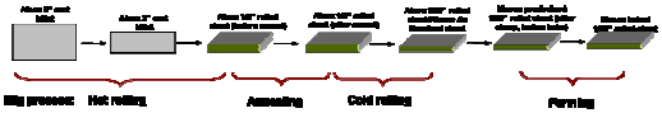

Figure 28. Various rolling stages of wrought 6022 Al alloy to quantify manufacturing history effect.

Recently, Horstemeyer et al. (2005) investigated the effect of variability in microstructures and the boundary conditions that characterize the damage evolution using uncertainty-analysis methodology. In particular, void-nucleation, void-growth, and void-coalescence equations were evaluated and quantified in terms of sensitivity and uncertainty of various parameters in the constitutive equations. They found that a 1% uncertainty in the microstructural and boundary-condition parameters results in 16% uncertainty in damage near failure, 5% uncertainty in failure strain, and 13% uncertainty in failure stress, thereby revealing the need for incorporating uncertainties in the design process when multiscale material model is used.

Table 3a. Microstructure-property (elastic-plastic) model constants for A356-T6.

ID #	Constants (Units)	Mean	ID #	Constants (Units)	Mean
1	G (MPa)	25920	13	C_{10} (°K)	10.94
2	A	1.0	14	C_{11} (sec/MPa)	0.01369
3	K (MPa)	67630	15	C_{12} (°K)	2000
-	B	0.0	16	C_{13} (1/MPa)	0.0000165
4	melt temp (°K)	5556	17	C_{14} (°K)	-1000
5	C_1 (MPa)	53.09	18	C_{15} (MPa)	2818
6	C_2 (°K)	945.3	19	C_{16} (°K)	4.622
7	C_3 (MPa)	155.9	-	C_{17} (sec/MPa)	0.0
8	C_4 (°K)	110.5	20	C_{18} (°K)	235.4
9	C_5 (1/MPa)	0.00001	21	C_a	-7.0
-	C_6 (°K)	0.0	22	C_b	-0.3776
10	C_7 (1/MPa)	0.00087	23	init.temp (°K) heat gen.	297
11	C_8 (°K)	-1877	-	Coeff.	0.0
12	C_9 (MPa)	4820			

Uncertainties in the microstructure-property relationships and multiscale ISV material model are incorporated. The effect of variability in microstructures and boundary conditions that characterize the damage evolution is investigated using uncertainty-analysis methodology. A nonlinear regression algorithm developed previously (Horstemeyer (2001)), was used to fit the plasticity model constants for both wrought and cast Al alloys (the A356-T6 Al alloy, as shown in Tables 3a and 3b). The experimental uncertainty, U_E, is calculated based on systematic and random uncertainties in the measured quantities such as force, strain, and specimen sizes (Eqns. 19 and 20).

$$U_E = \sqrt{U_r^2 + U_s^2} \tag{19}$$

where U_r is random uncertainty and U_s is systematic uncertainty.

The random uncertainty, U_r, in experimentally measured quantities, r_i (force and strain), for M different tests is given by

$$U_r = 2\sqrt{\frac{1}{M-1}\sum_{i=1}^{M}(r_i - r_{i\,mean})^2} \tag{20}$$

where r_{imean} is mean of experimentally-measured quantities (force and stain).

The systematic uncertainty in experimentally measured quantities, r_i (force and strain), for M different tests is given by

$$U_s = r_i\sqrt{U_L^2 + U_{daq}^2} \tag{21}$$

where U_L is uncertainty in load cell or extensometer or strain gauges and U_{daq} is uncertainty in data acquisition.

Quantitative fractographic measurements were used to quantify the variability in microstructure spatial clustering, as shown in Figure 27. A typical optical montage used in quantitative fractographic measurement is shown in Figure 26. The experimental uncertainties related to stress-strain responses are propagated through model correlation routine using propagation law (Eqns. 19 to 21) to predict uncertainty related to material-plasticity parameters as defined by Eqns. 6 to 11.

Table 3b. Microstructure-property (damage) model constants for A356-T6 Al alloys.

ID #	Constants (Units)	Mean
24	M	0.3
25	R_o (mm)	0.0002
26	A	615369
27	B	58630
28	C	30011
29	C_{coeff}	90.6
30	K_{ic} MPa(m$^{1/2}$)	17.3
31	d (mm)	0.000004
32	F	0.07
33	cd1	1.0
-	cd2	0.0
34	DCS0 (mm)	20
35	DCS (mm)	20
36	Z	0.0509
37	initial void volume fraction	0.0001
38	$C_{\eta T}$	0.6
-	C_{CT}	0.0

Uncertainty Analysis of Damage Evolution

In this section, we first apply the DR+EGLD uncertainty-analysis methodology to characterize the uncertainty in damage at different strain values for cast Al alloy. Then, we present a sensitivity and uncertainty analysis of damage related to different input parameters.

We consider uniaxial tensile loading of an A356 Al alloy at strain rate of 10^{-3} 1/sec. The probability distributions of the damage (integration of Eq. 14) at different part of the strain-damage response (see

Figure 29) are provided in Figure 30. The scatter of damage (the coefficient of variation of the damage, C_ϕ) increases along with the mean value of the damage as the strain value increases. The comparison of the probability distribution functions (PDFs) obtained through DR+EGLD and MC simulations (MCS) of sample size 10,000 are also shown in Figure 30, indicating a good agreement between the results of DR+EGLD and MCS considering these analyses were performed independently.

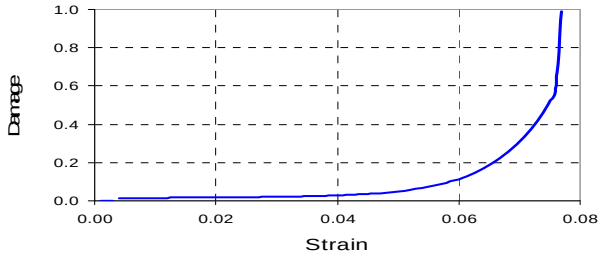

Figure 29. Strain versus damage curve for A356 Al alloy.

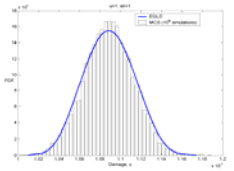

(a) strain = 0.001; C_ϕ = 0.022

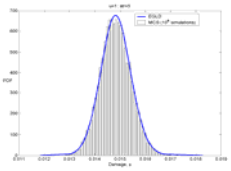

(b) strain = 0.005; C_ϕ = 0.040

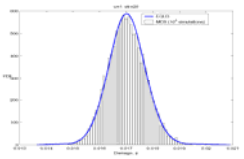

(c) strain = 0.02; Cϕ = 0.040

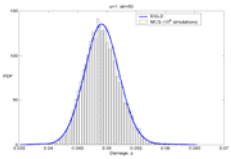

(d) strain = 0.05; C_ϕ = 0.061

Figure 30. PDFs of damage at different applied strain levels (0.001, 0.005, 0.02, and 0.05) obtained through DR+EGLD and MCSs (with sample size of 10,000).

We also compare uncertainty-analysis results of DR with FOTS uncertainty analysis results. Table 4 shows that the DR uncertainty predictions are better (1% difference at 5% strain) than FOTS uncertainty predictions (4% difference at 5% strain) when compared to MCSs (with sample size of 10,000).

Table 4. Uncertainty analysis results obtained through FOTS expansion, DR (with 4N+1 points), and MCS.

	Standard deviation of damage			
	Strain = 0.001	**Strain = 0.005**	**Strain = 0.02**	**Strain = 0.05**
FOTS	2.43×10^{-7}	6.00×10^{-4}	7.29×10^{-4}	3.09×10^{-3}
DR	2.43×10^{-7}	5.92×10^{-4}	6.93×10^{-4}	3.00×10^{-3}
MCS (10^4 simulations)	2.43×10^{-7}	5.98×10^{-4}	6.87×10^{-4}	2.97×10^{-3}

Results

Uncertainty Characterization of Wrought Al Alloy

In this section, we apply uncertainty analysis methodology to characterize the uncertainty in various rolling stages of manufacturing process. Figure 31 shows comparisons between experimental data to the model along the longitudinal direction for various rolling stages. The uncertainties in experimental data were calculated using Eqs. 19 to 21.

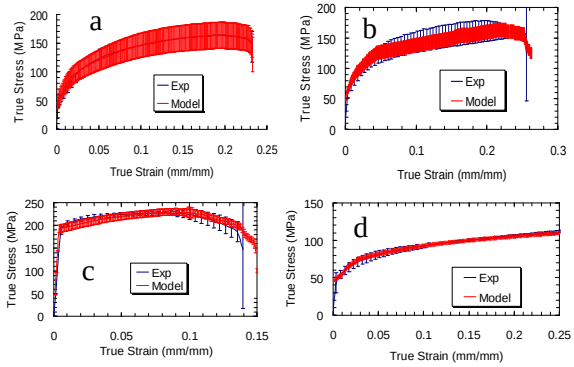

Figure 31. Comparison between experiment and model for a) 6-in. rolled sheet, b) 3-in rolled sheet, c) 1/8 in before annealing, and d) 1/8 in after annealing.

Experimental uncertainties were then propagated through a model correlation routine to estimate uncertainty in model. Figure 31 shows good comparison between model and experimental uncertainties for various rolling stages. The variations of uncertainty from one stage to another were due to variations in microstructural clustering. These results indicate the physical nature of uncertainty analyses, which are

associated with material history and inherent heterogeneities.

Sensitivity of Uncertainty of Damage at Different Strain Values Using the Cast Al Alloy.

In this section we calculate the sensitivity of uncertainty of damage to multiscale material parameters. We measure the sensitivity of damage, S_i, to an input random variable, X_i, by using

$$S_i = \frac{\partial C_\phi}{\partial C_i}\frac{C_i}{C_\phi} \qquad (22)$$

where C_i is the coefficient of variation of X_i. Sensitivities of uncertainty of damage to the uncertainties of the multiscale material parameters are depicted in Figure 32. For instance, Figure 32 (a) shows that, at the very beginning of the damage evolution, the initial radius of spherical void, d, (31st random variable) and nucleation coefficient (35th random variable) are the most influential parameters. Figure 32 (b-c), on the other hand, shows that, as damage progresses, the initial temperature (28th random variable), coalescence temperature dependence term (46th random variable), coalescence factor cd1 (39th random variable) and initial void volume fraction (44th random variable) are more important. Finally, Figure 32 (d) displays the effect of parameters on the last stages of damage progression. We see that the most influential terms can be ordered according to their importance as the fracture toughness (36th random variable), initial temperature (28th random variable) and coalescence temperature dependence (46th random variable), respectively.

The sensitivity plots in Figure 32 are also consistent with the physics of the damage progression. At the very beginning, the void nucleates and grows. Then, voids combine with each other and coalescence becomes the main driver. Near failure, macroscopic properties such as fracture toughness, K_{IC}, determines the damage evolution process.

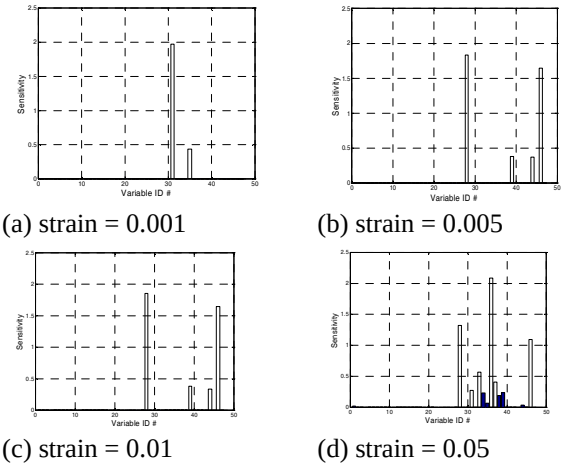

(a) strain = 0.001 (b) strain = 0.005

(c) strain = 0.01 (d) strain = 0.05

Figure 32. Sensitivity of uncertainty of damage to the uncertainties of the multiscale material parameters.

Summary

The specific conclusions are:

1. The scatter in damage (that is, the coefficient of variation of damage) increases as the strain values increase even though the uncertainties in the input variables remain fixed.
2. The sensitivities of the uncertainty of damage to the uncertainties of the input random variables were found to be dependent on the strain values. As the strain value changed (that is, as the damage evolved), the importance of the random variables changed. This correlates exactly with the physical basis of the damage formulation.
3. As such, the sensitivities were found to be consistent with the physics of the damage progression. At the very beginning, the void nucleation properties drive the damage evolution. Then, voids combine with each other and coalescence becomes the main driver during the intermediate and later stages of deformation. At final fracture, macroscopic properties such as fracture toughness, K_{IC}, became dominant.
4. We compared the uncertainty-analysis results obtained through FOTS expansion and DR with those of the MCS and found that DR uncertainty predictions were better than FOTS-series predictions.

Presentations/Publications/Patents

1. Hammi, Y., Horstemeyer, M.F., "A Physically Motivated Anisotropic Tensorial Representation of Damage with Separate Functions for Void Nucleation, Growth, and Coalescence," Int. J. Plast., Vol. 23, pp. 1641-1678, 2007.
2. Querin, J.A., Schneider, J.A., Horstemeyer, M.F., "Analysis of micro void formation at grain boundary triple points in monotonically strained AA6022-T43 sheet metal," Materials Science and Engineering A, v 463, n 1-2, p 101-106, 2007.
3. Potirniche, G., Horstemeyer, M.F., Ling, X.W., "An internal state variable damage model in crystal plasticity," Mechanics of Materials, v 39, n 10, p 941-952, 2007.
4. Jordon, J.B., Horstemeyer, M.F., Solanki, K., Xue, Y., "Damage and stress state influence on the Bauschinger effect in aluminum alloys", Mechanics of Material, Vol. 39, pp. 920-931, 2007.
5. Anurag, S., Guo, Y., Horstemeyer, M.F., "The Effect of Materials Testing Mode on Dynamic Mechanical Behavior Modeling and Hard Machining Simulation," Proc. 2007 Int. Manufacturing Science and Engineering Conference, MSEC2007-31087, Oct 2007, Atlanta, GA.
6. Solanki, K, Horstemeyer, M.F., "A Physically Motivated Uncertainty-Based Higher Order Plasticity and Damage Model," MCMAT2007-30120, ASME Applied Mechanics and Materials Conference, University of Texas at Austin, June 3-7, 2007.
7. Horstemeyer, M.F., Solanki, K., "Internal State Variable Modeling of Structure-Property Relationships in Deformed Microstructures," The Minerals, Metals, and Materials Society, 2007 TMS Annual Meeting & Exhibition, Orlando, Florida, 25 Feb - 1 March 2007.

References

1. Agnew, S. R., Yoo, M. H., and Tome, C. N. (2001) "Application of texture simulation to understanding mechanical behavior of Mg and solid solution alloys containing Li or Y", Acta. Mater., 49, 4277-4289.
2. ASTM Standards, "Section 3: Metals Test Methods and Analytical Procedures", Vol. 03.01, American Society of Testing and Materials, West Conshohocken, PA, 2000.
3. Bammann, D. J., (1990), "Modeling Temperature and Strain Rate Dependent Large Deformation of Metals," Applied Mechanics Reviews, Vol. 43, No. 5, S312-S319.
4. Bammann, D. J., Chiesa, M. L., Horstemeyer, M. F., and Weingarten, L. I., (1993), "Failure in Ductile Materials Using Finite Element Methods," Structural Crashworthiness and Failure, edited by T. Wierzbicki and N. Jones, Elsevier Applied Science, The Universities Press (Belfast) Ltd.
5. Bammann, D. J., Chiesa, M. L., and Johnson, G. C., (1996), "Modeling large deformation and failure in manufacturing processes," Theoretical and Applied Mechanics, ed. T. Tatsumi, E. Wannabe, and T. Kambe (Elsevier, Amsterdam), 359-376.
6. Baskes, M.I., (1992), Phys. Rev. B 46, 2727.
7. Coleman, H. W., and Steele, W. G., (1999), "Experimentation and Uncertainty Analysis for Engineers", 2nd Edition, John Wiley, New York, NY.
8. Dawson, P., Boyce, D., MacEwen, S., and Rogge, R. (2001) "On the influence of crystal elastic moduli on computed lattice strains in AA-5182 following plastic straining," Mat. Sci. Engrg., A313, 123-144.
9. Ganapathysubramanian, S and Zabaras, N., (2004), "Design across length scales: A reduced-order model of polycrystal plasticity for the control of microstructure-sensitive material properties," Computer Methods in Applied Mechanics and Engineering, Vol. 193, pp. 5017-5034.
10. Graham-Brady, L. L., Arwade, S. R., Corr, D. J., Gutierrez, M. A., Breysse, D., Grigoriu, M., and Zabaras, N., (2006), "Probability and Materials: from Nano- to Macro-Scale: A Summary," Probabilistic Engineering Mechanics, Vol. 21, pp. 193-199.
11. Horstemeyer, M. F. and Ramaswamy, S., (2000a), "On Factors Affecting Localization and Void Growth in Ductile Metals: A Parametric Study," Int. J. Damage Mech., Vol. 9, pp. 6-28.
12. Horstemeyer, M. F., Lathrop, J., Gokhale, A. M., and Dighe, M., (2000b), "Modeling Stress

State Dependent Damage Evolution in a Cast Al-Si-Mg Aluminum Alloy," Theoretical and Applied Fracture Mechanics, Vol. 33, pp. 31-47.
13. Horstemeyer, M. F., Matalanis, M. M., Sieber, A.M., and Botos, M.L., (2000c), "Micromechanical Finite Element Calculations of Temperature and Void Configuration Effects on Void Growth and Coalescence," Int J. Plasticity, Vol. 16.
14. Horstemeyer, M. F., (2001), "From Atoms to Autos A New Design Paradigm Using Microstructure-Property Modeling, Part 1: Monotonic Loading Conditions," Sandia National Laboratories, Sand2000-8662, Livermore, CA.
15. Horstemeyer, M. F., Wang, P., (2003), "Cradle-to-Grave simulation-Based Design Incorporating Multiscale Microstructure-Property Modeling: Reinvigorating Design with Science," J. Computer-Aided Materials Design, Vol. 10, pp. 13-34.
16. Horstemeyer, M.F., Gall, K. A., Dolan, K., Haskins, J., Gokhale, A.M., and Dighe, M.D., (2003) "Numerical, Experimental, and Image Analyses of Damage Progression in Cast A356 Aluminum Notch Tensile Bars," Theoretical and Applied Fracture Mechanics. Vol. 39, n 1, p 23-45.
17. Horstemeyer, M. F., Negrete, M., and Ramaswamy, S., (2003), "Using a Micromechanical Finite Element Parametric Study to Motivate a Phenomenological Macroscale Model For Void/Crack Nucleation in Aluminum with a Hard Second Phase," Mechanics of Materials, Vol. 35, pp. 675-687.
18. Horstemeyer, M.F., Solanki, K. and Steele, W.G., (2005) "Uncertainty Methodologies to Characterize a Damage Evolution Model," Proceeding of International Plasticity Conference, Hawaii.
19. ISO, (1995), International Organization for Standardization, Guide to the Expression of Uncertainty in Measurement, ISO, Geneva.
20. Kamat, R.G., Butler, Jr., J. F., Murtha, S. J., and Bovard, F., S., (2002), "Alloy 6022-T4E29 For Automotive Sheet Applications," Materials Science Forum, 396-402, 1591-1596.
21. Kamat, M. Z., and Kassner, M. E., (2002), "Tensile and Fatigue Properties of Aluminum Alloy Sheet 6022," Journal of Materials Engineering and Performance, Vol. 11, 166-168.
22. Kocks, U. F., Tome, C. N., and Wenk, H. R. (1998) "Texture and Anisotropy", Cambridge University Press, 1st edition.
23. Marin, E. B. and Dawson, P. R., (1998) "On modelling the elasto-viscoplastic response of metals using polycrystal plasticity." Comput. Methods Appl. Mech. Engrg., Vol. 165, 1-21.
24. Miao. W. F., and Laughlin, D. E., (1999), "Precipitation Hardening in Aluminum Alloy 6022," Scripta Materialia, Vol. 40, 873-878.
25. Rahman, S., and Xu, H., (2004), "A Univariate Dimension-Reduction Method for Multi-dimensional Integration in Stochastic Mechanics," Probabilistic Engineering Mechanics, Vol. 19, pp. 393-408.
26. Shilkrot, L. E., Miller, R. E., and Curtin, W. E., (2004), "Multiscale Plasticity Modeling: Coupled Atomistics and Discrete Dislocation Mechanics," Journal of the Mechanics and Physics of Solids, Vol. 52, pp. 755-787.
27. Triboindenter User Manual, NRL-M-023 v. 5.0, Hysitron Inc., Minneapolis, 2005.

K. Cyberinfrastructure

Co-Principal Investigator: Tomasz Haupt
Center for Advanced Vehicular Systems
Mississippi State University (MSST)
PO Box 5405, Mississippi State, MS 39762
(662) 325-4524, fax: (662)325-5433, haupt@cavs.msstate.edu

Technology Area Development Manager: Joseph A. Carpenter
(202) 586-1022; fax: (202) 586-1600; e-mail: joseph.carpenter@ee.doe.gov

Contract Monitor: Aaron Yocum
(304) 285-4852; fax: (304) 285-4403; e-mail: aaron.yocum@netl.doe.gov

---

Contractor: MSST
Contract No.: 4000054701

Objective

- Design and develop cyberinfrastructure to exploit the recent transformative research in material science involving multiscale physics-based predictive modeling, multiscale experiments and design.

- This project is aligned with the United States Automotive Materials Partnership (USAMP) Integrated Computational Materials Engineering (ICME, see 6.F) effort for the Mg international pilot project (see 6.C).

Approach

- The development of the cyberinfrastructure to support the capabilities described above will leverage tools, technologies, and software approaches developed by other large-scale, scientific cyberinfrastructures, in particular GEONGrid (http://www.geongrid.org/) and NEESit (http://it.nees.org/). Much of the foundation of the infrastructure is common across domains (security, grid integration, etc) and can serve to bootstrap this project to delivering an initial working solution in a relatively short time frame. Some initial customization will be needed to support the unique aspects of this project, but we have the experience and contact with the other projects to ensure those are relatively quick. After the initial system is developed, we expect many of the advanced capabilities of the system to require additional software development or customization and entirely new development to support additional features. Hence, we will proceed with a two-stage development model: phase one to initially leverage existing software and tools to bring up a working software infrastructure, then phase two to evaluate and further develop missing or insufficient software as needed to support the project requirements.

- The user will access the engineering virtual organization (EVO) services through a grid portal. The grid portal will manage the user credentials and user sessions, and will host portlets implementing rich graphical user interfaces (GUI) for services rendered by the infrastructure (database queries, remote job submission, etc.). The GUI will be implemented using the combination of Java Applets, Java Script and Asynchronous JavaScript and eXtensible Markup Language (XML) (AJAX). In addition, the portal will enable accessing the services from grid-enabled stand-alone applications. Finally, the software integration will be accomplished applying Java Business Integration (JBI) approach using an open-source service bus implementation.

Accomplishments

- **Task 1**: Identify, acquire and deploy servers supporting simple object access protocol (SOAP), Web Service Description Language (WSDL) and integrating Message Oriented Middleware. This task has been completed. We selected and installed: Globus Toolkit 4 grid computing (remote access to resources, security); Apache/Tomcat Web Server with support for J2EE (Java 2 Platform, Enterprise Edition), GridSphere (portlet container), JBoss (Enterprise JavaBeans container), Axis (SOAP and WSDL container), ServiceMix (JBI – Service Bus), and Microsoft's Share Point Server for the deployment of USAMP community portal.

- **Task 2:** Create a virtual organization encompassing all partners involved in the project research and implement authentication, authorization, and auditing mechanisms according to policies negotiated with the system administrators. This task has been modified. At this phase of the project, there is no need for resource sharing (e.g., running jobs on machines outside MSST campus or allowing non-MSST employees or students to run jobs on MSST systems). On the other hand, the USAMP project mandates the development of an electronic "community of practice" web-site that allows development and integration of multiscale, physics-based material models for selected properties and processes. To this end, we deployed the Share Point Server configured to be accessible from any place in the world with all necessary security setting protecting against misuse and cyber-vandalism. The portal has been made available to selected test users participating in the USAMP Mg project. Eventually, the server will provide a single point of access to all services rendered by the cyberinfrastructure, through the contents aggregation.

- **Task 3:** Develop and deploy services for secure access to remote resources (job submission to high performance platforms, job monitoring, access to file systems and databases). Most of the services have been developed and utilized in Task 5. This present Task 3 is essentially completed; however, the developments in Task 5 to 7 may require some additional customization and/or hardening of the implementation.

- **Task 4:** Develop support for service orchestration and workflows. The service orchestration is achieved by employing the Service Bus and used in Task 5. The interfaces for composing workflows remain to be implemented. This means that Task 4 is 50% completed.

- **Task 5:** Develop specific services supporting design optimizations (design-of-experiment (DoE)), metamodels, optimization, input/output (I/O) for ABAQUS and other finite-element analysis (FEA) codes from multiscale and multiscale simulations (bridges from Tasks 1 and 2). This task actually comprises three tasks: online repository of material properties, support for design optimizations and support for multiscale simulations. This builds on the results of activities within Tasks 1, 3, and 4, and is the subject for the integration effort in Tasks 2 and 7. The preliminary version of the repository (including the capability to generate mechanical material properties using internal state variables – DMGfit – see Figure 1) has been developed and made available for testing by engineering students at MSST (presented at 7th international conference on Grid Computing, Barcelona'06, and International Conference on Grid Computing and Applications, Las Vegas 2007). For design optimization, we have implemented support for the creation of metamodels: DoE, automatic-creation ABAQUS and LS-DYNA input decks with the value of design variables according to DoE results, running FEA codes on remote, high-performance resources, collecting the output files, and extracting the responses to build a metamodel (presented at e-Science'06 conference, Amsterdam, NL). In parallel, in collaboration with Project 4, we are developing a Flexible Advanced Metamodeling Estimator (FAME) for automatic generation of best metamodel-based surrogate model (c.f. 4.3). The support for multiscale simulations has been postponed to the later phases of the project.

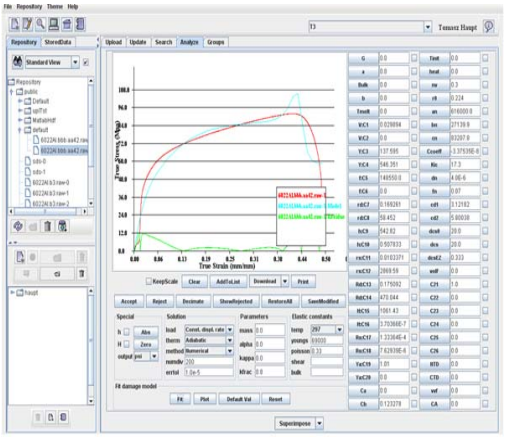

Figure 1. Repository of Material Properties - a snapshot of the web-based user interface.

- **Task 6:** Develop a resource-management system for multiscale simulations. We have developed an overlay

scheduler to support adaptive multiscale simulations (presented at The Minerals, Metals and Materials Society (TMS) 2006 conference).

- **Task 7:** Integrate all components into a single system (cyberinfrastructure). Verify and validate the system by running design optimization and multiscale cases. Improve the GUIs, performance and robustness. These activities are about to be initiated.

Future Direction

- During the first year, the basic infrastructure has been created that forms a solid foundation for creating the cyberinfrastructure for EVOs. Furthermore, preliminary implementation of vital components has been done, in particular support for design optimizations and service-based repository of material properties. During year two, the production version of these components needs to be developed and deployed. This involves thorough tests and validation and gathering feedback for early users. The components need to be integrated into a single versatile and expandable system accessible by the Grid Portal. The final integration is the subject of Task 7, which will dominate the activities in year two.

- The system at the end of year two will provide the basic collaborative system enabling design optimization and multiscale experiments and simulations. This base system will be further expanded adding new software components and the implementation will be brought to the next level to support autonomous execution of complex computational workflows, including self-optimizations (scheduling in high-performance, heterogeneous, distributed environments and adaptive resource management), self-healing (fault-tolerance through monitoring of resource availability, fault detection, and conditional workflows), self-protection (context-sensitive security), and self-configuration (automatic detection of new hardware, software, and data components).

- The specific activities for the year two include:
    - **Repository of Material Properties:** The preliminary implementation requires further optimizations (both back-end services and GUIs, as well as systematic validation. The repository is already on-line ready for the early users, and we are in the process of collecting the users' feedback. Currently, it provides support for fitting parameters to the Bammann-Chiesa-Johnson (BCJ) plasticity model (see 6.J) and to the damage model. Additional models and more material properties are being prepared for the integration (optical properties, fatigue, etc).
    - **Support for Design Optimizations:** Currently, two approaches have been adopted. In the early stages of this project we have created grid-enabled system that automates performing design optimizations and concurrent execution of FEA models on remote, high-performance systems. The second approach is to develop a system for adaptive metamodeling (FAME). The next step is to merge the two approaches into a single system with user-friendly interfaces and develop flexible resource-management techniques to minimize the turnaround time for generation metamodels. In the later phases, the subsystem for design optimizations will be integrated with the subsystem for multiscale simulations.
    - **Support for Multiscale Simulations:** We have developed an overlay scheduler to manage an adaptive tree of processes spawned while performing multiscale simulations. Further development of the support for multiscale simulations has been postponed. The concurrent developments of multiple system components jeopardize timely completion of the tasks and the multiscale simulations are the least mature for automation and integration (as opposed to repository of material properties and support for design optimizations).
    - **Portal for the Virtual Organization:** The USAMP ICME for the Mg international pilot project redefined our initial requirements for creation of the Virtual Organization. The new requirements call for the deployment of a collaborative portal based on Microsoft's SharePoint server. This portal will enable sharing documents and management of the tasks and projects between the participants of the ICME Mg project. In the next step, the support for sharing data will be added and, finally, all capabilities of the cyberinfrastructure under development at MSST will be made available through this portal.

Introduction

The objective of this project, Cyberinfrastructure, is the establishment of an EVO to exploit the recent transformative research in material science involving multiscale, physics-based predictive modeling, multiscale experiments and design, in conjunction with robust design and manufacturing process optimizations with uncertainty and cyberinfrastructure development (Figure 2). The information, data, and software tools generated by the virtual organization will enable closing the significant knowledge gaps in a unifying, physics-based modeling theme that captures a broad range of materials, admits structure-property relations, can be used in simulation-based design, can be implementable into finite-element codes, can be experimentally validated, can capture history effects, and can morph into a metamodel for rapid use prognostics. The knowledge and data will come from many sources across organizational boundaries (distributed databases of geometries, material properties, manufacturing processes, experimental results coming from different labs, etc.) allowing experts from different disciplines (such as bio-inspired material models, models at different length scales, metamodeling and optimizations) to work together toward the common goal.

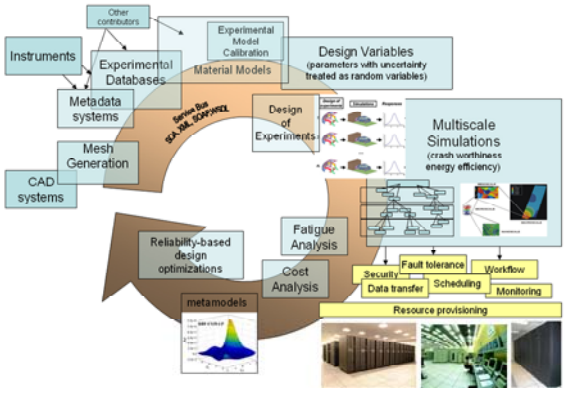

Figure 2. The vision - the cyberinfrastructure will integrate distributed databases of engineering knowledge and computational workflows for multi-objective, multiscale, design optimizations under uncertainty.

The implementation will follow Service-Oriented Architecture paradigm. The user will access the EVO services through a grid Portal. The grid portal is implemented using GridSphere – a robust and widely used implementation of the JSR-168 Portlets specification. The grid portal will manage the user credentials and user sessions, and will host portlets implementing rich GUIs for services rendered by the infrastructure (database queries, remote-job submission, telepresence, etc.). The GUI is being implemented using the combination of Java Applets, Java Script and AJAX. In addition, the Portal will enable accessing the services from Grid-enabled stand-alone applications. For example, modules for MATLAB and ABAQUS are planned to allow these applications to access the material- properties databases directly from the native GUI (MATLAB, ABAQUS, respectively) and submit jobs to remote, high-performance platforms.

The Portlets will delegate the actual processing of the user requests to services implemented in Java. The services will form a façade for the Grid fabric services such as Globus grid resource allocation management (GRAM) — remote-ob submission, direct-access interface system (DAIS) – remote-database access, and gridFTP (file transfer and remote file system access) as well as Data Turbine (telepresence). The overall architecture of the proposed cyberinfrastructure for engineering Virtual Organization is shown in Figure 3.

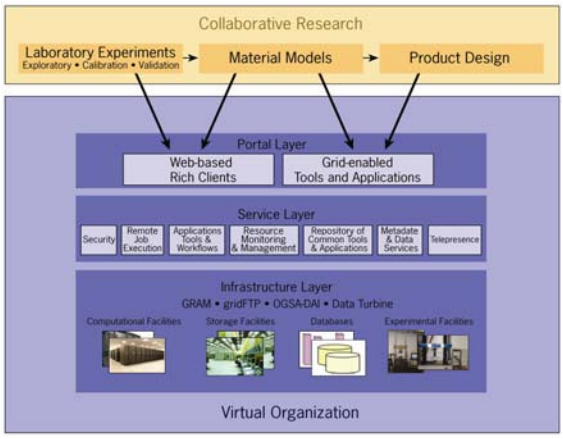

Figure 3. Architecture for EVO.

Finally, the software integration will be accomplished applying JBI approach using an open-source Service Bus implementation, as shown in Figure 4.

Figure 4. Horizontal software-integration bases on the service-bus concept (as opposed to currently-used centralized, "hub and spoke" architectures leading to vertical silos and stovepipes.

Repository of Material Properties

Introduction

The goal for this repository is threefold. Firstly, the repository provides the support for *ad-hoc* collaborations that require sharing restricted-access data between members of dynamically-created groups. Secondly, the repository supports creating different views on the storage by virtual gathering metadata records in hierarchical collections mimicking a tree of folders. Finally, the repository supports data transformations on-the-fly taking the advantages of the flexibility of the enterprise service bus (ESB)-based architecture.

The system is designed to support sharing thousands of data sets of a small to moderate size (gigabytes) per group. The number of the data sets mandates a support for metadata describing these data sets thus allowing for queries. The manner how the data is described, that is, the metadata schema, may vary from group to group and, in addition, it may change in time adapting to the evolving user needs. Therefore, it is necessary to introduce a very flexible metadata system without compromising the performance of queries. The data may be stored at different locations that support different mechanisms or interfaces for data access. Finally, strong authentication and group-based authorization mechanisms are required.

The metadata catalog and the storage are deliberately organized independently from each other. The storage is implemented as a flat collection of files and the physical location of a particular file is determined by the storage. The user can access it only by its logical name. The resolution from the logical name to the physical location is performed dynamically by an independent service – the replica locator. The metadata catalog is conceptually implemented as a single "business" structured query language (SQL) table. The columns of the table represent the attributes of the metadata, with the logical name of the file as one of the attributes. The user may query the catalog to retrieve a set of logical names of files that match the selection criteria constructed as Boolean expressions involving the values of the metadata attributes – equivalent of SQL queries. In addition, the metadata system supports capturing the parent-child relationships between the metadata entries adding to the flexibility creating different views on the catalog and, consequently, allows the user to customize the interfaces for the data selection.

The data stored in the repository are meant to be consumed by the user applications (as input files). It is well known fact that hardly ever any two applications accept the data in the same format. It is thus imperative that the repository provides support for data transformations. The transformation can be simple such as format translations (e.g., the parameters of a stress-strain curve need to be formatted differently for ABACUS and LS-DYNA finite-analysis simulations) or may involve more complex processing such as performing model fits.

The repository is implemented as an aggregate of independent services: metadata service, replica locator, data storage and authorization service, and transformation services, all integrated using Apache's ServiceMix - an Open Source implementation of an Enterprise Service Bus compliant to the JBI specification.

Model of the Repository

Each entry in the repository (a file, a database record or other data item) is associated with a metadata record (a variable-length vector of attributes name-value pairs that describes the properties of the entry). The attributes capture the properties of the resource; both generic properties (such as ownership of the data, time of creation and data format) and application-specific, user-defined attributes that facilitate queries. The

details of that flexible metadata support that allows the evolution of the metadata schemas without risking loosing the integrity of the data is described elsewhere. Notably, the metadata records do not capture the physical location of the resources.

Each metadata record is uniquely identified by a uniform resource identifier (URI). The relationship between the metadata record URI and the uniform resource locator (URL) of the corresponding repository entry (or its replicas) are maintained by a replica locator. Consequently, the repository is implemented as three independent services: metadata service, replica-locator service, and storage services.

Creating the repository as an aggregate of three independent services, as shown in Figure 5, has clear advantages. The separation of concerns simplifies the implementation and enables reusing existing components, if required. For example, depending on the characteristics of the data sets to be maintained by the repository, the storage service can be implemented as a simple file system accessible through a secure file-transfer protocol such as gridFTP, or it can be implemented on top of a relational database system. If mass-storage and high-performance protocols are needed, a heavy-duty system such as SDSC Storage Resource Broker (SRB) can be used as the storage service instead. Other advantages, including the support for *ad-hoc* collaborations and creating different views are discussed below.

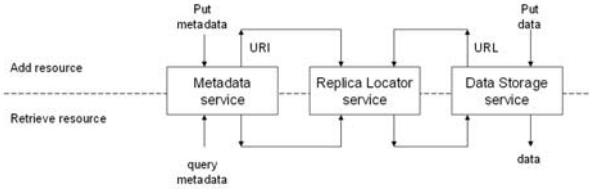

Figure 5. High-level model of the repository.

To add a data resource to the repository, the user puts a metadata record to the metadata service which returns URI of the resource and puts the file to the data storage which returns URL. The URI-URL pair is then put to the replica locator. To retrieve a data resource, the user queries the metadata repository to obtain the URI of the resource (or uses cached URI). The URI is resolved to URL by the replica locator. The URL is used to retrieve the corresponding data resource.

The repository is designed to facilitate *ad-hoc* collaborations that require sharing of restricted-access data between members of dynamically-created groups. To achieve this functionality, the repository must provide support for creating and managing groups of users and provide access-control mechanisms that allow or deny the access to data resources based on the user's membership in a group.

Support for *Ad-Hoc* Collaborations

The repository access-control mechanisms are based on privileges assigned to groups to perform specified operations on the entries. Each entry is associated with one or more groups by setting permission flags which specify permissions for the group members to perform operations on the resources. The user may be a member of a several groups, with each group having different privileges, that is, rights to perform specific operations on the same resource. For example, let the resource permission flags be set to grant members of group A read access to a file and deny members of group B privileges to the same file. To download the file from the repository, the user must prove that he or she belongs to group A; and, to delete the file from the repository, she must prove that she is a member of group B. If she is a member of both groups, she will be allowed to read and/or delete the file.

The current authorization frameworks are not applicable to a distributed repository where trust relationship between services is required, with one service providing authorization necessary for the next service. The solution adopted here extends the Virtual Organization Membership Service (VOMS) architecture. The authorization is group-based with Group Membership Authorization Service (GMAS) responsible for maintaining the user the membership in a group. Each user is authorized to create a new group and the group moderator (by default the creator) can add and remove group members. The user can then securely share data with the other members of the group in a distributed repository, as shown in Figure 6.

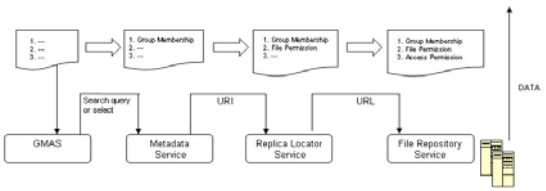

Figure 6. Starting with GMAS issuing a Security Access Markup Language (SAML) assertion about the user's membership in a group, and then collecting SAML assertions from the component services (Metadata and Replica Locator) the user assembles a complete assertion document that allows it to retrieve data from a data service.

Since the metadata service effectively acts as an index of all data entries anyway, it is natural that the resource permission flags are maintained as a part of the metadata record. It has an additional advantage of providing access control not only to the data entries but also to metadata records. Controlling the access to metadata is important since the metadata records may reveal too much information on the contents of the data and, in addition, the very existence of the data may be confidential.

Custom Views on the Repository Contents

The metadata catalog is conceptually implemented as a single "business" SQL table. The user may query the catalog to retrieve a set of logical names of files that match the selection criteria constructed as Boolean expressions involving the values of the metadata attributes – equivalent of SQL queries. In addition, the metadata system supports capturing the parent-child relationships between the metadata entries. Since the organization of the metadata is independent from the organization of the file repository, it is possible to create different views on the catalog and, consequently, allows the user to customize the interfaces for the data selection.

In particular, two categories of the interfaces can be created: folder-based and attribute based. Assume that the user is collecting data from an instrument measuring the mechanical properties of a material sample. The user may want to make several measurements, experimenting with different instrument settings, making measurements at different conditions (temperature, sample orientation, etc.), or using different samples of the same material. It is very likely that the user introduces some conventions for naming the resulting files and it might be convenient to organize the files in a tree of folders. To achieve that, the interface provides controls for creating and managing folders. However, the folders are "virtual". Instead, the metadata attributes are set to capture the intended parent-child relationship that can be displayed as a tree of files and folders making it easy for the user to find the results. Another user, however, might be interested is seeing all results for a given material obtained at a specific conditions, regardless of the who, when, and where of the measurement (subject to access control). In such a case, the attributes describing the parent-child relationship are simply ignored and a different tree is presented to the user. The data are sorted by materials, by sample types, by experiment types, etc., in the order specified by the user.

Data Service Facade

Construction of the repository from the independent services has many advantages. On the other hand, it is difficult for the end user (or the user agent) to use such a distributed system. Many conceptually-simple operations, such as retrieving a file, require making multiple requests to different services. The above mentioned flexibility of the system adds to the complexity of using the repository: the user must not only know the right order of service invocations, but also needs to know interfaces of the particular services and the communication protocols used by these services. Furthermore, since all services act independently from each other, maintaining repository consistency becomes difficult (e.g., each metadata record corresponds to at least one data resource and each data resource has associated metadata records).

To ease these difficulties, all constituent services of the repository are hidden from the user behind a facade which is the middle-tier service that orchestrates the services and exposing a simple, intuitive interface for the end user. Now, given the URI of the resource (from querying the metadata service or otherwise), there is a single method of the facade to retrieve the file. The invocation of this method results in all actions needed to get the authorization assertions, resolving URI to the

physical locations and returning the data stream. To achieve that, the facade employs the business delegate pattern that delegates the actual implementations of the back-end service clients to service providers which understand the transport and assertion requirements of the corresponding services. In addition, the provider-based architecture makes it easy to retarget the repository to a different implementation of any of the constituent services – it requires just replacing the service provider without the need for modifications of the facade interface. The business logic of the facade also enforces the integrity of the repository. For example, a request to remove a data resource from the storage automatically triggers appropriate actions of replica-locator and metadata services initiated by the facade.

Data Transformations

Hardly ever any two applications accept the data in the same format. It is thus imperative that the repository provides support for data transformations. There are two basic types of data transformations. One type facilitates relatively simple operations such as format translations or processing data headers that can be performed on-the-fly. The other type supports the processing of large files or making complex transformations. These transformations are delegated to high-performance platforms. The data transformations are independent from the metadata catalog or file repository services, and need to be implemented as independent services (the loose-coupling principle) and invoked either prior to the data uploading or after retrieving the data from the file repository, but before returning the data to the end user.

As proof-of-concept, several data transformations have been developed. Among the purposes of the material properties repository is the collection of data coming from measurement of stress-strain curves. The data coming from different instruments are, very expectably, in different formats. A transformation service hides these differences from the instrument operator who uploads the data to the repository. The service creates a metadata record by combining the information from the header automatically generated by the instrument from the system (e.g., time and the operator id), and the data typed in by the operator (the instrument has no way to know what material and in what manufacturing stage, e.g., after rolling or stamping, is being measured) and, then, from the measured values of the displacements and loads calculates the true stress and strain values. Once this “transformation” is complete, the metadata and data pair are uploaded to the repository. When retrieving the data from the repository, the user may specify the desired format, e.g., raw data, data formatted to match the syntax of the ABAQUS FEA package, or others. Such format translation is delegated to another transformation service that is invoked automatically after retrieving the data from the repository and before sending the data to the user. The National Aeronautics and Space Administration (NASA) Rapid Prototyping Capabilities project has different requirements. An example of a data transformation is the generation of a time series of selected observables for a selected geographical region. It involves retrieving a set of satellite images for the specified time period, re-projecting them so that an x-y pixel represents the same spatial location on each image, and then filtering out “noise” pixel (e.g., cloud cover), and finally filling the gaps resulting form the noise elimination by comparing images at adjacent time frames. These operations involve significant central processing unit (CPU) power and, since most of the procedure is embarrassingly parallel, it is desirable to perform it on a high-performance cluster.

Integration of Data Repository Services Using the ESB

The primary functionality of the service bus is routing messages between services associated with it. There are two base types of associations. The service can be plugged into the bus container as so-called service engine to be directly invoked through a Java message service (JMS). Alternatively, a service may be deployed in a separate container and be invoked through web-service interface (WSDL). The web service invocation is facilitated by a binding service bus component.

The incoming requests, generated by a web portal or a stand-alone client, are accepted by a custom-developed, hypertext transfer protocol (HTTP) input component. The input component effectively acts as a service broker forwarding the requests to the target services that generates the actual responses to the client requests. To make it possible, the client's request must provide a signature of the target service. In order to invoke the service (i.e., to forward the request) the signature must be resolved into the service endpoint reference (EPR). To this end, the broker uses a service directory--another custom service engine. The service signature is a collection of the service attributes. In the simplest case, it could be just the service name. The service WSDL interface could serve as the service signature; however, for this data repository, most of the transformation services implement the same WSDL interface making it easy to "bind" the actual transformation late, depending on the context of the request. The EPR may refer to an "atomic" service (either a service engine or a binding component) or refer to an orchestrating service (e.g., a Business Process Execution Language (BPEL) engine, or a service facade) that aggregates several services in order to generate the final response the client requested.

Architecture of the Repository

The architecture of the repository is shown in Figure 7. The clients, implemented as Java applets or stand-alone applications implemented in Java, Python, or otherwise, communicate with the ESB through HTTP/HTTPS. The Input Component/Service Broker accepts three types of requests: metadata query, data upload (that may or may not involve the data transformations), and data download (that may or may not involve the data transformations). The metadata query allows the user to search the metadata catalog to locate the data set of interest, create custom views on the data repository, as well as uploading and downloading of data are orchestrated by the data-repository facade, as described above. Consequently, the client requests to perform these operations are simply forwarded by the service broker to the façade service engine. The data facade invokes the constituent service services as needed through the binding components.

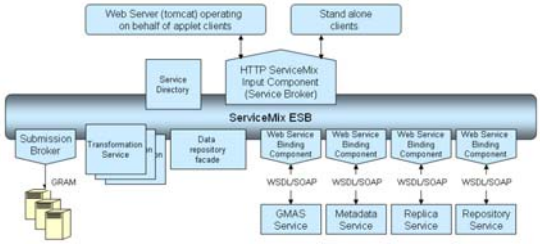

Figure 7. Architecture of the data repository integrated by ESB.

The data transformations, on the other hand, are bound dynamically. If the repository operation requires a transformation, the name of the transformation is passed as the request argument. The broker resolves the transformation name into the service EPR using the service directory, and invokes the service before or after invoking the data-facade services, depending whether data are uploaded to or downloaded from the repository, respectively. Simple transformations are implemented as ESB service engines, while complex transformations are executed by the submission broker – a binding ESB component. The submission broker is responsible for setting the run-time environment (setting the environmental variable, creating a working directory, etc.), staging in data, executing and monitoring jobs on remote systems, and finally passing the results to the requested destination (typically through a third-party data transfer). Since all transformations implement the same WSDL interface (the transformation-specific parameters are grouped as a single array of strings), the dynamic binding allows seamless adding or replacing existing transformations.

Summary and Future Work

The system has been internally deployed at MSST as is subjected to test users. The feedback from the early users will guide us in improvements of the User Interfaces, improvements in the system functionality, and hardening the implementation. Once tested and validated, it will serve the ICME Mg project. In addition, we plan adding new transformations for extracting more material properties including optical properties.

Support for Design Optimizations

Simulation-Based Design Optimizations

Simulation-based design optimization is playing an increasingly important role in engineering-product development. It enables engineers to make optimal product design and manufacturing-process decisions, reduce or eliminate the need for physical prototyping, and increase the quality of manufactured products. This importance is also evident in the development and marketing of several commercial optimization software tools (e.g., DOT, iSIGHT) that can be interfaced with computer-aided design/computer-aided engineering (CAD/CAE) and engineering simulation programs to accommodate a paperless product-design activity.

The rapid development of computer technology and commercial simulation tools has enabled engineers to solve more complex problems and obtain more details to enhance knowledge. For example, it is now possible to perform full-scale, finite-element (FE) simulations of vehicle crashes with commercial FE codes and parallel computers. However, the increased complexity has significantly increased the computational cost that, in turn, prevents engineers from combining the simulation tool with an optimization method, which is an iterative procedure and requires hundreds or even thousands of simulations to perform one design. To alleviate the high computational cost of full-scale simulations, yet maintain the level of complexity, the metamodeling approach has been widely adopted in simulation-based design optimization.

In the metamodeling approach, the expensive simulation tool is replaced with a surrogate approximation model (metamodel) that is in explicit form and efficient to evaluate. The metamodel is created from the results of some predefined simulations determined by DoE methods. Figure 8 illustrates the procedure of simulation-based design optimization using DoE and metamodeling. There are four major components in this procedure: DoE, simulation, metamodeling, and optimization--which serve as four independent functional blocks.

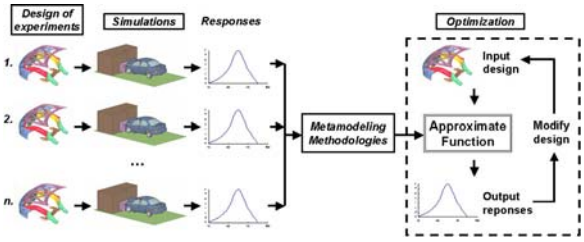

Figure 8. Workflow for simulation-based optimization using DoE and metamodeling.

Since a limited number of simulations are used in creating the metamodel, the model accuracy will depend on how well the selected designs represent the design space. To this end, the DoE methods such as factorial design, central composite design, Taguchi orthogonal array, and Latin hypercube sampling, are typically used to create the samples and referred to as the response surface methodology (RSM). For high-order, nonlinear responses, other metamodeling methods using high-order, nonlinear functions, particularly the radial basis functions (RBF), work best.

With the created metamodels representing responses within the design space, the optimization can be carried out using existing optimization methods such as gradient-based or direct-search algorithms. As pointed out by the no-free-lunch theory, there is no single optimization method that is good for all types of problems. Therefore, it is preferred to apply different optimization methods at this stage to obtain the best solution.

The Need for Cyberinfrastructure

The complexity of the new generation of simulation codes demands the employment of high-performance computing platforms, even when employing the metamodeling approach. However, the reduction of the computational costs down to an affordable amount is achieved at the price of a very tedious and error-prone manual effort by the designer to submit, monitor and coordinate hundreds of jobs in heterogeneous, distributed environments. Performing simulation-based optimization is not only a time consuming but it also requires the designer to learn the arcana of ever-changing information-technologies (IT) such as operating systems, batch systems, storage systems, networking, and security. To reduce the time and cost associated with the design, it is thus

imperative to provide a cyberinfrastructure that effectively and efficiently manages high-performance computing resources. Furthermore, the infrastructure should provide mechanisms of resource discovery (hardware, software and data) and seamlessly integrate simulation programs (including multiscale simulations), CAD/CAE tools and various functional components such as DoE, metamodeling, and design optimization.

Functional Requirements

Figure 9 summarizes the required minimum functionality of the system needed to automate the optimization process. Conceptually, the system comprises three major components: a GUI, execution environment, and data repositories.

The GUI provides means for defining the optimization problem and specifying the optimization workflow. The GUI also embeds clients to a grid infrastructure that provides access to grid resources including remote-data repositories (such as product geometries and material properties) and execution environment for submitting, controlling, and monitoring the workflow.

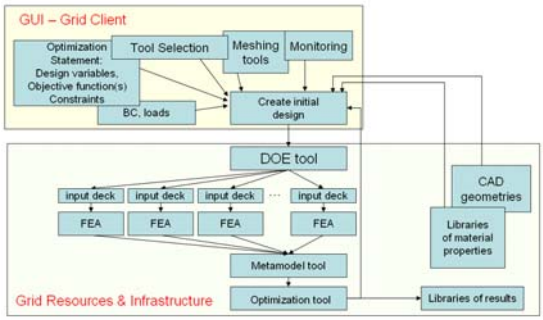

Figure 9. Functionality of the simulation-based optimization system.

Defining the Optimization Process

The starting point for the design optimization process is the specification of the initial design. This involves the creation of the geometry of the initial design (usually imported from CAD), specification of material properties (taken from the material properties databases), as well as the definition of boundary conditions, loads, and constraints. The optimization problem is then defined by a vector of design variables **x**, one or more objective functions f(**x**) and set of constraints g(**x**) $\leq$0, h(**x**) =0.

To solve the stated problem, computational tools needs to be selected. The first tool to be selected is a simulation code to perform FEA. There are many commercial packages available for that purpose such as ABAQUS, LS-DYNA, or PAM-CRASH, each optimized for a particular class of problems. Once the FEA tool is selected, the initial design must be expressed in terms of an input deck formatted for the selected tool.

To finish setting up the optimization workflow, the DoE tool, the metamodeling tool, and optimization tool need to be selected. Typically, each such tool requires the selection of a particular method and its parameters.

For design optimizations of complex systems, it is vital to provide the capability of selecting the best tool (or the best method) for the problem at hand, including a support for "plugging in" new tools as needed. Such flexibility can be achieved by using the horizontal integration approach, as opposed to vertical stovepipes. Horizontal integration means the adoption of uniform management interfaces so that the large numbers of resources (such as software and hardware), distributed over what used to be distinct silos, can be allocated, used, monitored, and managed in a common and automated manner.

Optimization Process Workflow

Once the optimization process is defined, it is submitted for execution. The DoE module generates sets of values of the design variables that are used for automatic generation of FEA input decks, one for each set of design variables' values. The input decks are then staged at remote computational servers and used to run the FEA analysis. Since there are no data dependencies between different FEA runs, all of them can be run concurrently if enough computational resources are available. Once all instances of the simulation code are completed, their outputs are parsed to extract the value of the responses which, in turn, are used to create the metamodel that is the input for the optimization module.

To increase the engineer's productivity, it is imperative that, once the optimization problem is interactively defined through the GUI, the optimization workflow runs asynchronously, automatically and autonomously. It should run asynchronously to let the engineer perform other tasks while waiting for the optimization results, as simulating complex systems can take hours or days to complete. The workflow can be asynchronous only if the complete process is automated (generation of input data sets for all software components in the workflow, setting the run environment, staging files in and out, generation of batch scripts, allocating the resources, etc.), and autonomous (self-optimizing, adapting to changes in the resource availability and capable of recovering from failures).

Cyberinfrastructure

The design-optimization process requires horizontal software integration with loosely-coupled components. The loose coupling is enabled by web services or any service-oriented architecture (SOA), such as Open Grid Services Architecture (OGSA) - based grid infrastructure. Loosely-coupled services, even if they use incompatible system technologies, can be joined together on demand to create composite services; however, participants must establish a shared semantic framework to ensure messages retain a consistent meaning across participating services. Furthermore, the grid infrastructure establishes a separation between the service provider and the consumer and provides the ability to negotiate a desired quality of service from the provider. All these properties are needed for asynchronous and autonomous execution, making the grid infrastructure a good choice for the implementation of the cyberinfrastructure for the optimization workflow. The architecture of the system is shown in Figure 10.

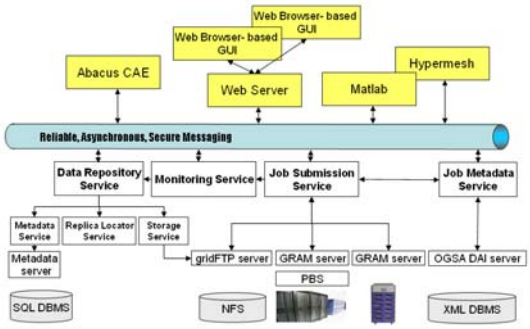

Figure 10. Cyberinfrastructure for horizontal integration.

Horizontal Integration

The first step towards horizontal integration is the decoupling of the user applications, such as design-optimization process, from the hardware. A workload manager would use common grid infrastructure mechanisms (OGSA services) to discover available resources and deploy application components onto these resources. As load increases, new resources could be automatically (and temporarily) allocated to, and used by, the application. In other words, the grid resources—compute servers, file systems, databases—need to be provisioned on demand by making them available as services. Following the loose-coupling strategy, it is not important what technology is used to implement these services. The system described here employs GRAM, OGSA-DAI, and gridFTP services included in Globus Toolkit 4 (GT4), and WSDL-based (Axis) Metadata Service developed at MSST and described in detail elsewhere. The rationale for this particular choice is the ease of availability. The GRAM service provides access to the remote compute servers (or resource-management systems such as PBS), gridFTP is used for file transfers effectively providing access to remote file systems, while OGSA-DAI and the Metadata Service provide access to remote databases.

The next layer of the infrastructure supporting horizontal integration comprises services for deploying application components onto selected resources, job monitoring and data access. Higher-level services, including resource discovery, brokerage, workflow enacting, adaptive scheduling and self-management, belong here, too. They will be added in the forthcoming phase

of this project; at present, this functionality is delegated to the clients.

Job Submission

Deploying application components onto computational resources is the responsibility of the Job Submission Service (JSS). The needed flexibility for submitting a particular application component on a selected hardware is achieved by employing a Job Descriptor (JD). The descriptor is an XML document that provides a "recipe" on how to run the component on target machines where the component is installed. The JSDL-like schema captures all information necessary to automatically generate a run script, a batch script, and/or Globus GRAM RSL string.

The JDs for all the application components needed for the design optimization process are maintained in an XML database deployed as a Grid Service (OGSA-DAI), referred to as Job Metadata Service (JMS). Each application component, such as FEA code, is uniquely identified by a URI. The URI for the selected component can be obtained from the Job Metadata Service itself by querying the database by application name and/or other application signature attributes.

The support for the selection of the tools is implemented by embedding the Job Metadata Service client in the GUI and hiding the syntax for queries from the end user. Adding new tools to the system is simply a matter of adding new JDs to the repository, assuming that the code is already installed, and that the user has authorization to use those systems.

To submit a job, the client needs to retrieve the corresponding JD from the Job Metadata Service and customize it for a particular run. This involves the selection of the target system from the list embedded in the JD itself and replacing the default values of job attributes (such as location of the input deck and other data files) by the actual ones. The updated JD is then sent as a payload of the request to the JSS. The JSS parses the JD and follows the recipe it contains. Typically, these are the operations that need to be performed: staging the input files (using gridFTP); if necessary, creation and staging execution scripts; creating the run environment (such as creating a working directory for the job); creating the RSL string; submitting the job request to the Globus GRAM server; creating a job entry in the job database (explained in the Job Monitoring section below); and, finally, registering itself for GRAM notifications. As the job executes, JSS forwards the notifications to the JMS, and when the job completes, it stages it out to the location prescribed in the JD using gridFTP.

The customization of a JD can be performed in separate steps (with a JD file passed from one service to another). For example, the location of the input files for FEA can be provided by the input deck creation tool, while the selection of the target system can be determined by a resource scheduler. The former creates a new input desk for each set of design variables' values as returned by the DoE module, and the scheduler is responsible for selecting resources so that all FEA simulations complete roughly at the same time. Such separation of concerns is an important element of the horizontal integration and the reusability of services. The DoE is independent of the choice of the FEA tool, input deck is FEA-specific (e.g., an ABAQUS input is formatted differently than LS-DYNA one), and the scheduler is a generic Grid service. In the current implementation, however, the customization of the JD is performed by the JSS client embedded in the GUI. This will change in the next release of the system.

Job Monitoring

All jobs submitted within the optimization process are run asynchronously and, therefore, there is a need to monitor their status. Resource Management Systems, such as PBS, provide this functionality for all pending and executing jobs. However, once the job completes, the information about it disappears. To remedy this, an independent Job Monitoring Service (JMS) is provided that persistently maintains information on all submitted jobs in a database. The job entry in the database is kept until the user explicitly deletes it.

Results produced by individual jobs are used to create a metamodel and, therefore, they are not of

direct interest for the user – as long as the optimization process proceeds as expected. If a failure should occur (for example, the FEA analysis produces results different than anticipated), the user must be provided with the means to identify the problem. Therefore, the JSS provides not only the information on the current status of the job (pending, running, completed) but also the complete provenance of the job (input deck, run scripts, etc.), and it provides the access to its output files. For example, the ASCII log file can be opened at the user workstation without the user explicitly transferring it, and binary data files can be downloaded for analysis using ABAQUS CAE by a single mouse click.

The JMS, which is a WSDL-based grid service, uses the data service (described below) to maintain the information about the jobs. The changes in job status reported by the GRAM server are forwarded to JMS by the JSS. File transfers, if requested by the user, are seamlessly made using gridFTP.

Data

The data, in particular input and output data sets that needs to be examined or shared between the users, are maintained by the data service (described in details elsewhere), composed of three independent services: Metadata Service, Replica Locator Service and Storage Service. The metadata (an XML-encoded, variable-length vector of attribute name-value pairs) allows for efficient queries and generation of multiple views on the data collections to fit the user's needs, regardless how the files are actually stored. It is implemented on top of J2EE and SQL Database Management System (DBMS). The storage service uses a Unix file system with gridFTP for file transfers. The replica locator provides the mapping between the logical file name (URI) and the physical file (URL). The Data Service is a WSDL service that act as a facade orchestrating the three constituent services.

GUI

The user interactions with the system logically split into two independent subjects:

- the specification of the optimization process, including the selection of the tools (DoE, FEA, metamodeling and optimizations) together with capabilities for monitoring of the process status, and
- the specification of the initial design, including the product's geometry and its discretization, materials, loads, and constraints.

The process definition and monitoring requires embedding clients of the grid services, as described in Section "Horizontal Integration" above. Many different technologies can be used to develop this part of the user interface, e.g., a Java applet or extensions to existing stand-alone applications such as MathWorks' MATLAB™.

On the other hand, there are many state-of-the-art commercial and community tools available for specifying the initial design, such as Hypermesh, or vendor-provided GUIs for specific FEA packages, such as ABAQUS CAE™.

Since for the first demonstration problems an Abaqus input deck needs to be generated, it is natural to extend the ABAQUS CAE as the complete, stand-alone GUI for specifying the product design-optimization process. ABAQUS CAE interface has an open architecture with a published application program interface (API), and it is implemented in Python.

Thanks to the open architecture, ABAQUS CAE can be extended by providing new GUI elements and modules in Python, including modules that act as Grid services' clients. A similar approach – embedding the Grid clients into an existing standalone application – can be applied to other products used in the engineering practice, notably MATLAB.

The extensions needed to adopt the ABAQUS CAE as the GUI fall into two categories: GUI components and modules. The new GUI components, invoked through extensions to the existing menus, include forms to specify definition of design variables, constraints and objective functions as well as setting the parameters of DoE, metamodeling and optimization modules. Other GUI components allow control of the JSSs and display the status of all remotely run jobs.

In addition to new GUI element, six new modules have been added:

1. ABAQUS **input deck parser**. The initial product design is created using ABAQUS CAE tools, and the process results in generating the ABAQUS input deck that drives the FEA analysis of that initial design. The parsers extract variables defined in the input deck. This information is used for selecting the design variables (not all variables needed to simulate the design are subject to the optimization process), define objective functions and constraints (these are typically functions of the design variables).
2. **DoE module** does not require much CPU and, therefore, can be run inside the ABAQUS CAE environment. It is adopted from the HIPPO package (an Object-Oriented Framework for General Purpose Design Optimization by H. Wang) by rewriting it in Python.
3. **Input deck generator** replaces the value of design variables specified in the initial design by those generated by the DoE module.
4. **Metamodel creator**, using the native ABAQUS CAE Python libraries, parses the outputs of Abacus FEA simulations to extract the responses and creates the input data set to create the metamodel by launching a separate process outside the ABAQUS CAE environment.
5. **JSS client** delegates computations to remote, high-performance computers (including all necessary file transfers)
6. **JMS client** accesses the status of remotely-executed jobs.

Summary and Future Work

The developed cyberinfrastructure comprises a collection of Grid services that automates creation, submission and monitoring of jobs. In addition, support is provided for accessing information needed to identify the reasons of failures, should any occur. The front end of the system extends the commercial tool (ABAQUS CAE), that is, it augments the state-of-art user graphical interface for defining a FEA problem with GUI components for specifying the optimization problem and providing access to remote resources. The access to remote resources is achieved by embedding clients of grid services in the ABAQUS CAE. The next phases of the project include integrating this infrastructure with FAME and thorough test and validation of the system.

Support for Multiscale Simulations

We have developed an overlay scheduler to manage an adaptive tree of processes spawned while performing multiscale simulations. Further development of the support for multiscale simulations has been postponed. The concurrent developments of multiple system components jeopardize timely completion of the tasks, and the multiscale simulations are the least mature for automation and integration (as opposed to repository of material properties and support for design optimizations).

Portal for the Virtual Organization

The USAMP ICME for Mg international pilot project redefined our initial requirements for creation of the Virtual Organization. The new requirements call for the deployment of a collaborative portal based on Microsoft's' SharePoint server. This portal will enable sharing documents and management of the tasks and projects between the participants of the ICME Mg project. In the next step, the support for sharing data will be added and, finally, all capabilities of the cyberinfrastructure under development at MSST will be made available through this portal.

Conclusions

The creation of the cyberinfrastructure is on schedule, in spite of changes in the requirements. Of particular importance is the establishment of tight connections between this project and the ICME Mg project.

Presentations/Publications/Patents

1. T. Haupt, "Cyberinfrastructure for multiscale Simulations", *2007 TMS Annual Meeting*, Orlando, FL, Feb 25-March 1, 2007.
2. T. Haupt, A. Voruganti, A. Kalyanasundaram, I Zhuk. "Grid-Based System for Product Design Optimization", *2nd IEEE International Conference on e-Science and*

Grid Computing, Amsterdam, the Netherlands.
3. T. Haupt, A. Kalyanasundaram, I. Zhuk "Architecture for a Secure Distributed Repository", *7th IEEE/ACM International Conference on Grid Computing*, Barcelona, Spain: IEEE/ACM Press, 170-177.
4. T. Haupt, A. Kalyanasundaram, G. Singh, I. Zhuk, "Data Repository for Ad-Hoc Collaborations Horizontally Integrated with Transformation Services", *The 2007 International Conference on Grid Computing and Applications*, Las Vegas, NV, June 25-28, 2007.